Max-Planck-Institut
für Kolloid- und Grenzflächenforschung
Abteilung Theorie und Bio-Systeme

Universität Potsdam

Different Modes of Cooperative Transport by Molecular Motors

Dissertation

zur Erlangung des akademischen Grades
"doctor rerum naturalium"
(Dr. rer. nat.)
in der Wissenschaftsdisziplin theoretische Physik

eingereicht an der
Mathematisch-Naturwissenschaftlichen Fakultät
der Universität Potsdam

von
Florian Berger

Potsdam, Januar 2012

Published online at the
Institutional Repository of the University of Potsdam:
URL http://opus.kobv.de/ubp/volltexte/2012/6031/
URN urn:nbn:de:kobv:517-opus-60319
http://nbn-resolving.de/urn:nbn:de:kobv:517-opus-60319

Abstract

Cargo transport by molecular motors is ubiquitous in all eukaryotic cells and is typically driven cooperatively by several molecular motors, which may belong to one or several motor species like kinesin, dynein or myosin. These motor proteins transport cargos such as RNAs, protein complexes or organelles along filaments, from which they unbind after a finite run length. Understanding how these motors interact and how their movements are coordinated and regulated is a central and challenging problem in studies of intracellular transport. In this thesis, we describe a general theoretical framework for the analysis of such transport processes, which enables us to explain the behavior of intracellular cargos based on the transport properties of individual motors and their interactions. Motivated by recent *in vitro* experiments, we address two different modes of transport: unidirectional transport by two identical motors and cooperative transport by actively walking and passively diffusing motors.

The case of cargo transport by two identical motors involves an elastic coupling between the motors that can reduce the motors' velocity and/or the binding time to the filament. We show that this elastic coupling leads, in general, to four distinct transport regimes. In addition to a weak coupling regime, kinesin and dynein motors are found to exhibit a strong coupling and an enhanced unbinding regime, whereas myosin motors are predicted to attain a reduced velocity regime. All of these regimes, which we derive both by analytical calculations and by general time scale arguments, can be explored experimentally by varying the elastic coupling strength. In addition, using the time scale arguments, we explain why previous studies came to different conclusions about the effect and relevance of motor-motor interference. In this way, our theory provides a general and unifying framework for understanding the dynamical behavior of two elastically coupled molecular motors.

The second mode of transport studied in this thesis is cargo transport by actively pulling and passively diffusing motors. Although these passive motors do not participate in active transport, they strongly enhance the overall cargo run length. When an active motor unbinds, the cargo is still tethered to the filament by the passive motors, giving the unbound motor the chance to rebind and continue its active walk. We develop a stochastic description for such cooperative behavior and explicitly derive the enhanced run length for a cargo transported by one actively pulling and one passively diffusing motor. We generalize our description to the case of several pulling and diffusing motors and find an exponential increase of the run length with the number of involved motors.

Contents

1. Introduction

The basic functional unit of every living organism is the cell [1]. Thousands of molecules constantly participate in various biochemical reactions to maintain the complex internal structure of the cell [2]. Although these reactions typically take place on length scales on which thermal fluctuations are dominant, processes such as DNA replication or separation of chromosomes during cell division, are highly organized and occur in a precisely defined manner. Special types of proteins, so-called enzymes, catalyze specific chemical reactions and thus determine which biochemical pathways occur in the cell [2]. Hydrolases are enzymes that catalyze the hydrolysis of a chemical bond. One important subclass of hydrolases are motor proteins that are also called molecular motors [3]. Various motor proteins hydrolyze adenosine triphosphate (ATP) into adenosine diphosphate (ADP) and free inorganic phosphate (Pi), see fig. 1.1. In other words, they cleave ATP into ADP. This reaction releases free energy which the motor proteins convert into directed active motion.

The specific function of converting chemical energy into mechanical energy is at heart of various cellular processes and keeps the cell in a state far from equilibrium. Active pumps, embedded in membranes, maintain certain concentration gradients. Different polymerases process DNA and RNA sequences in a directed manner. During cell division, several active processes are involved in keeping the genomic information consistent between the divided cells. Even cell motility by the beating of flagella and muscle contraction are founded on the principle of converting chemical energy into mechanical work. Another class of processes based on this principle is intracellular cargo transport by molecular motors which, is the subject of this thesis.

1.1. Molecular motors

Active transport by molecular motors is ubiquitous in all eukaryotic cells [4]. In these cells, various processes are spatially separated by compartmentalization. Hence, the cell has to rely on a transport system to ensure the exchange of cargos such as RNAs, protein complexes, filaments and organelles. Passive transport driven by diffusion would be too slow in the crowded environment of the cytoplasm and its direction is difficult to regulate. For example, in an axon, an organelle like a mitochondrion has to be transported from the synapse to the region next to the nucleus for degradation, see fig. 1.2. In this case, a micrometer object has to cover a distance of up to one meter in an extended neuron cell, which would certainly take longer than the lifetime of the organism.[1] Thus, only passive diffusion

[1] The time for one-dimensional diffusion in aqueous solution is estimated for several objects in [3]. For an organelle with a 500 nm diameter it takes 10^{12} s to diffuse a distance of one meter.

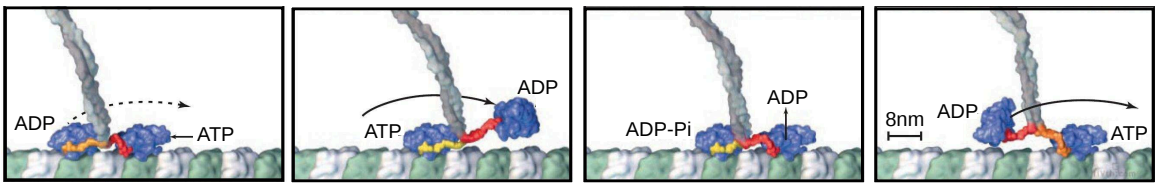

Figure 1.1 A molecular model of kinesin-1 converting chemical energy into mechanical by hydrolyzing ATP into ADP and Pi; taken from [5]. Because of the periodic structure of the filament, the motor performs a discrete step to the next binding site.

is insufficient for the cell and an active transport system by motor enzymes is required.

Molecular motors walk along the filament network of the cytoskeleton, which is the cell's skeleton made of proteins. Eukaryotic cells contain three different types of cytoskeletal filaments: actin filaments, intermediate filaments and microtubules [1]. Cargos are transported by motor proteins only along microtubules and actin filaments [6]. Microtubules consist of 13 protofilaments [5] and each of these protofilaments provides a track for a molecular motor. The filaments are polar with a plus and a minus end. This polarity can be recognized by motors, such that a single motor walks along the filament in a directed fashion. In cells, the filaments are differently organized according to their type: microtubules form long tracks from the cell center to the cell periphery, and the much shorter actin filaments act as a dense meshwork mainly in the cell periphery. Typically, microtubules are mostly arranged in such a way that their minus ends are close to the nucleus, where the microtubule organizing center is located, and their plus ends are pointing towards the cell periphery [7]. The organization of actin filaments is more complicated and varies with cell type [1,8]. However, in motile cells, actin is oriented primarily with the plus end towards the cell membrane [9].

Cytoskeletal motor proteins fall into two classes based on their substrate: actin-based motors and microtubule-based motors. The microtubule-based motors are further subdivided into two superfamilies: kinesins and dyneins [12]. There is only one known superfamily for transport on actin, namely the myosin superfamily [4, 13]. Many different members belong to these superfamilies and vary widely between different organisms. For example, mammals have genes for over 40 kinesins, 40 myosins and several dyneins [4]. The most prominent members involved in cargo transport are kinesin-1, cytoplasmic dynein and myosin V. The repeating structure of the filaments provides equally spaced binding sites for the motors. Therefore, motors move in discrete steps along these filaments. Kinesin and dynein take 8 nm steps along microtubules and myosin V walks in 36 nm steps along actin filaments [3]. Most of the kinesins walk towards the plus end of microtubules and all dyneins walk towards the minus end. As mentioned above, this directed movement requires energy supplied by the hydrolysis of ATP. The free energy released from this reaction induces an conformational change in the motor molecule. Thereby, the motor is able to move in a certain direction and to perform mechanical work. The occurrence of a step can be considered as a stochastic event with a frequency that depends on the ATP concentration. In addition, the stepping

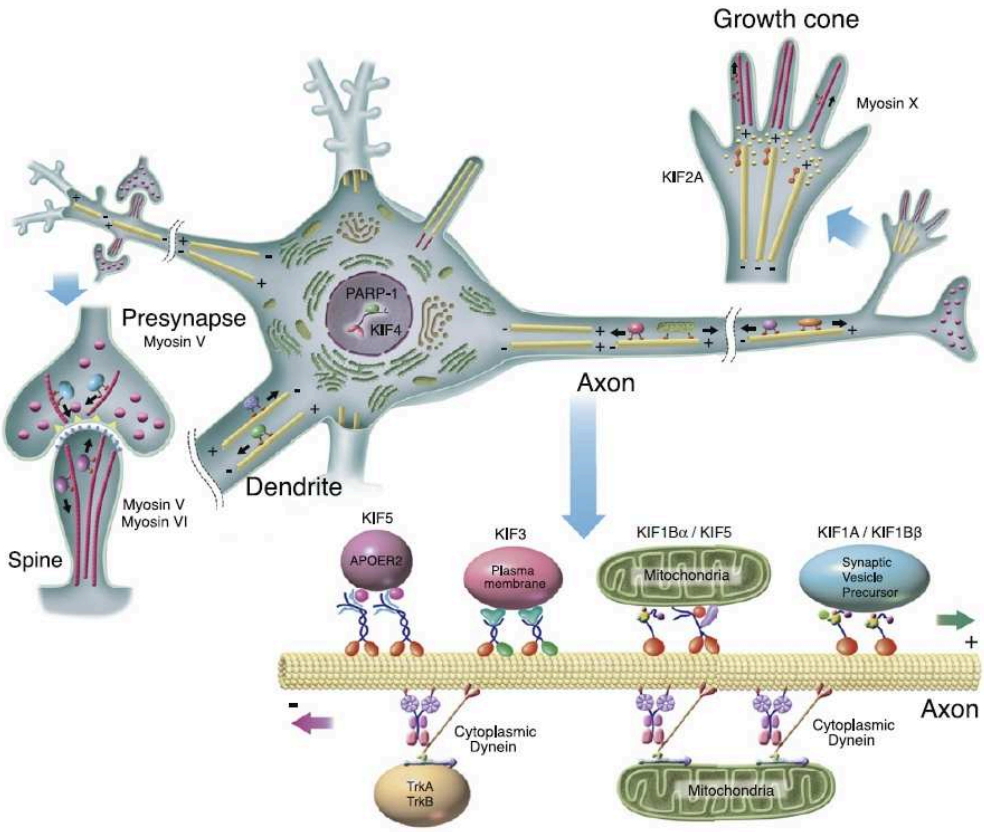

Figure 1.2 Cargo transport in a neuron cell, adapted from [10]. Microtubules (yellow rods) are arranged isopolarly in the axon. Actin filaments (red rods) are located in the cell periphery, the growth cone and the synapse. Large proteins (APOER2, TrkA, TrkB), mitochondria, synaptic vesicles and building blocks of the plasma membrane are transported by different motors. Myosins pull cargo along actin filaments and kinesins (KIFs) and dyneins along microtubules. Here, the kinesin motors are named by their gene sequence, usually starting with 'KIF' which is an acronym for the kinesin superfamily [11].

frequency can also depend on an external force-induced by a load. Typical load forces, which motors are able to bear, are on the order of pN.

Since motors constantly undergo thermal collisions with surrounding molecules, they unbind from their track after a finite run length. Motors that take many steps before unbinding are called processive motors [14]. For example, processive kinesin-1 performs roughly 100 steps before it unbinds from the filament.

Taken together, processive molecular motors stochastically step along the filaments by the hydrolysis of ATP and, in this way, cover distances of μm. Different types of motors use different filaments and walk in different directions. They can be characterized by different physical quantities, such as the maximum load they are able to bear, their velocity and their

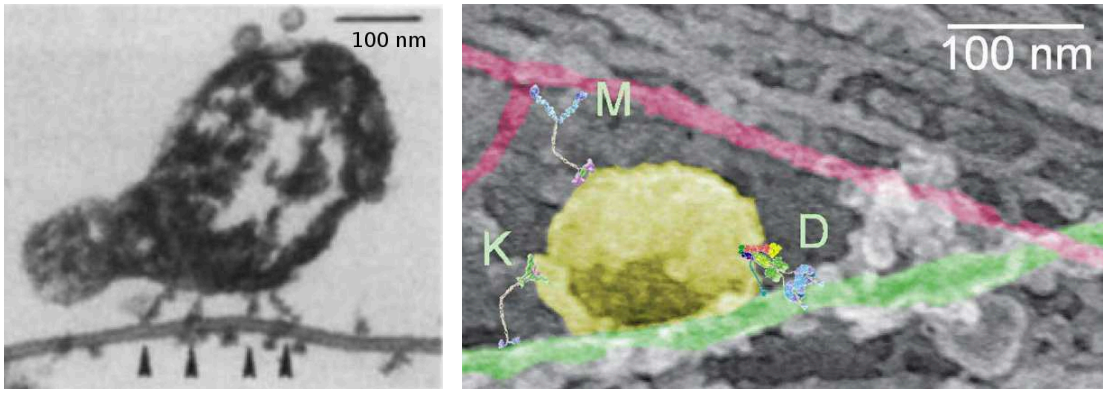

(a) (b)

Figure 1.3 Examples of cargo transport by several molecular motors. (a) Electron microscopy image of a mitochondria transported by four motors indicated by arrows; from [15]. (b) Cargo transported by three different types of motors: kinesin (K), dynein (D) and myosin (M); taken from [16]. The motors are drawn approximately to scale. The background image is an electron micrograph showing a vesicle (colored in yellow), a microtubule (colored in green) and actin filaments (colored in red).

binding time.

1.2. Cargo transport by cooperative action of molecular motors

In cells, cargo transport relies on the cooperative action of molecular motors as revealed by electron microscopy [15, 17, 18] and optical tracking of cargo particles [19–21]. From electron microscopy pictures, it is evident that several motors are attached to the same cargo, see fig. 1.3(a). The observation of cargos reversing their direction of motion along the filament and switching between microtubules and actin lead to the notion that different types of motors are involved in transporting the same cargo, see fig. 1.3(b). How multiple motors are coordinated, in particular when the transport involves two or more species of motors, is currently an area of active research [16, 22, 23]. Although various combinations of different types of motors are possible and presumably occur in the cell, we discuss three basic cases: unidirectional transport by one team of motors, bidirectional transport by two teams of motors and transport on different tracks, involving both actin- and microtubule-based motors. All three cases have been studied extensively in recent years, both experimentally [24–29] and theoretically [23, 30–32].

1.2.1. Unidirectional transport

Even though a single motor molecule can power processive motion, transport in cells is often driven by more than one motor [33]. One advantage of cargo transport by several motors

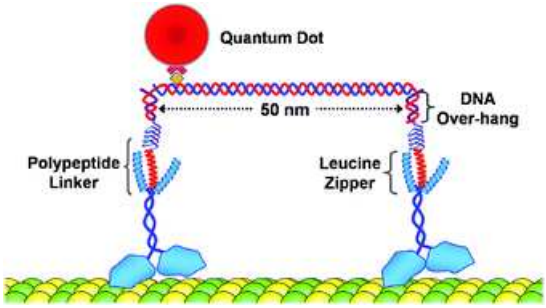

Figure 1.4 Kinesin assembly as studied in the Diehl lab [25]; figure adapted from [25]. Two kinesins are coupled via polypeptide linkers to a 50 nm DNA scaffold. The movement of the assembly is observed by following the attached quantum dot.

is a higher velocity if the cargo experiences a high viscosity [24, 34, 35]. Another advantage of cooperative transport is an increased run length compared to the run length of a single motor, which is typically about 1 μm: if one motor unbinds, the cargo is still transported by the other motors and the unbound motor has a chance to rebind to the filament. In this way, cargos can be transported over cellular distances that are on the order of tens of micrometers. A theoretical study, based on the assumption of non-interacting motors, indicates that the run length increases exponentially with the number of motors [30]. Qualitatively, an increase in the run length has been known for a long time for kinesin [36] and recently also reported for dynein [37] and myosin V [38]. However, quantitative experiments remain challenging, because it is difficult to determine the number of motors involved in the transport [39]. Two recent studies of the run lengths of beads covered with different amounts of kinesin-1 have attempted to estimate the motor number on the basis of force measurements [40] or run length distributions [24]. While the observations from the latter study were consistent with the theoretical predictions, the former study found longer run lengths than expected.

However, in both studies only the average number of motors could be determined and the actual number of motors engaged in transport varied from bead to bead. Furthermore, the precise geometric arrangement of the motors was not known. These difficulties have been overcome in a recent study that used synthetic complexes of two kinesin motors connected through a rigid DNA scaffold [25], see fig. 1.4. The experiments suggest that motors strongly interfere in such a way that they pull each other from the filament. In the discussion of these findings, the notion of induced elastic strain forces arises. These strain forces influence the dynamics of the individual motor. In addition, in a surface gliding assay experiment, involving however a large number of processive kinesins, the influence of the elastic coupling between the motors on the overall velocity was studied [41]. These experiments suggest that elastically coupled motors slow each other down depending on the strength of the elastic coupling. Therefore, loose mechanical coupling between motors is required for efficient transport. Recently, much theoretical effort [23,30,42–47] has been devoted to these transport processes but different studies came to different conclusions about the relevance of strain and interference effects. Nevertheless, the observations of interference effects indicate

that, while run lengths of cargo do increase with the number of pulling motors, the increase may be less pronounced than what is estimated based on non-interacting motors and that more motors than previously thought may be necessary for transport over typical cellular distances.

1.2.2. Bidirectional transport

Many intracellular cargos, such as mitochondria, pigment granules, endosomes, lipid droplets and viruses, move in a bidirectional manner, reversing direction every few seconds [20, 48]. Bidirectional motion requires at least two types of motors that are attached to one cargo, e.g. kinesin-1 and cytoplasmic dynein. Two mechanisms for bidirectional transport have been proposed [20,48]: (i) biochemical coordination by a hypothetical coordination complex which ensures that only one type of motor is active at any given time; and (ii) mechanical coordination through a tug-of-war between the motors, which pull on each other until one type of motor team wins and drags the cargo in its direction. Several recent experiments provide clear evidence for such mechanical interactions between the two motor teams [27,49, 50]. A systematic theory for bidirectional transport based on a stochastic tug-of-war model has been developed in [31,51,52]. This framework is fully consistent with experimental data and explains the bidirectional motion of lipid-droplets [31] and of endosomes [27,28] without any putative coordination complex.

1.2.3. Transport on different filaments

Long-range transport within a eukaryotic cell is typically microtubule-based, whereas short-range transport at the cell periphery is actin-based. Various cellular cargos such as mitochondria, pigment granules and synaptic vesicles use both transport systems as reviewed in [21, 53, 54]. To be able to switch from one transport system to the other without any interruption, actin motors as well as microtubule motors are attached simultaneously on the same cargo [21, 53, 54]. Switching between filament species depends on cellular regulation, on the cargo and on the number and type of motors [55–57]. Recently, it has been discovered that, when a cargo is transported on one kind of filament, say a microtubule, both microtubule- and actin-based motors can interact with that filament. The microtubule motor is strongly bound and actively pulls the cargo, whereas the actin-based motor tethers the cargo to the filament, presumably via an unspecific electrostatic interaction. It has been found that the actin-based motor myosin V can diffuse randomly on a microtubule [58] and that the microtubule motor kinesin-1 has a weak affinity for actin [29]. A cargo transported along a microtubule by kinesin-1 and myosin V exhibits fast directed motion interrupted by diffusive events [29]. During these diffusive events, kinesin is not bound to the microtubule but the cargo is still tethered to the filament by the myosin motor, which gives kinesin the chance to rebind. Overall, the run length of such a cargo is more than twice that of a cargo transported by a single kinesin alone.

This enhancement of motor processivity has also been observed in other systems. For example, the non-processive myosin motor Myo2p was shown to transport a cargo proces-

sively along an actin filament if the kinesin-related protein Smy1p was present on the same cargo [59]. Similarly, effects of diffusing linkers have also been discussed on the level of single-motor molecules [60]. For example, dynein and kinesin-2 use the large complex dynactin [61–63] and myosin V uses melanophilin [64] as tethers. The role of these tethers is to prevent the motor from unbinding from the filament and thus to enhance its run length.

1.3. Overview

In this thesis, we study cooperative transport by molecular motors from a theoretical perspective. We address unidirectional transport by two identical motors and transport involving different filaments by actively pulling and passively diffusing motors, based on a description for the dynamics of a single motor. In **chapter 2**, we introduce such a reduced single motor description incorporating the stochastic motor dynamics as known from experiments. For a probabilistic treatment, we discuss Markovian dynamics and review a method to obtain averaged quantities for time dependent processes. Furthermore, we introduce a generalization of this method for arbitrary initial conditions.

The unidirectional transport by two elastically coupled motors is addressed in **chapter 3**. We introduce a general state space for two elastically coupled motors based on single motor parameters. From this state space, we derive four different transport regimes for a motor pair. The emergence of these regimes can be understood intuitively by the comparison of three different time scales. These time scale arguments allow us to predict which of the different transport regimes should be observed for different motor types when their coupling strength is varied. Several extensions of the single motor description are studied quantitatively and an intuitive understanding is developed by means of the time scale arguments. Finally, we apply the framework developed here to quantitatively discuss experimental results from the Diehl lab obtained with two coupled kinesin-1 motors [25].

Chapter 4 deals with the observed enhanced run length of cargo transport involving motors that move along different filaments. We focus on the case of a cargo transported along a microtubule by one microtubule-based motor kinesin and one actin-based motor myosin V. For the corresponding quantitative description of such a cargo, we deduce all parameters from experimental quantities and explain the cooperative effect of the enhanced run length in terms of single motor properties. Once we know the single motor properties, we study cargo transport by the cooperative action of several passively diffusing and several actively pulling motors, which leads to an exponential increase of the cargo's run length and to an effect on the cargo's velocity: more diffusing motors reduce the overall cargo velocity, whereas more pulling motors keep the velocity constant.

Chapter 5 concludes with a summary and raises further questions concerning cooperative transport, some of which can be addressed with an appropriate extension of the framework developed in this thesis.

Supplementary material is presented in the appendix, including detailed calculations, further extension and discussions of the reduced single motor description and its influence on the dynamics of a motor pair.

1.3.1. List of publications

This thesis contributed to the following publications:

- 'Distinct transport regimes for two elastically coupled molecular motors'
  F. Berger, C. Keller, S. Klumpp, and R. Lipowsky, submitted (2011)
- 'Co-operative transport by molecular motors'
  F. Berger, C. Keller, M. J. I. Müller, S. Klumpp, and R. Lipowsky, Biochem. Soc. Trans. 39, 1211 (2011).
- 'Cargo transport by teams of molecular motors: Basic mechanisms for intracellular drug delivery'
  M. J. I. Müller, F. Berger, S. Klumpp, and R. Lipowsky, Organelle-specific Pharmaceutical Nanotechnology, edited by V. Weissig and G. G. D'Souza, pp. 289-309. (Wiley, Hoboken NJ, 2010).
- 'Enhancement of the processivity of kinesin-transported cargo by myosin V'
  F. Berger, M.J.I. Müller, and R. Lipowsky, EPL 87, 28002 (2009).

2. Basic description of transport by molecular motors

In this chapter, we introduce a reduced single motor description which is suitable for the length and time scales that we are interested in. We discuss experiments, from which we deduce all parameters to describe processive molecular motors such as kinesin-1, dynein, myosin V, and myosin VI. The basic motor processes of stepping along, binding to and unbinding from the filament are of stochastic nature. For an appropriate description, we introduce continuous-time Markovian dynamics. Furthermore, we present a generalization of a method originally introduced by T. Hill that is, to our knowledge, new. This method enables us to calculate quantities such as average velocities, average binding times and average run lengths of cargos for arbitrary initial conditions.

2.1. Transport on different scales

Transport by molecular motors covers a wide range of time and length scales. Different experimental setups and theoretical descriptions have been established to reveal and understand the transport behavior of molecular motors on these different scales. Three regimes of transport can be identified with typical time and length scales [65]:

- On the molecular level, motor proteins step discretely on a nanometer scale by hydrolyzing ATP, see fig. 2.1(a). For kinesin-1, the time for the actual step is very short and about 15 μs [69]. However, the time to complete one enzymatic cycle depends on the ATP concentration. Kinesin-1 takes a step every 10 ms in the case of saturating ATP concentration [69]. The details of the enzymatic motor cycles governing the motion of molecular motors have been studied in single molecule experiments [70, 71], as well as in theoretical descriptions based on a discrete Markovian state space [72, 73].

- Cargo particles transported by processive motor proteins cover distances of μm before they unbind from their track after a binding time of seconds, see fig. 2.1(b) [36, 74]. Therefore, typical cargo velocities are of the order of μm/s. The walking distance and the binding time can be increased by the cooperative action of several motors of the same species [24, 30]. Cargos that are transported by different species of motors exhibit interesting transport properties like bidirectional motion [20, 31, 48], enhanced processivity [29, 32] or mutual motor activation [75]. Transport on the μm scale can be accessed experimentally by different microscopy techniques [76]. Theoretical studies describe the rich behavior of cooperative transport based on the known single molecule properties, reviewed in [23].

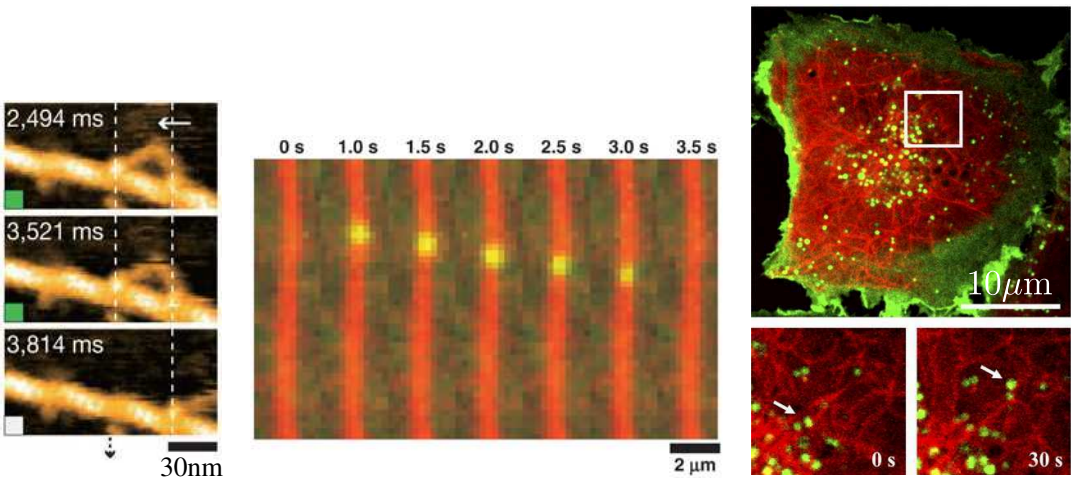

(a) (b) (c)

Figure 2.1 Transport by molecular motors on different scales: (a) Time-series of one step by myosin V recorded with high-speed atomic force microscopy [66]. The typical length scale is nanometer and the typical time scale for stepping is of the order of milliseconds. (b) TIRF microscopy image of quantum dot (green) transported by several kinesins along red-labeled microtubules [67]. Here, the typical length and time scales are micrometers and seconds, respectively. (c) Live cell confocal image of cargo transport through a whole alveolar epithelial cell on large length scales of tens of micrometers and long time scales exceeding minutes [68]. Vesicles (green dots) are transported along red-labeled microtubules. Bottom panels: magnification (white square) of two time windows showing a single vesicle indicated by the white arrow that moves along the microtubule over time (0 s and 30 s).

- On the length scale of cells, which ranges from a few micrometers up to meters in axons, cargo transport can be divided into two processes: active transport by motors along the filament and diffusion in the cellular environment when the cargo is detached from the filament [77]. Cycles of reattachment to, being transported along and unbinding from the filament leads to cargo transport on large length and time scales exceeding micrometers and seconds, see fig. 2.1(c). However, *in vivo* , additional processes like motor recruitment to the cargo and other functions of adapter proteins influence the details of the cycles [4, 7]. This large scale transport can be accessed experimentally with different microscopy techniques [76]. Theoretical studies describe the interplay of active movement, unbound diffusion, binding and unbinding of motors [78, 79].

In this thesis, we focus on the second regime of time and length scale. Using a reduced single motor description that is consistent with results obtained in the first regime, we deduce and predict properties of cooperative transport in the second regime. In the following, we introduce the reduced description of a single molecular motor that provides the basic

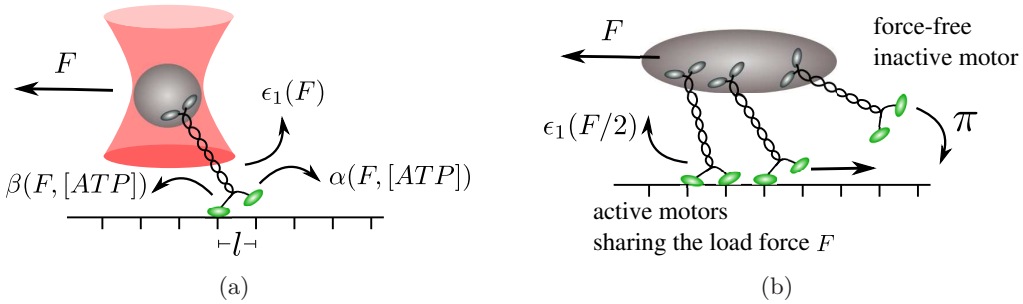

Figure 2.2 Motor parameters: (a) A processive molecular motor in an optical trap walking on a discrete lattice with step size l. In general, the forward stepping rate α and the backward stepping rate β depend on the external force F and the ATP concentration. The motor unbinds with the force-dependent unbinding rate $\epsilon_1(F)$. (b) Several motors transport a common cargo. Motors that are bound to and step along the filament are *active* motors governed by the dynamics depicted in (a). These active motors share the external load force F. For example, the left motor is exposed to half the load force. Motors that are attached to the cargo but unbound from the filament are called *inactive* motors. They do not participate in active transport. These inactive motors can rebind to the filament with binding rate π.

dynamical processes for our study.

2.2. A single molecular motor

In this section, we introduce a coarse-grained description of a single molecular motor. Similar reduced models have been used successfully in several theoretical studies [30, 31, 43, 45]. Since the motor is influenced by the thermal environment, the basic processes of binding to, unbinding from and stepping along the filament occur stochastically. Therefore, we associate rates to these processes defined as the average frequency per time for the corresponding process to occur. In general, the rates depend on additional parameters like the external force and ATP concentration. Our generic description can be applied to a large variety of different motors by adapting the rates to characterize specific functions. The numerical values for the parameters of our description are taken from force-dependent single molecule experiments that we discuss later in this section.

2.2.1. Theoretical description of processive motors

Processive motors bind to, walk along and unbind from the filament. In general, these processes depend on external parameters such as the load force and ATP concentration. Their precise details have been revealed in force-dependent single molecule experiments, mostly done with the best-studied motor kinesin-1. Following the convention of the literature, the direction of the applied load force is positive if it is opposite to the forward stepping di-

rection of the motor, see fig. 2.2. A negative force towards the walking direction is termed assisting force. In our reduced description, we consider the motor as a point particle, to which an external force is transmitted via an elastic element.

Active, inactive and passive motors

Next, we comment on some of the terminology used in our study. We call a motor *active*, if it is bound to the filament and walks along it by hydrolyzing ATP. On the other hand, motors are *inactive*, if they are not bound to the filament, but still attached to the cargo. For example, we consider a fixed number of motors attached to a cargo. During cargo transport, motors unbind and rebind to the filament. In this way, the number of active and inactive motors fluctuates, see fig. 2.2(b). In the biochemical literature, in contrast, inactive refers to the state of motors, in which they are not attached to a cargo and in an inhibited conformation [80]. Presumably, such a conformation ensures that the motor is not needlessly burning ATP or clogging up the microtubule roadways. Furthermore, we term a motor *passive*, if it is bound to the filament, but not able to move actively by hydrolyzing ATP. For example, this is the case when the actin motor myosin V binds unspecifically to and diffuses along microtubules, as studied in chapter 4.

Binding to the filament

In the context of cargo transport by molecular motors, two distinct situations are usually termed as binding processes. The first is the binding of a freely diffusing cargo, or motor, from the solution to the filament. This process depends on the geometry and the diffusive dynamics. The second process is the binding of the motor, when it is close to the filament, i.e., binding of an inactive motor attached to a cargo which is tethered by other motors to the filament, see fig. 2.2(b). As we will see later, our study focus on cargos that are already close to the filament, and therefore we only have to take the second process into account. The binding of the motor protein to the filament is a complicated process on the atomistic level. From a coarse-grained point of view, as a first order approximation, we assume that the motor can be in a bound state or in an unbound state. We describe the transition from the unbound state to the bound state with a single binding rate π. Since the binding process is not very well studied in experiments, we consider the binding rate as constant and independent of other parameters, particularly independent of an external force. This is reasonable because even if there is a force acting on the cargo, an inactive motor is in a relaxed force-free state and the binding process should be independent of it, see fig. 2.2(b). In principle, the rate could depend on parameters which influence the finding of the binding site on the filament and the formation of the motor-filament bond.

Stepping along the filament

When a motor is bound to the filament, it moves forward and backward in discrete steps. In our reduced description, we consider the motor as a stochastic stepper with a forward

stepping rate α, a backward stepping rate β and a step size l. Generally, these stepping rates could depend on the external load force F and the ATP concentration,

$$\alpha = \alpha(F, [ATP]) \tag{2.1}$$
$$\beta = \beta(F, [ATP]). \tag{2.2}$$

We relate these rates to experimentally accessible quantities. Usually, analyzed data from single molecule experiments provide the force-velocity relation $\mathcal{V}(F, [ATP])$, which is the average velocities of the motor, and the ratio of forward to backward steps $q(F, [ATP])$. Both quantities can be written in terms of the stepping rates [77], leading to

$$\mathcal{V}(F, [ATP]) = l[\alpha(F, [ATP]) - \beta(F, [ATP])] \tag{2.3}$$

and

$$q(F, [ATP]) = \frac{\alpha(F, [ATP])}{\beta(F, [ATP])}. \tag{2.4}$$

From these equations we obtain the forward stepping rate,

$$\alpha(F, [ATP]) = \frac{q(F, [ATP])}{q(F, [ATP]) - 1} \frac{\mathcal{V}(F, [ATP])}{l} \tag{2.5}$$

and the backward stepping rate,

$$\beta(F, [ATP]) = \frac{1}{q(F, [ATP]) - 1} \frac{\mathcal{V}(F, [ATP])}{l}. \tag{2.6}$$

The precise form of $\mathcal{V}(F, [ATP])$ and $q(F, [ATP])$ differ between different motor species. However, as a common feature the velocity vanishes for a high load force, the stall force F_s that we implicitly define as

$$\mathcal{V}(F_\mathrm{s}, [ATP]) \equiv 0. \tag{2.7}$$

Hence, in case of $F = F_\mathrm{s}$, we obtain from eq. (2.4) the stepping ratio

$$q(F_\mathrm{s}, [ATP]) = 1. \tag{2.8}$$

Subjected to a force smaller than stall force, highly processive motors perform much more forward steps than backward steps, i.e., $q(F, [ATP]) \gg 1$ [69]. For this reason, we have

$$\frac{q(F, [ATP])}{q(F, [ATP]) - 1} \approx 1 \tag{2.9}$$

and

$$\frac{1}{q(F, [ATP]) - 1} \approx 0. \tag{2.10}$$

In case of small forces, we neglect backward steps and the forward stepping rate is given by

$$\alpha(F, [ATP]) = \frac{\mathcal{V}(F, [ATP])}{l}. \tag{2.11}$$

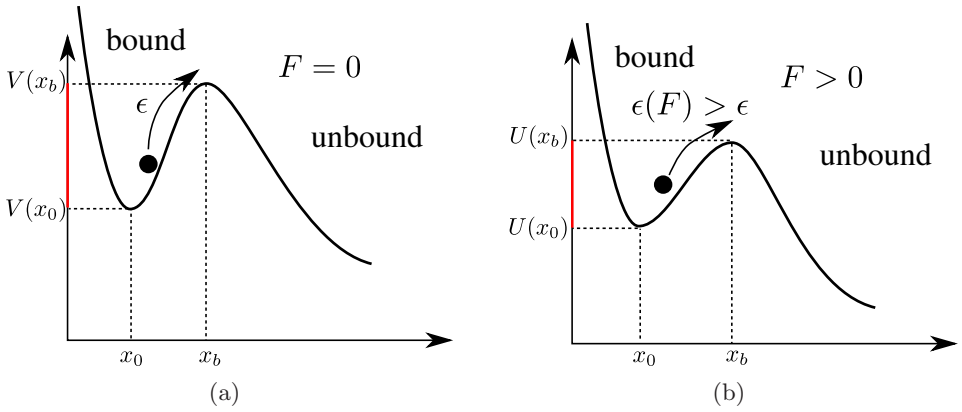

Figure 2.3 Kramer's escape rate problem: (a) The state, in which the motor is bound to the filament, is associated with the minimum at x_0 of the potential $V(x)$. Kramer's theory describes unbinding as the transition over a potential barrier at x_b driven by diffusion. (b) Applying an external force F to the bond leads to a tilted potential $U(x) = V(x) - Fx$ with a reduced barrier height $U(x_b) - U(x_0) = V(x_b) - V(x_0) - F(x_b - x_0)$. The escape rate under force is higher than in the force-free case.

On a micrometer and second scale, this stepping dynamics appears as a smooth directed movement with a constant velocity. From this point of view, a motor, or a cargo, can also be considered as a particle which performs a directed motion that starts and ends in a stochastic manner. Such a semi-stochastical description has been used in previous studies of cooperative motor transport [30, 31] and will be applied in chapter 4.

Unbinding from the filament

The motor heads[1] form a biomolecular bond with the filament. Similar to the binding process, we describe the bond dissociation with a single rate. This idea of reducing the intrinsic complexity of the molecular details based on Kramers' escape rate theory [81] has widely been used and extended in biophysical studies [82–84]. Here, the dissociation of the bond is associated with the diffusive escape of an over-damped Brownian particle with diffusion coefficient D over a one dimensional potential barrier. The spatial coordinate for the particle corresponds to the reaction coordinate. Let x_0 be the position of the bound state and x_b the position of the maximum of the barrier of the potential $V(x)$, see fig. 2.3(a). The rate for escape follows from a mean first passage time calculation with a saddle point approximation for the potential [85] and depends exponentially on the height of the potential barrier,

$$\epsilon \sim e^{-(V(x_b)-V(x_0))/k_\mathrm{B}T}, \tag{2.12}$$

here $k_\mathrm{B}T$ is the product of the Boltzmann constant and the temperature. The prefactor, which is not shown here, depends on the second derivatives of the potential [85]. This

[1] Motor heads are the motor domains that bind to the filament, see fig. 2.7

Kramers rate is valid for a large potential barrier, i.e., $V(x_b) - V(x_0) \gg k_\mathrm{B}T$ and non equilibrium steady state condition [85, 86].

When a constant force is applied to the bond, the dissociation rate increases. The Kramers rate as in eq. (2.12) allows us to estimate the influence of the force. In this one dimensional reduced description, a constant force adds the energy $-Fx$ to the potential and lowers the barrier, see fig. 2.3(b). Together with the tilted potential $U(x) \equiv V(x) - Fx$, we obtain a force-dependent dissociation rate from eq. (2.12),

$$\epsilon(F) = \epsilon e^{F(x_b - x_0)/k_\mathrm{B}T}. \tag{2.13}$$

This exponential force-dependence of the rate has been first discussed by Bell [82].

Despite of the complexity of the molecular details of the motor-filament bond, we assume that the force dependency of the bond dissociation can be described according to Bell's equation (2.13). Furthermore, as a first approximation, we treat all directions equally and thus the unbinding rate increases under an external force independent of its direction. To account for these assumptions, we use the absolute value of the force and obtain from eq. (2.13) the force-dependent unbinding rate of a single motor,

$$\epsilon_1(F) = \epsilon e^{|F|/F_\mathrm{d}}. \tag{2.14}$$

Here, we introduce the force scale $F_\mathrm{d} \equiv k_\mathrm{B}T/(x_b - x_0)$, which we term the detachment force. In general, forces in different directions, for example perpendicular to the filament, have different impact on the motors [87]. However, in our description only forces parallel to the filament occur. These forces arise from other motors attached to the cargo. As a refinement of the assumptions entering into eq. (2.14), we distinguish the forward and backward direction of the motor in section 3.4.4. In general, other functional forms of the force-dependent unbinding rate can also be incorporated into our description.

Elasticity of motor proteins and cargos

Not only motor proteins, but also adapter proteins for the motor cargo linkage and cargos themselves are often soft objects with a considerable elasticity [80]. When studying cooperative cargo transport forces between the motors are exerted via these elastic elements. As mentioned above, we only consider forces parallel to the filament and thus we describe the relation between the elastic strain force and the deformation with a one dimensional force extension relation $F(\Delta x)$, where the extension Δx is along the filament. In order to develop a general understanding, we will not account for specific elastic elements, but rather study four different generic types of elasticity: a linear spring, a cable, a freely jointed chain (FJC) and a worm like chain (WLC).

A linear spring is described by a linear force extension relation, i.e.,

$$F = \kappa \Delta x, \tag{2.15}$$

with spring constant κ. The force extension relation for a cable is split in two regions. In the compression mode, where the actual end to end distance of the elastic element is

smaller than a rest length l_0 no forces are needed for extension. In the stretch mode, where the actual length is larger than the rest length a linear force extension relation applies. Therefore, the force extension relation for a cable reads

$$F(\Delta x) = \begin{cases} 0 & \Delta x < l_0 \\ \kappa(\Delta x - l_0) & \Delta x \geq l_0. \end{cases} \tag{2.16}$$

The linear spring and the cable are good approximations for small extensions. However, for large extensions, we expect that the force needed for further extension increases rapidly. From a more realistic point of view, every elastic element has a maximal extension length before it ruptures. To account for a non-linear increase in force and a finite extension, we use the force extension relations from two simple models for describing polymers, namely the freely jointed chain and the worm like chain.

The FJC is composed of segments each with length L_s and connected in such a way that they are able to swivel freely in three dimensions. Stretching such a chain by a force in a certain direction leads to an extension Δx along this direction. This extension as a function of the magnitude of that force can be derived theoretically as [3]

$$\Delta x = L_\mathrm{c} \left(\coth \left[\frac{F L_\mathrm{s}}{k_\mathrm{B} T} \right] - \frac{k_\mathrm{B} T}{F L_\mathrm{s}} \right), \tag{2.17}$$

with two parameter: the maximal contour length L_c and the segment's length L_s.

A very flexible slender rod should qualitatively behave like a FJC with many segments. This case is described by a worm-like chain (WLC) with maximal length L_c and persistence length L_p. The persistence length is a parameter describing the resistance to thermal forces. Qualitatively, if $L_\mathrm{p} \gg L_\mathrm{c}$ the object is rigid, whereas for $L_\mathrm{p} \ll L_\mathrm{c}$ the object is very flexible. The force as a function of the extension can be approximated by [88]

$$F(\Delta x) = \frac{k_\mathrm{B} T}{L_\mathrm{p}} \left(\frac{1}{4(1 - \Delta x / L_\mathrm{c})} - \frac{1}{4} + \frac{\Delta x}{L_\mathrm{c}} \right). \tag{2.18}$$

An intuitive derivation of this equation can be found in [89].

2.2.2. Experimental values for the single motor properties

In the previous section, we introduced a reduced single motor description which incorporates generic features of molecular motors. In this section, we discuss experimental results from which we obtain the numerical values of the parameters for that description.

Binding rate

Since it is difficult to measure the binding rate π directly, it is often used as a fit parameter. In an experiment, where kinesin-1 motors extract a membrane nanotube from a vesicle in contact with a microtubule, a binding rate $\pi \simeq (4.7 \pm 2.4)\,\mathrm{s}^{-1}$ has been obtained [90]. The run length distribution of beads transported by several kinesin-1 motors could be fitted

parameter	kinesin-1	dynein	myosin V	myosin VI
π [s^{-1}]	5* [24,90]	1.6* [31]	-	-
l [nm]	8 [70]	8 [91]	36 [92]	36 [93]
q_0	800 [69]	-	-	-
F_s [pN]	6 [94,95], 5 [96], 7 [69]	7 [97] 1.1 [98]	1.7 [92], 3 [99]	2.8 [100]
v [nm/s]	1000 [94], 490 [25]	650* [31], 700 [62]	400 [92], 380 [101]	150 [101], 291 [100]
ϵ [s^{-1}]	1 [94], 0.6 [25]	0.27* [31], 0.16 [37]	0.48 [99], 0.3 [101]	0.25 [101], 1.3 [100]
F_d [pN]	3 [94]	1.1* [31]	4* [101]	2.6* [101]
κ [pN/nm]	0.3 [96], 0.5 [102], 0.2 [25]	$0.1 - 0.5$ [103,104]	$0.2 - 0.45$ [105]	-
l_0 [nm]	80 [12]	40 [106]	80 [107]	-

Table 2.1 Overview of parameters for the different molecular motors, kinesin-1, dynein, myosin V and myosin VI. The parameters are the binding rate π, the step size l, the force-free forward to backward stepping ratio q_0, the stall force F_s, the force-free velocity v, the force-free unbinding rate ϵ, the detachment force F_d, the molecule stiffness κ and the molecule length l_0. The parameters have been obtained in the cited studies. The stared values are indirectly obtained from theoretical modeling of experimental data.

with a binding rate of $5\,s^{-1}$ [24]. In both experiments, the inactive motors are close to the filament and therefore, they have a fairly high chance to rebind. In contrast, in an two motor experiment with kinesin-1, the run length could be fitted with a binding rate of $1.03\,s^{-1}$ [25]. Obviously, the binding rate depends on the geometry of the cargo, on the arrangement of the motors on the cargo [108] and on the buffer used in the experiment. Therefore, it should not be taken as an inherent motor parameter.

For other motor species, the binding rate can only be estimated from the dissociation constant [109] or used as a fit parameter, since there are no experimental data available to our knowledge.

Stepping rates from force-velocity relations

The stepping rates are determined by the step size l, the ratio of forward and backward steps $q(F)$, and the force-velocity relation $\mathcal{V}(F)$ as explained in section 2.2.1. Two experimental methods are widely used to study the force-dependence of motor dynamics: a stationary optical trap and a force-feedback trap [76, 110], see fig. 2.4. In both setups the filaments are immobilized on a substrate. Beads coated with motor proteins are transported along these filaments. The dielectrical beads can be manipulated with focused laser beams, so-called optical tweezers or optical traps. The radiation pressure provides a potential for the dielectric beads [111], which can be approximated as a quadratic potential with a trap stiffness [112]. In the case of a stationary trap, the distance between the trap center and the bead increases as the motor pulls the bead along the filament, see fig. 2.4(a). In this way, the force on the motor heads increases in time [96]. In order to attain a large force before the motor unbinds, in some experiments, this force increase is supported by moving the stage on which the microtubules are immobilized [95]. In contrast, in a force-feedback

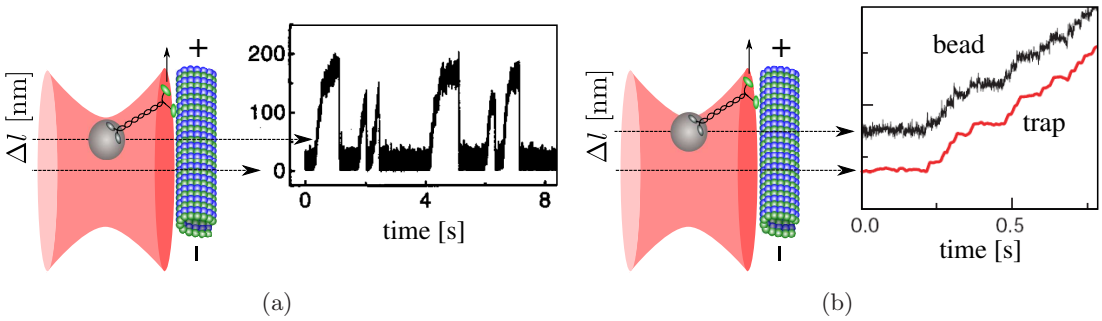

Figure 2.4 Kinesin-1 in optical traps with corresponding trajectories. The motors, the filaments and the optical trap are not drawn to scale. (a) In a stationary trap the distance Δl between the bead and the trap center increases as kinesin-1 walks along the filament. Hence, the force applied on the motor also increases. The example trajectory is taken from [95]. The plateaus of the trajectories correspond to the stall force. The sudden drops indicate unbinding from the filament and the bead falls back to the center of the trap. (b) In a force-feedback trap, the force applied to the motor is kept constant by readjusting the position of the center of the trap in such a way that Δl is kept constant. The trajectory, taken from [70], reveals discrete steps.

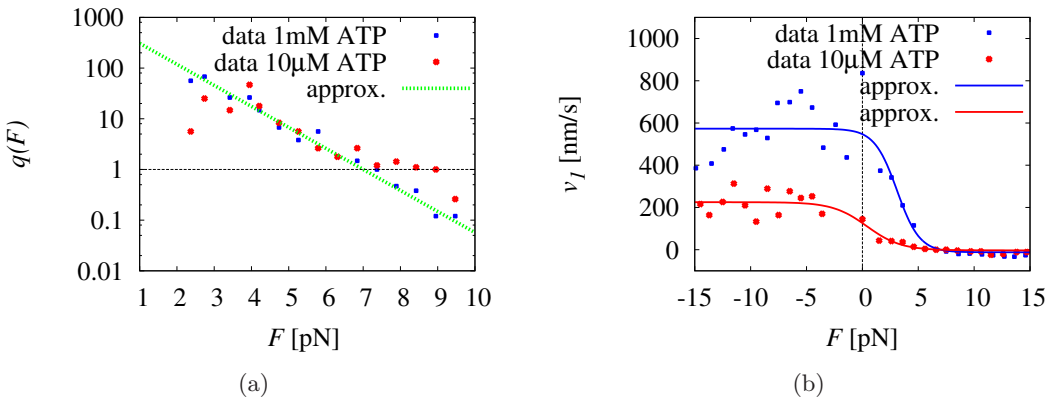

Figure 2.5 Experimental data for kinesin-1 stepping taken from [69]. (a) Ratio $q(F)$ of forward to backward stepping rates as a function of load force F for different ATP concentrations: 1mM ATP (blue) and 10μM ATP (red). The line in the logarithmic plot is given by eq. (2.19) with $q_0 \simeq 800$ and $F_s \simeq 7$pN as suggested in [69]. (b) Force-velocity relation for kinesin-1 for different ATP concentrations taken from [69]. The two lines are approximate force-velocity relations discussed in appendix A.4.

trap the distance between the bead and the trap center is kept constant by adjusting the trap according to the position of the bead [110, 113]. One advantage of the force-feedback trap is that the movements of the motor is directly displayed as the movements of the bead, see fig. 2.4(b). In the case of a stationary trap, the movements of the beads are smaller than those of the motor because of the compliance of the motor bead linkage [96, 112].

Both, the stationary trap as well as the force-feedback trap have been used to determine the force-dependent dynamics of single motor proteins. From these trajectories, a discrete step size l of the motor can be detected: $l \simeq 8\,\mathrm{nm}$ for kinesin-1 [70], as well as for dynein [91] and $l \simeq 36\,\mathrm{nm}$ for the actin motors myosin V [92] and myosin VI [93].

Kinesin-1 is the best studied motor protein. Carter and Cross obtained the force-dependent ratio of forward and backward steps for kinesin-1 [69], which could be approximated with

$$q(F) = q_0^{1-\frac{F}{F_\mathrm{s}}}, \tag{2.19}$$

where $q_0 \simeq 800$, see fig. 2.5(a). They found that this ratio $q(F)$ is not affected by the ATP concentration.

In general, motors under an external load force slow down. Increasing the load force F decreases the velocity until the average velocity is zero under stall force F_s. The precise shape of the force-velocity relation is different for different motor species [69, 91, 114]. Even for the same motor, different experimental groups came to different conclusions [69, 94–96]. As an example, the force-velocity relation for different ATP concentrations obtained by Carter and Cross [69] is shown in fig. 2.5(b).

In order to capture the main feature of a decreasing velocity with an increasing force, we choose as a first approximation a piecewise linear form for the force-velocity relation and will study different functional forms later. Such a force-velocity relation,

$$\mathcal{V}(F) \equiv \begin{cases} v & F < 0 \\ v(1 - F/F_\mathrm{s}) & 0 \le F < F_\mathrm{s} \\ 0 & F \ge F_\mathrm{s} \end{cases} \tag{2.20}$$

has a constant velocity v under assisting forces and backward steps are neglected, see fig. 2.6. In this way our force-velocity relation is determined by two parameters, the force-free single motor velocity v and the stall force F_s. These two parameters have been measured for different motors, see table 2.1. Further refinements of the force-velocity relation that, for example, include backward stepping, are possible and will be discussed in appendix A.5.

In general, one expects that the average motor velocity for fixed forces F increases in a Michaelis Menten like behavior with increasing ATP concentration [115]. Indeed, such behavior has been found for several motors [70, 116]. In experiments with single kinesin-1, it has been demonstrated that the average motor velocity decreases with increasing phosphate concentration as well as with increasing ADP concentration [117]. However, here, we only focus on the effect of the ATP concentration on the force-velocity relation. In general the force velocity relation is a function of the force and the ATP concentration, $\mathcal{V} = \mathcal{V}(F, [ATP])$. For a qualitative treatment, we write the dependence in a product of two

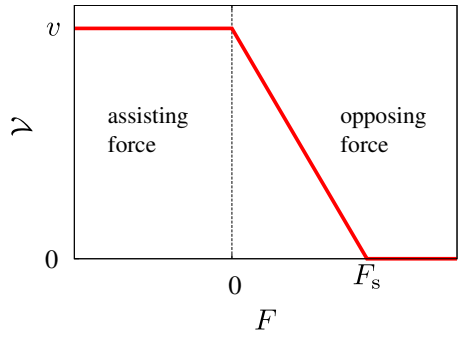

Figure 2.6 Simplified piecewise linear force-velocity relation as used in our reduced description. It is characterized by two parameters: the stall force F_s and the force free velocity v.

functions,

$$\mathcal{V}(F,[ATP]) = \mathcal{V}(F) \cdot K([ATP]). \tag{2.21}$$

We use the force-velocity relations of fig. 2.6 as $\mathcal{V}(F)$ and a Michaelis Menten like behavior for

$$K([ATP]) \equiv \frac{[ATP]}{[ATP] + K_M}, \tag{2.22}$$

with $K_M \simeq 100\,\mu M$, which is in the same order of magnitude for low forces as in [70]. The oversimplified [ATP] dependence of the force-velocity relation in eq. (2.21) captures the characteristic behavior of an increasing velocity that saturates with increasing the ATP concentration. However, a more complicated dependency has been revealed in experiments [70, 94] and theoretical studies considering the chemomechanical coupling of motor proteins [72, 73]. Different force-velocity relations can easily be incorporated into our description. As an example, an empirical [ATP] dependence based on kinesin-1 data is discussed in appendix A.6.

The unbinding rate and the detachment force

The force-dependent description of the unbinding rate $\epsilon_1(F)$ of eq. (2.14) involves two parameters: the force-free unbinding rate ϵ and the detachment force F_d. The unbinding rate ϵ is determined by the inverse of the force-free binding time t_1 of a single motor to the filament. Values for different motor species are summarized in table 2.1.

As already mentioned in section 2.2.1, the detachment force is related to the distance $x_b - x_0$ of the potential between the bound and unbound state. This distance is typically in the nanometer range and has been used to estimate a detachment force of $F_d = k_B T/(x_b - x_0) \simeq 3\,\mathrm{pN}$ for kinesin-1 [30].

In other studies, F_d has been used as a fit parameter in order to obtain a good agreement between a model and experimental data. For example in a gliding assay experiment with kinesin-1 a lower detachment force $F_d \simeq 1.8\,\mathrm{pN}$ has been determined from a fit [41]. In a

tug-of-war model, which successfully described the experimental data of Drosophila lipid-droplet transport, a dynein detachment force of $F_\mathrm{d} \simeq 1.1\,\mathrm{pN}$ has been used [31]. The detachment force for myosin V, $F_\mathrm{d} \simeq 4\,\mathrm{pN}$, and for myosin VI, $F_\mathrm{d} \simeq 2.6\,\mathrm{pN}$ have been estimated recently to explain the trajectories of a tug-of-war between these two motors [101].

However, in general the whole shape of the unbinding rate $\epsilon_1(F)$ can be obtained experimentally. One method is to measure the life time of the motor-filament bond under various constant loads F. In studies of molecular bonds a widely used method is to pull at constant speed on the molecular complex and measure the distribution of rupture forces [84]. The average life time for a constant load can directly be obtained from these rupture force distribution [118]. It has been shown for kinesin-1 and myosin V, that the rupture force distributions depend on the pulling direction [102, 119, 120] . As a consequence, the detachment force could be also different for assisting forces and opposing forces. Such mechanical differences has been discussed to explain the intrinsic directionality of processive motors. In the last decades, a lot of work has been done, mainly with kinesin-1, to reveal the precise mechanism of the coordination of the two motor heads that leads to processive movement. Not only different nucleotide states of the heads,[2] but also mechanical strain forces between the heads are necessary for breaking the symmetry [120, 121]. In this way, the probability to detach is higher for the trailing head during double-headed binding than for the leading head. This dependence of the kinesin-microtubule binding on both the nucleotide state and the loading direction has been explicitly demonstrated for single headed motors [119]. In a later experiment, the same group studied both the equilibrium of and transition between single- and double-headed binding of kinesin and found that the unbinding force obtained by loading directed toward the minus end of microtubule was 45% greater than that for plus end-directed loading [102]. This is consistent with the idea that unbinding for the trailing head, which feels a load in the plus direction, is more probable than for the leading head. Conclusively, it is plausible to introduce a direction dependent detachment force and study its influence on the dynamics of a motor pair, as we will present in section 3.4.4.

Elastic motor linkers

In general, the elasticity of the elements between the cargo and the motor heads is very complicated. For example, the stalk of kinesin-1 consists of different coiled-coils and flexible regions, see fig. 2.7. All these region contribute to the overall elasticity of the motor. Although the elastic details of motor stalks are, in principle, accessible in experiments with atomic force microscopy (AFM), a detailed force extension relation has only been reported for muscle myosin II to our knowledge [123]. For other motors, the elasticity has been determined indirectly, mostly from bead fluctuations in optical traps. Kawaguchi et al. found a simple linear force extension relation with a spring constant of $\kappa \simeq 0.5\,\mathrm{pN/nm}$ for kinesin-1 [102]. In contrast, Coppin et al. determined a non-linear behavior which saturates at $\kappa \simeq 0.3\,\mathrm{pN/nm}$ [96]. Furthermore, a study of kinesin-1 combining molecular dynamic

[2] Nucleotide states of the heads are chemical states associated with the type of nucleotide (ATP, ADP-Pi, ADP) that is bound to the head.

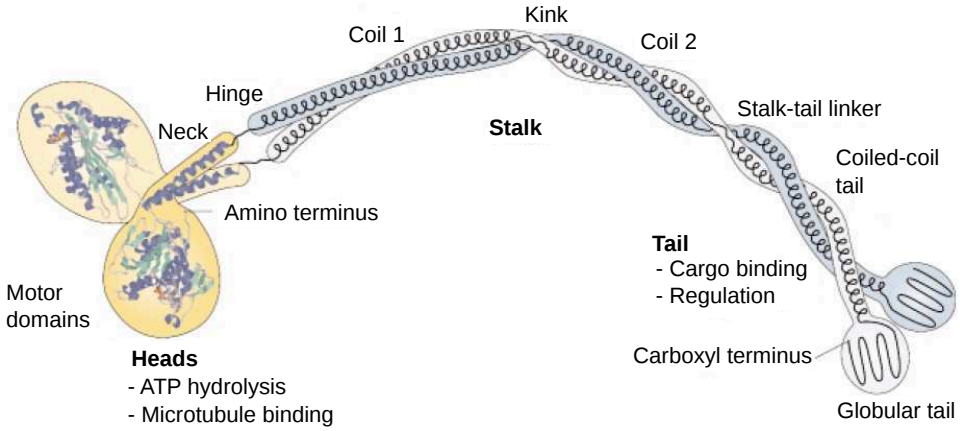

Figure 2.7 Overview of the domain organization of kinesin-1 taken from [122]. Stalk and tail consist of different elastic regions (coil 1, coil 2, coiled-coil tail) and very flexible joints (hinge, kink, stalk-tail linker)

simulations with experimental data, suggested a cable like behavior, with a small stiffness in the compression mode and a constant stiffness of 0.3 pN/nm for stretching [124].

In several optical trapping experiments, the compliance between the bead and the filament has been estimated for several different species of motors. The typical values are of the order of pN/10nm, see table 2.1.

To account for the non-linearity and the finite length of the motor stalk, we introduced the FJC and the WLC model in section 2.2.1. Both models are based on two parameter. One is the contour length L_c that is the maximal extension of the molecule. The other one is the segment length L_s for the FJC model and the persistence length L_p for the WLC model. We relate the later two parameter to the stiffness κ by requiring the linear behavior, $F \approx \kappa \Delta x$, for small extensions. This constrain leads to a segment length

$$L_s = \frac{3k_B T}{L_c \kappa} \tag{2.23}$$

and a persistence length

$$L_p = \frac{3k_B T}{2L_c \kappa}. \tag{2.24}$$

By comparing these two equation, one finds the general relation $2L_p = L_s$ which is also called the Kuhn length [3]. For a rough estimate of the order of magnitude for the contour length, we assume that there are no folded domains in the stalk. Then, a reasonable maximal extension is 50% of the molecule length which is known from electron microscopy. The length of myosin V and kinesin-1 are similar between $60 - 100\,\text{nm}$ [12, 107], whereas the molecular length of dynein is $35 - 50\,\text{nm}$ [106]. From these considerations a contour length of $20 - 80\,\text{nm}$ seems reasonable.

2.3. Mathematical description of transport by motors

In cellular biological systems, on small length scales, typically processes are influenced by the thermal environment. The resulting stochasticity requires a probabilistic description. Methods for studying stochastic processes are discussed in several textbooks [85,86,125]. In the following, we review continuous-time Markovian dynamics for describing such stochastic processes. Furthermore, for calculating averaged quantity of time dependent processes, we explain a method introduced by Hill in the 1980ies [126–128]. Additionally, we introduce a generalization of this method, which is necessary to establish a general framework for the description of transport by molecular motors.

2.3.1. Discrete state space with continuous-time Markovian dynamics

In order to develop an appropriate theoretical description, one has to choose a state space and the dynamics on that state space. However, it is not straightforward to find a state space which, on the one hand, accounts for the characteristic behavior of the system and on the other hand is still manageable to get an intuitive understanding. Since in experiments usually the position of the cargo over time is measured, we focus on the cargo and we introduce a discrete state space for the cargo. We associate the states with a discrete physical quantity, such as the number of active motors or an effective number of steps between two active motors. We denote the states by (i), where i numerates for example the states from 0 to N. Next, we specify the propagation of the system in time on the introduced state space. The time evolution of such a system can be represented by $X(t)$, which is the state of the system at time t. Since $X(t)$ describes a stochastic process, we can only predict its time evolution probabilistically. We consider the dynamics as a continuous-time random process with the Markov property. The Markov property implies a memoryless stochastic process, meaning that its future only depends on the present state and not on its history. This can be formally expressed with conditional probabilities, i.e.,

$$p[X(t) = j | X(s) = i, X(t_{n-1}) = i_{n-1}, \ldots, X(t_1) = i_1] = p[X(t) = j | X(s) = i], \tag{2.25}$$

where $0 \leq t_1 \leq t_2 \leq t_3 \leq \ldots t_{n-1} \leq s \leq t$ is a non-decreasing sequence of times and $i_1, i_2 \ldots i_{n-1}, i, j$ are any states in the state space. Despite of its simplicity, this *ab initio* assumption has proved to be useful in many cases when constructing a theoretical description for stochastic processes, especially in the context of molecular motors [30,31,72,73,77]. The system attains different states over time. A system in state (i) makes a transition to the next state (j) according to a transition probability $W(i, j)$. Once the system is in a state (i) it sojourns in this states according to a sojourn time distribution also called waiting time distribution. The only waiting time distribution with a Markov property in continuous time is an exponential distribution [129] with a probability density function

$$\psi_i(t) = \frac{1}{\langle \Delta t_i \rangle} e^{-t/\langle \Delta t_i \rangle}, \tag{2.26}$$

where $\langle \Delta t_i \rangle$ is the average waiting time in state (i). The probability that the system waits the time τ in state (i) and changes to state (j) over time t is then given by

$$p[\tau \leq t]W(i,j) = \int_0^t \frac{1}{\langle \Delta t_i \rangle} e^{-t'/\langle \Delta t_i \rangle} dt' W(i,j) = (1 - e^{-t/\langle \Delta t_i \rangle}) W(i,j). \tag{2.27}$$

For later purposes, we expand this equation in a Taylor series for small $t = \delta t$,

$$p[\tau \leq \delta t]W(i,j) \approx \frac{W(i,j)}{\langle \Delta t_i \rangle} \delta t. \tag{2.28}$$

We define the transition rate

$$\omega_{ij} \equiv \frac{W(i,j)}{\langle \Delta t_i \rangle} \tag{2.29}$$

for a transition from state (i) to state (j) with the property that $\omega_{ii} = 0$. Thus $\omega_{ij}\delta t$ is the probability that a transition from state (i) to state (j) occurs in the time interval δt.

In order to derive a differential equation describing the time evolution, we consider a three point process $\{X(t) = j, X(s) = i, X(0) = z\}$ with $0 \leq s \leq t$. Its probability can be written using the Markov property (2.25) as

$$\begin{aligned} &p[X(t) = j, X(s) = i, X(0) = z] = \\ &\qquad p[X(t) = j | X(s) = i] p[X(s) = i | X(0) = z] p[X(0) = z] \end{aligned} \tag{2.30}$$

By summing this equation over i, we eliminate the state $X(s)$ on the left hand side,

$$\begin{aligned} &p[X(t) = j, X(0) = z] = \\ &\qquad \sum_i p[X(t) = j | X(s) = i] p[X(s) = i | X(0) = z] p[X(0) = z]. \end{aligned} \tag{2.31}$$

From the definition of the conditional probability, $p(A|B) = p(A \cap B)/p(B)$ [129], i.e., $p[X(t) = j | X(0) = z] = p[X(t) = j, X(0) = z]/p[X(0) = z]$, we obtain the discrete form of the Chapman-Kolmogorov equation [85]

$$p[X(t) = j | X(0) = z] = \sum_i p[X(t) = j | X(s) = i] p[X(s) = i | X(0) = z]. \tag{2.32}$$

Next, we consider this equation for a small time step, such that $t = s + \delta t$,

$$p[X(s + \delta t) = j | X(0) = z] = \sum_i p[X(s + \delta t) = j | X(s) = i] p[X(s) = i | X(0) = z] \tag{2.33}$$

Now, we use the Taylor expansion of eq. (2.28) and the definition of the transition rates from eq. (2.29) to rewrite the conditional probability for small δt as

$$p[X(s + \delta t) = j | X(s) = i] = \left(1 - \sum_k \omega_{ik} \delta t\right) \delta_{ij} + \omega_{ij} \delta t + \mathcal{O}(\delta t^2), \tag{2.34}$$

where δ_{ij} is the Kronecker symbol. The parenthesized expression is the probability of staying in state (i) after the time interval δt and $\omega_{ij}\delta t$ is the probability for a transition from state (i) to state (j) during the time δt. Putting this expansion into eq. (2.33), we obtain after rearranging,

$$\frac{p[X(s+\delta t)=j|X(0)=z]-p[X(s)=j|X(0)=z]}{\delta t}= \sum_i \omega_{ij} p[X(s)=i|X(0)=z]-\sum_k \omega_{jk} p[X(s)=j|X(0)=z]. \tag{2.35}$$

Taking the limit $\delta t \to 0$, we derive the master equation [86]

$$\frac{dp_j(t)}{dt}=\sum_i p_i(t)\omega_{ij}-\sum_i p_j(t)\omega_{ji}, \tag{2.36}$$

where $p_i(t)$ is a simplified notation for the probability of being in state (i). We like to emphasize here, that in our theoretical description, we use the master equation as the fundamental equation for the time evolution of probabilities. In general, the solution of this differential equation depends on the initial condition. If the probabilities $p_i(t)$ are time independent, the stochastic process is called stationary or in other words the system is in a steady state. We denote such time independent probabilities P_i.

A convenient way for illustrating a finite state space with possible transitions is a network representation. Each state corresponds to a node and the transitions are represented as directed arrows weighted with the transition rate, see fig. 2.8(a). A state is called an absorbing state, if there are only transitions going into that state and no transition going out of it, like state (0) in the network shown in fig. 2.8(a). Once the system reaches an absorbing state, it is trapped, since there are no transitions going out of that state. A meaningful steady state solution does not exist for a network with absorbing states. However, in the 1980ies Hill introduced a framework to study networks with absorbing states, which we will briefly review in the next section. Other standard methods to treat master equations, involve matrix algebra can be found in textbooks [85, 86].

2.3.2. The average time to absorption: Hill's method

Certain averaged quantities, such as the average time to absorption or the average number of visits to a state before absorption, are of particular interest. For example, in the context of transport by molecular motors, the average time to absorption is associated with the binding time of the cargo to the filament. Such averaged quantities can be derived from a steady state probability distribution of a modified network without the absorbing states [126–128]. This method introduced by Hill is based on the idea of replacing time averages by ensemble averages. For networks with absorbing states, these averages depend on the initial condition. Before we introduce a generalization of Hill's method for the average absorption time for arbitrary initial conditions, we give a rather intuitive explanation of the method by considering the time to absorption for a simple three state system with one absorbing state

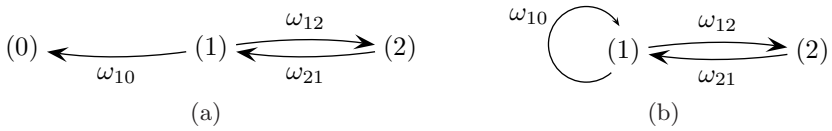

Figure 2.8 Network representation of a three state system with one absorbing state (0). (a) Original network with absorbing state (0) and starting state (1), in which all runs start. The time dependent state probability distribution for this network is denoted $p_i(t)$. (b) Closed network, where the absorbing state (0) is eliminated by redirecting the arrow going into the absorbing state to the starting state (1). The steady state distribution of this closed network is denoted by P_i. Note, the self loop with the transition rate ω_{10} does not contribute to the P_i.

(0) shown in fig. 2.8(a). The process always starts in state (1). The average time spent in one of the non-absorbing states before absorption is given by,

$$\tau_i \equiv \int_0^\infty p_i(t)dt \quad \text{for } i = 1, 2 \tag{2.37}$$

where $p_i(t)$ is obtained from the time dependent solution of the master equation. Summing up all times spent in non-absorbing states gives the average time to absorption,

$$\langle \Delta t \rangle = \sum_{i=1}^{2} \tau_i = \sum_{i=1}^{2} \int_0^\infty p_i(t)dt. \tag{2.38}$$

Here the $p_i(t)$ are the ensemble-average state probabilities at time t. Now, we explain how to derive the average time to absorption using time averages instead of ensemble averages. Instead of considering an ensemble of runs from start to end, we follow a single system over a long time. This system immediately starts a new run when it reaches the absorbing state (0), which is equivalent to concatenating the trajectories of the original runs. A network that represents such a repeating process is constructed by 'closing' the network of fig. 2.8(a), i.e., by eliminating the absorbing state (0) and redirecting all arrows that end in state (0) to the starting state (1), see fig. 2.8(b). We denote the time-averaged state probabilities P_i of the closed network. It can be obtained from the corresponding steady state master equation. In the original network including the absorbing state, P_i is the probability of being in state (i) before absorption. Therefore, the probability P_i can be written in terms of the relative time that the system sojourns in state (i) before absorption, leading to

$$P_i = \frac{\tau_i}{\langle \Delta t \rangle} = \frac{1}{\langle \Delta t \rangle} \int_0^\infty p_i(t)dt, \tag{2.39}$$

where τ_i is the average time spent in state (i) and $\langle \Delta t \rangle$ is the time to absorption. Note, from the normalization $\sum P_i = 1$ follows eq. (2.38).

Now, the average time to absorption is the inverse rate of arrivals in the absorbing state (0), which is connected to the probability current $J \equiv P_1 \omega_{10}$. Thus, we obtain the average

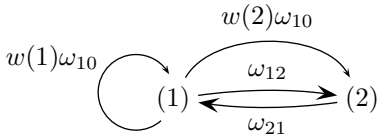

Figure 2.9 Closed network of the original network of fig. 2.8(a), taking a new initial probability distribution into account. Runs start with probability $w(1)$ in state (1) and with $w(2) = 1 - w(1)$ in state (2). To close the network, we duplicate the arrow going into the absorbing state and redirect it to each of both starting states (1) and (2). The new transitions have to be weighted with the initial probabilities $w(1)$ and $w(2)$.

time to absorption

$$\langle \Delta t \rangle = \frac{1}{J} = \frac{1}{P_1 \omega_{10}}. \tag{2.40}$$

Note, this equation only depends on the steady state probability P_1 of the closed network. Obtaining steady state probabilities from the master equation is in general more convenient than solving the time dependent master equation for the $p_i(t)$. In addition to the standard linear algebra methods for obtaining the steady state solution of the master equation [86], a powerful diagrammatic method has been proposed [130, 131].

2.3.3. Generalization of Hill's method to arbitrary initial conditions

Hill's method for the average absorption time applies only for networks with several absorbing states and one initial starting state [126–128]. We introduce a to our knowledge novel generalization of Hill's method for the average absorption time for several starting states. We consider the three state system of fig. 2.8(a) with a new initial condition: the process starts with probability $w(1)$ in state (1) or with probability $w(2) = 1 - w(1)$ in state (2). When closing this network, the initial condition has to be taken into account. The arrow going into the absorbing state has to be redirected to both starting states (1) and (2) weighted with the starting probabilities $w(1)$ and $w(2)$ respectively, see fig. 2.9. Such a closed network gives the correct state probability distribution in the steady state from which we obtain the average time to absorption according to eq. (2.40). Note that P_1 now depends on the initial probabilities $w(1)$ and $w(2)$.

In the following, we mathematically derive the average time to absorption for a general network with several absorbing states and an initial probability distribution for several starting states. We assume that all states of the network are connected. Next, we divide the states into four different sets: (i) set $\mathcal{B}$ contains all states; (ii) subset $\mathcal{A}$ contains all absorbing states; (iii) subset $\mathcal{S}$ contains all starting states and (iv) subset $\mathcal{A}'$ contains all states with at least one transition into an absorbing state. Obviously, the two sets $\mathcal{A}'$ and $\mathcal{A}$ are mutually disjoint, $\mathcal{S}$ and $\mathcal{A}$ are disjoint sets as well, whereas, in general, $\mathcal{S}$ and $\mathcal{A}'$ may have a non empty intersection.

We start with the master equation for a state $(s) \in \mathcal{S}$ of the original network,

$$\frac{dp_s(t)}{dt} = \sum_{j\in\mathcal{B}} p_j(t)\omega_{js} - \sum_{j\in\mathcal{B}} p_s(t)\omega_{sj} \tag{2.41}$$

and integrate this equation over t, leading to

$$p_s(\infty) - p_s(0) = \sum_{j\in\mathcal{B}} \omega_{js} \int_0^\infty p_j(t)\,dt - \sum_{j\in\mathcal{B}} \omega_{sj} \int_0^\infty p_s(t)\,dt. \tag{2.42}$$

Because $(s) \notin \mathcal{A}$, we know that $p_s(\infty) = 0$. Multiplying by $1/\langle\Delta t\rangle$ and using eq. (2.39) yields

$$-\frac{p_s(0)}{\langle\Delta t\rangle} = \sum_{j\in\mathcal{B}} P_j\omega_{js} - \sum_{j\in\mathcal{B}} P_s\omega_{sj}. \tag{2.43}$$

Now, we add the sum of all probability currents $p_s(0)\sum_{a'\in\mathcal{A}'}\sum_{a\in\mathcal{A}} P_{a'}\omega_{a'a}$ from the redirected arrows of the closed network which are weighted with the initial probability distribution $p_s(0)$ and obtain

$$\begin{aligned} -\frac{p_s(0)}{\langle\Delta t\rangle} + p_s(0)\sum_{a'\in\mathcal{A}'}\sum_{a\in\mathcal{A}} P_{a'}\omega_{a'a} &= \sum_j P_j\omega_{js} - \sum_j P_s\omega_{sj} + p_s(0)\sum_{a'\in\mathcal{A}'}\sum_{a\in\mathcal{A}} P_{a'}\omega_{a'a} \\ &= 0. \end{aligned} \tag{2.44}$$

The right hand side of this equation vanishes, because we recover the steady state equation for state (s) of the closed network. Hence the left hand side of eq. (2.44) gives

$$\frac{1}{\langle\Delta t\rangle} = \sum_{a'\in\mathcal{A}'}\sum_{a\in\mathcal{A}} P_{a'}\omega_{a'a}. \tag{2.45}$$

Then, the average time to absorption reads

$$\langle\Delta t\rangle = \frac{1}{\sum_{a\in\mathcal{A}} J_a}, \tag{2.46}$$

where J_a is the total probability current into the absorbing state (a).

2.3.4. The average run length of a cargo

As mentioned above, molecular motors unbind from their filament after a finite run length. As a consequence, cargo particles also unbind. The distance covered by these particles can be obtained in experiments and from our description. In order to obtain the average run length of a cargo, one has to assign the dynamics of a spatial coordinate x to every state (i). This dynamic can either be stochastic or deterministic. For a deterministic motion, we assign a constant velocity v_i to every state (i). Since we know the time spent in state

(i) before absorption $\tau_i = \langle \Delta t \rangle P_i$, where P_i is the steady state probability of the closed network, we obtain the average run length as

$$\langle \Delta x_{\mathrm{ca}} \rangle = \sum_i \tau_i v_i = \langle \Delta t \rangle \sum_i v_i P_i. \tag{2.47}$$

In order to treat the spatial coordinate stochastically, we introduce the probability distribution $p_i(x,t)$. For state (i), the time evolution of the probability distribution $p(x,t)$ is governed by the Fokker-Planck equation [125]. The form of the Fokker-Planck equation that we use is only valid under two assumptions. First, the noise resulting from the thermal environment has to be uncorrelated. Second, the coordinate x is over-damped, meaning that friction dominates in such a way that the momenta relax very fast. The time evolution of the probability distribution $p(x,t)$ of a particle with friction coefficient γ and diffusion coefficient D in a potential $V(x)$ is given by

$$\partial_t p(x,t) = \mathcal{L} p(x,t), \tag{2.48}$$

where $\mathcal{L} \equiv \partial_x[(\partial_x V(x)/\gamma) + D\partial_x]$ is the usual Fokker-Planck operator. A purely diffusive motion is represented by

$$\mathcal{L} = D\partial_x^2 \tag{2.49}$$

and a deterministic motion with constant velocity v_i by

$$\mathcal{L}_i = -\partial_x v_i. \tag{2.50}$$

In this way, we describe the time evolution of the spatial coordinate for a fixed state (i) with a Fokker-Planck operator $\mathcal{L}_i$. Now, we extend the master equation eq. (2.36) to take the evolution of this coordinate explicitly into account, leading to

$$\partial_t p_i(x,t) = \sum_j p_j(x,t)\omega_{ji} - \sum_j p_i(x,t)\omega_{ij} + \mathcal{L}_i p_i(x,t). \tag{2.51}$$

In our description we only deal with Fokker-Planck operators of the type as in eq. (2.49) and eq. (2.50). Together with an initial condition, this set of ordinary differential equations can be transformed into a set of linear equations using the Fourier-Laplace transform

$$\hat{p}_i(k,\lambda) \equiv \int_{-\infty}^{+\infty} \int_0^{+\infty} p_i(x,t)\, e^{\mathrm{i}kx - \lambda t} dt\, dx. \tag{2.52}$$

In networks with absorbing states, the average time to absorption and the average run length is obtained from derivatives of the Fourier-Laplace transform of the time dependent probability current into the absorption state

$$\hat{J}(k,\lambda) = \sum_{a' \in \mathcal{A}'} \sum_{a \in \mathcal{A}} \hat{p}_{a'}(k,\lambda)\omega_{a'a}, \tag{2.53}$$

where $\mathcal{A}$ is the set containing all absorbing states and $\mathcal{A}'$ contains all states with a transition into an absorbing state. Thus, the average binding time is given by

$$\langle \Delta t_{\mathrm{ca}} \rangle = \int_{-\infty}^{+\infty} \int_{0}^{+\infty} t\ J(x,t) dt\, dx = -\partial_\lambda \hat{J}(0,\lambda)|_{\lambda=0} \tag{2.54}$$

and the average run length is given by

$$\langle \Delta x_{\mathrm{ca}} \rangle = \int_{-\infty}^{+\infty} \int_{0}^{+\infty} x\ J(x,t) dt\, dx = -\mathrm{i}\partial_k \hat{J}(k,0)|_{k=0}, \tag{2.55}$$

For a specific network, these two equation yield the same result as eq. (2.46) and eq. (2.47) and provide a non-trivial check of the derivation using closed networks. However, the advantage of taking explicitly care of the spatial coordinate is to obtain some information about $p(x,t)$ that we will need in the following subsection.

2.3.5. Two different average velocities of the cargo

When validating a theoretical description with experimental data, one would like to compare as many quantities as possible. The average velocity defined as

$$v_{\mathrm{ca}} \equiv \frac{\langle \Delta x_{\mathrm{ca}} \rangle}{\langle \Delta t_{\mathrm{ca}} \rangle} \tag{2.56}$$

does not yield any new information when the average run length $\langle \Delta x_{\mathrm{ca}} \rangle$ and the average binding time $\langle \Delta t_{\mathrm{ca}} \rangle$ is already known. However, we can define a different average velocity as the average of the velocities of the single trajectories,

$$\langle v \rangle_{\mathrm{ca}} \equiv \left\langle \frac{\Delta x_{\mathrm{ca}}}{\Delta t_{\mathrm{ca}}} \right\rangle. \tag{2.57}$$

In general $\langle v \rangle_{\mathrm{ca}} \neq v_{\mathrm{ca}}$. We derive $\langle v \rangle_{\mathrm{ca}}$ from the Fourier-Laplace transform as

$$\langle v \rangle_{\mathrm{ca}} = \int_{-\infty}^{+\infty} \int_{0}^{+\infty} \frac{x}{t}\ J(x,t) dt\, dx = -\mathrm{i} \int_{0}^{+\infty} \partial_k \hat{J}(k,\lambda)|_{k=0}\, d\lambda. \tag{2.58}$$

This averaging of the velocities provides a new quantity which can be evaluated from run time and run length measurements of a specific system and thus compared to a theoretical description as we will do in chapter 4, see eq. (4.28).

2.4. Summary

In this chapter, we have introduced a reduced single motor description, which includes the basic motor dynamics of stepping along, binding to and unbinding from the filament. This description is based on several parameters and force-dependencies, which can be determined by single molecule experiments. Numerical parameters as obtained from such experiments

are summarized in table 2.1. Furthermore, we have presented the mathematical framework based on continuous-time Markovian dynamics and an extension of Hill's method for the average absorption time that we use to describe cargo transport in general.

In the following chapters, we use the reduced single motor description to study transport by the cooperative action of molecular motors. In this way, we are able to explain and predict cooperative transport behavior based on a single motor description, which is fully consistent with the available experimental data.

3. Cargo transport by two identical motors

In this chapter, we develop a systematic theory for two elastically coupled motors and show that this system exhibits four different transport regimes: one regime of weak coupling without motor-motor interference and *three distinct regimes of interference*. Some of these regimes have been discussed separately in previous experimental [24, 25] and theoretical studies [30, 43–47, 132–134]. We present a unifying theory based on timescale arguments for the strain force generation of a motor pair. In general, these arguments are independent of the details of the model and therefore suitable to explain why different previous studies came to different results. Furthermore, based on this description, we use single motor properties as determined experimentally to quantitatively predict the effects of mutual interference for several species of molecular motors. We discuss refinements of our single motor description such as different shapes of force-velocity relations and non-linear elastic motor linkers, just to mention two. As a relevant example, we apply our theory to explain quantitatively the results of experiments with two coupled kinesin-1 motors from the Diehl lab [25]. Finally, we implement our results into a general framework to determine observables of a cargo transported by two motors.

3.1. Previous studies

Experimental methods for studying single motor molecules or motility driven by a large number of motors are nowadays routinely used in many labs. However, for intermediate motor numbers, it is still challenging to set up experiments in which the number of involved motors is known precisely [39]. In several studies, the average number of motors has been estimated from different methods, such as combination of light scattering and theoretical analysis [24], force measurements [40] and biochemical analysis with modeling [28]. Qualitatively, an increase in the cargo run length has been known for a long time [36, 74], but a detailed explanation how this increase is related to the number of motors is difficult, since the exact number of motors is unknown. Nevertheless, the run length distributions of beads covered with different numbers of kinesin-1 have successfully been recovered theoretically by assuming no interaction between the motors [24]. In this study, however, only the average number of motors could be determined and the actual number of engaged motors varied from bead to bead. Furthermore, the precise geometric arrangement of the motors was not known. These difficulties have been overcome in a recent study that used synthetic complexes of two kinesin motors connected by a rigid DNA scaffold [25]. The group found that the binding time of both motors was substantial smaller than expected for non-interacting motors. This indicates a strong interference between the motors in a sense that they pull each other from the filament. However, the average velocity of the cargo was the

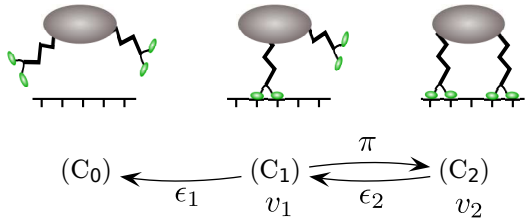

Figure 3.1 Activity states of a cargo transported by two identical motors. The cargo is pulled by one active motor (in state (C_1)), by two active motors (in state (C_2)) or unbinds from the filament into the absorbing state (C_0).

same whether it was transported by one motor or by two. In contrast, in a gliding assay experiment, a reduced velocity has been reported that results from mutual motor-motor interference induced by elastic strain force generation [41]. All of these results indicate that the motors interfere in various ways with different impact on the transport properties. Much theoretical work has been devoted to elucidate cooperative transport by molecular motors [30, 43–47, 132–134]. In some of these studies interference has been found, but not in others. Prior to discussing these issues in more detail, we review a general framework to describe cargo transport by two identical motors.

3.1.1. Semi-stochastic description of cargo transport by two identical motors

In this section, we review the theoretical description of a cargo transported by two identical motors, which also serves as a common ground to compare different experimental and theoretical studies. The model we use is a special case of a general description of cargo transport by several molecular motors [30]. This framework is quite general. It relates experimentally accessible quantities like the average and the distribution of the run length to general transition rates. Whether the motors interfere or act independently depends on the numerical values of these rates.

As mentioned in section 2.2.1, a motor with a cargo binds to the filament, walks along its track in a directed way, and unbinds from it. We characterize the cargo state space by the number of active motors, see fig. 3.1. We call these states activity states (C_i). In state (C_1), the cargo is transported by only one active motor and in state (C_2) both motors are active. Since we want to describe the motion of the cargo on length scales that are large compared to the motor step size l, we associate a deterministic velocity v_1 and v_2 with the cargo states (C_1) and (C_2), respectively. Since it is not likely that both motors unbind exactly at the same time, we assume that the cargo unbinds from the filament into the absorbing state (C_0) only from the state in which one motor is active. Following this description, the transition from state (C_1) into the absorbing state (C_0) is described by the unbinding rate of a single motor ϵ_1. When one motor is active, the other motor can bind with the binding rate π and the cargo is in state (C_2). The transition from state (C_2) back to state (C_1) is associated with the effective unbinding rate ϵ_2 of a motor of a motor pair. We assume

that an unbound cargo first binds with one motor into the state (C_1). With this initial condition, the average run time or binding time of the cargo $\langle \Delta t_{\mathrm{ca}} \rangle$ is obtained from closing the network of fig. 3.1 as described in section 2.3.2 and is given by

$$\langle \Delta t_{\mathrm{ca}} \rangle \equiv \frac{\pi + \epsilon_2}{\epsilon_1 \epsilon_2}. \tag{3.1}$$

We determine the average run length

$$\langle \Delta x_{\mathrm{ca}} \rangle \equiv \frac{\pi v_2 + \epsilon_2 v_1}{\epsilon_1 \epsilon_2}, \tag{3.2}$$

as described in section 2.3.4. The distributions of these quantities can be also calculated analytically as presented in [30] and given in appendix A.1. We obtain the average velocity from eq. (3.1) and eq. (3.2),

$$v_{\mathrm{ca}} \equiv \frac{\langle \Delta x_{\mathrm{ca}} \rangle}{\langle \Delta t_{\mathrm{ca}} \rangle} = \frac{\pi v_2 + \epsilon_2 v_1}{\pi + \epsilon_2}. \tag{3.3}$$

All of these experimentally accessible quantities depend on the transition rates. The state (C_1) is equivalent to the situation of a cargo transported by only one motor. Therefore, the values for the unbinding rate ϵ_1 and the velocity v_1 can be taken from single molecule experiments, see section 2.2.2. Numerical values for the binding rate π are also discussed in section 2.2.2. The parameters ϵ_2 and v_2 that characterize state (C_2), depend, in general, on the dynamical parameters of a single motor and on the interaction between the motors. In the case of cargo transport by two motors, the average time that both motors are bound simultaneously to the filament is given by $t_2 \equiv 1/\epsilon_2$. As mentioned at the beginning of this chapter, different studies obtained different values for t_2 and v_2 indicating either no interaction or a motor-motor interference, which we briefly review in the following.

3.1.2. Different studies, different results

Bead experiments with a small number of motors could be fitted consistently with a model based on non-interacting motors [24]. In this case, $\epsilon_2 = 2\epsilon_1$, since the rate for an unbinding event when both motors are active, equals the sum of the single rates [30]. Under no external force, the velocities for non-interacting motors do not depend on the state of the cargo, i.e. $v_2 = v_1$. In an experiment with two coupled kinesin-1 motors, the Diehl lab was able to estimate ϵ_2 and v_2 directly from the trajectories of the motor pair [25]. Although there was almost no effect on the velocity, $v_{\mathrm{ca}} = v_1$, the unbinding rate ϵ_2 was found to be six times greater than the single unbinding rate, $\epsilon_2/\epsilon_1 \simeq 6$. These findings suggest a strong interference between the motors.

Likewise, theoretical studies stimulated by these experiments show different results. In some cases, interference between the motors could be found to affect the velocity and/or the binding time t_2 and thus the run length of the cargo [25,44,46,47,132], but not in other cases [43,45,133]. A systematic description of two interacting molecular motors, which also leads to an intuitive understanding, is necessary to obtain a consistent picture of cooperative

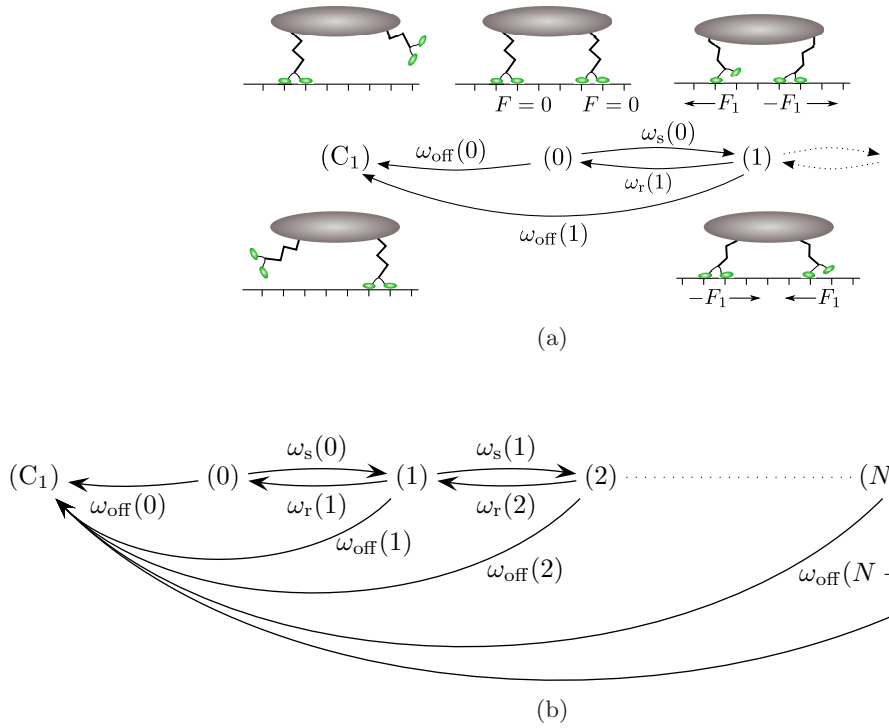

Figure 3.2 (a) State space with corresponding motor configurations. In state (C_1), only one of the two motors is active. In state (0), the motors are bound with relaxed linkers in such a way, that there is no force between the motors. When the motors step either towards each other or away from each other, a strain force is generated between them, like in state (1); two motor configurations correspond to this state. (b) Reduced state space for a cargo simultaneously transported by two motors. The cargo is transported by a single motor in state (C_1). The numbered states $(0)\dots(N)$ correspond to the effective extension of the linkers between the motors, when both are bound to the filament. Since it is not likely that both motors unbind exactly at the same time, one of both motors unbinds from the numbered states $(0)\dots(N)$ to the single motor state (C_1).

transport. In the following, we introduce a microscopic model on the level of the individual motors to determine t_2 and v_2 from well established single motor properties. Thus, we explain the emergence of different motor-motor interference and clarify the inconclusive theoretical results of different studies.

3.2. Motor pair description

Let us introduce a microscopic description to calculate the motor pair parameters t_2 and v_2. We focus on the activity state (C_2) in detail. In this state, both motors are bound to the filament and pull on the cargo together. The cargo then mediates an interaction

between the motors, which we model as the stretching of an elastic element associated with the motor linkers, see fig. 3.2(a). The elastic force generated in this flexible element is a function of the extension. Because of the discrete stepping of the motors the extension Δx_i is a discrete quantity, and thus the elastic force is defined as

$$F_i \equiv F(\Delta x_i). \tag{3.4}$$

When motors that start in the state (0), in which both linkers are relaxed, step either towards each other or away from each other, the linkers are stretched, see fig. 3.2(a).[1] In this way, a motor step leads to stretching or relaxation of the two linkers and thereby to a displacement of the cargo. Note, we do not consider steric effects between the motors as theoretically studied in [132]. Here, we rather assume that the distance between the attachment points of the motors on the cargo is larger than twice the maximal extension of their linkers or that the motors walk on different filaments or protofilaments next to each other.

To calculate t_2 and v_2, we describe the cargo in the state space of the discrete extension of the linkers, see fig. 3.2(b). We assign to every state $(0)\ldots(N)$ the forces F_i acting on the motors. In state (0), the linkers are relaxed. If one of the motors steps forward or backward, the absolute extension of both linkers increases by the motor step size l and the cargo is in state (1). For identical motors, each linker is stretched by $l/2$. This stretching induces an elastic force between the motors. One motor feels the force $F_1 = F(l/2)$ and the other motor feels the opposing force $-F_1 = -F(l/2)$. This force symmetry arising from Newton's *actio est reactio* principle is very important for developing an intuitive understanding of the system, as we will see later on. Since we know, from section 2.2.1, the dynamics of a single motor subject to an external force, we are able to assign rates to every state (i). We denote the transition rates for stretching of the linkers by $\omega_\mathrm{s}(i)$, and by $\omega_\mathrm{r}(i)$ for their relaxation. These transition rates can be written in terms of forward and backward stepping rates of the single motors. When the cargo is in state (0) with both linkers relaxed, the force on each motor is zero, $F(0) = -F(0) = 0$. From this state (0), there are four possible pathways to state (1): either one motor steps forward or backward or the other motor steps forward or backward and thus

$$\omega_\mathrm{s}(0) \equiv 2[\alpha(0) + \beta(0)]. \tag{3.5}$$

For the other states $i \neq 0$, the transitions are governed by the rates

$$\omega_\mathrm{s}(i) \equiv \alpha(F_i) + \beta(-F_i) \tag{3.6}$$

and

$$\omega_\mathrm{r}(i) \equiv \alpha(-F_i) + \beta(F_i). \tag{3.7}$$

Beside stepping, motors also unbind from their filaments. Since it is not likely that both motors unbind exactly at the same time, we introduce transitions from every state $(0)\ldots(N)$

[1] Since the cargo is rigid and able to move perpendicular to the filament, the motor linkers are stretched even when they walk towards each other.

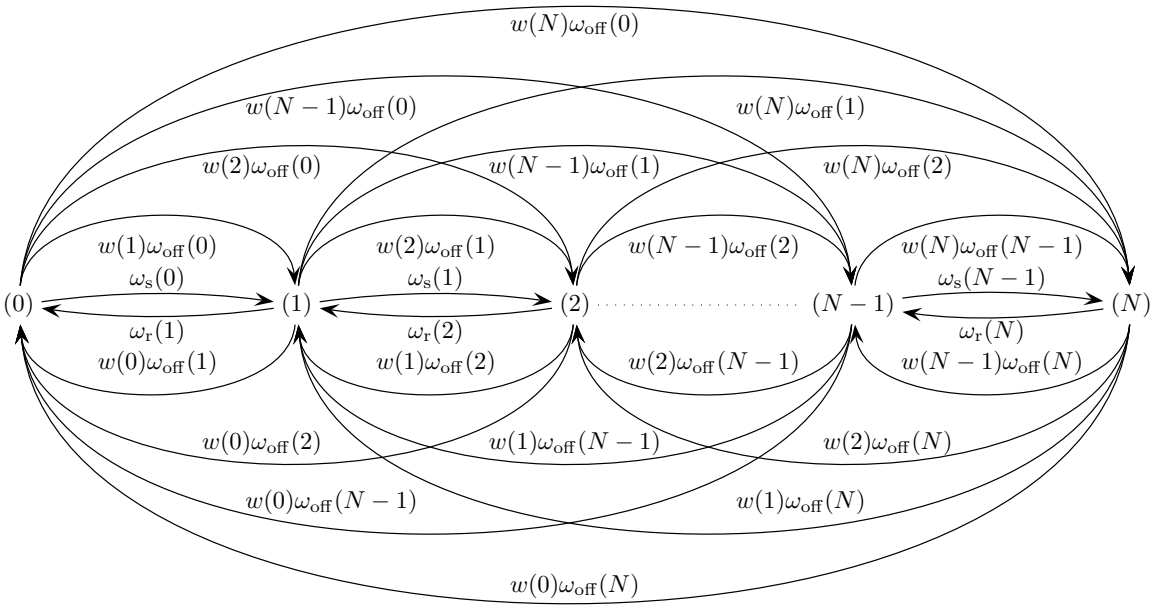

Figure 3.3 Closed network of network in fig. 3.2(b) obtained by redirecting all arrows that lead into the absorbing state (C_1) back into all starting states weighted with the initial probability distribution $w(i)$ as explained in section 2.3.3. We omitted the self loop of state (0), since it does not contribute to the calculations of the state probabilities.

to state (C_1), in which the cargo is transported by a single motor. These transitions are the sum of the force dependent unbinding rates of each motor,

$$\omega_{\text{off}}(i) \equiv \epsilon_1(F_i) + \epsilon_1(-F_i). \tag{3.8}$$

Since we are interested in the quantities t_2 and v_2, which are determined by the dynamics of both motors being active, we promote the state (C_1) to an absorbing state, see fig. 3.2(b). For a general description, we introduce the initial probability $w(i)$ to start in state (i), where $\sum_i w(i) = 1$. Now, t_2 is related to the probability current J into the absorbing state,

$$t_2^{-1} = J = \sum_{i=0}^{N} \omega_{\text{off}}(i) P_i, \tag{3.9}$$

as explained in section 2.3.3. Here, the P_i is the steady state probability distribution before absorption, which is obtained from the closed network taking account of the initial condition, as shown in fig. 3.3.

Since the unbinding rate $\omega_{\text{off}}(i)$ increases exponentially with i, the probability P_i decreases with i. For this reason, it is sufficient to study a finite chain. We chose N large enough and always check that the results do not depend on N, meaning that they converged. For such a finite system, P_i can be calculated from the steady state master equation,

$$0 = \partial_t P_0 = \omega_\mathrm{r}(1)P_1 - \omega_\mathrm{s}(0)P_0 - \sum_{j=1}^{N} w(j)\omega_\mathrm{off}(0)P_0 + \sum_{j=1}^{N} w(0)\omega_\mathrm{off}(j)P_j \tag{3.10}$$

$$0 = \partial_t P_i = \omega_\mathrm{s}(i-1)P_{i-1} + \omega_\mathrm{r}(i+1)P_{i+1} - \omega_\mathrm{r}(i)P_i - \omega_\mathrm{s}(i)P_i - \sum_{j\neq i}^{N} w(j)\omega_\mathrm{off}(i)P_i + \sum_{j\neq i}^{N} w(i)\omega_\mathrm{off}(j)P_j \tag{3.11}$$

$$0 = \partial_t P_N = \omega_\mathrm{s}(N-1)P_{N-1} - \omega_\mathrm{r}(N)P_N - \sum_{j=0}^{N-1} w(j)\omega_\mathrm{off}(N)P_N + \sum_{j=0}^{N-1} w(N)\omega_\mathrm{off}(j)P_j. \tag{3.12}$$

In general, this set of linear equations is difficult to solve in a closed form. However, for a specific model, the numerical values for the rates are known and the solution can be obtained with numerical methods [135–137].

Next, we derive the average velocity v_2 of two active motors. The stepping rate of the motors depend on the force. It is straightforward to define the velocity of the cargo as the average forward stepping rate $\langle\omega_\mathrm{f}\rangle$ minus the average backward stepping rate $\langle\omega_\mathrm{b}\rangle$ times the displacement of the cargo $l/2$ per motor step l,

$$v_2 \equiv (\langle\omega_\mathrm{f}\rangle - \langle\omega_\mathrm{b}\rangle)\frac{l}{2}. \tag{3.13}$$

Because both motors are identical and the two linkers are connected in series, one motor step of size l leads to a displacement of the cargo of $l/2$. The quantities $\langle\omega_\mathrm{f}\rangle$ and $\langle\omega_\mathrm{b}\rangle$ are related to transitions associated with forward and backward steps before absorption, respectively. The rate of a transition from state (i) associated with a forward step reads

$$\omega_\mathrm{f}(i) \equiv \begin{cases} 2\alpha(F_0) & i = 0 \\ \alpha(F_i) + \alpha(-F_i) & 0 < i < N \\ \alpha(-F_N) & i = N. \end{cases} \tag{3.14}$$

Likewise, we obtain the rate of backward steps from state (i) as

$$\omega_\mathrm{b}(i) \equiv \begin{cases} 2\beta(F_0) & i = 0 \\ \beta(F_i) + \beta(-F_i) & 0 < i < N \\ \beta(-F_N) & i = N. \end{cases} \tag{3.15}$$

Following the methods introduced in [128], the averaged rate of forward steps before absorption is

$$\langle\omega_\mathrm{f}\rangle \equiv \sum_i \omega_\mathrm{f}(i)P_i, \tag{3.16}$$

rates	$\omega_\mathrm{s}(0) = 2\mathcal{V}(0)/l = 2v/l$ $\omega_\mathrm{s}(i) = \mathcal{V}(F_i)/l = \frac{v}{l}(1 - \frac{F_i}{F_\mathrm{s}})$ $\omega_\mathrm{r}(i) = \mathcal{V}(-F_i)/l = \frac{v}{l}$ $\omega_\mathrm{off}(i) = \epsilon_1(F_i) + \epsilon_1(-F_i) = 2\epsilon e^{F_i/F_\mathrm{d}}$
parameters	$F_i = \kappa l i/2$ $N = \lceil \frac{2F_\mathrm{s}}{\kappa l} \rceil$ $l \simeq 8\,\mathrm{nm}$ $v \simeq 1\,\mu\mathrm{m/s}$ $\epsilon \simeq 1\,\mathrm{s}^{-1}$ $\kappa \simeq 0.3\,\mathrm{pN/nm}$ $F_\mathrm{s} \simeq 6\,\mathrm{pN}$ $F_\mathrm{d} \simeq 3\,\mathrm{pN}$

Table 3.1 Complete set of rates and parameters for the network shown in fig. 3.4 based on the reduced description of a molecular motor as explained in the text. The numerical values are taken from table 2.1 and have been measured for kinesin-1.

where P_i is again the steady state probability distribution before absorption, obtained from the closed network of fig. 3.3. Likewise, we obtain for the backward steps,

$$\langle \omega_\mathrm{b} \rangle \equiv \sum_i \omega_\mathrm{b}(i) P_i. \tag{3.17}$$

Using the definition of the force-velocity relation of a single motor eq. (2.3), the average velocity of two active motors eq. (3.13) can alternatively be rewritten as

$$v_2 = \frac{1}{2} \sum_i (\mathcal{V}(F_i) + \mathcal{V}(-F_i)) P_i. \tag{3.18}$$

In this section, we established a rather general description of two elastically coupled identical motors. So far, this description is based on general characteristics of single motors: force-dependent forward and backward stepping and force-dependent unbinding. We coupled the motors via an elastic force, which depends on the distance between the motors. In addition, we incorporated a general initial condition that takes into account how the motors start working together. In the following, we will specify all of these parameters and study their influence on cargo transport by two motors in more detail.

3.2.1. Reduced description of a single molecular motor

In the following, we specify a minimal model based on kinesin-1 data that captures the characteristic properties of processive molecular motors, as discussed in section 2.2.1. The advantage of such a minimal model is to understand the origin of certain effects without getting lost in details. Furthermore, without specifying details, it is applicable to different motor species with similar behavior, at least in a qualitative manner.

The dynamics of a single motor has been introduced in section 2.2.1. Neglecting backward stepping[2] of the motor, the stepping rates attain the simple form,

$$\alpha(F) = \frac{\mathcal{V}(F)}{l} \quad \text{and} \tag{3.19}$$

$$\beta(F) = 0. \tag{3.20}$$

Using these rates with the piecewise-linear force-velocity relation $\mathcal{V}(F)$, eq. (2.20), we obtain, from eq. (3.5) - eq. (3.7), the rates for stretching,

$$\omega_{\mathrm{s}}(0) = 2\alpha(0) = 2\frac{\mathcal{V}(0)}{l} = 2\frac{v}{l}, \tag{3.21}$$

and for $i \neq 0$,

$$\omega_{\mathrm{s}}(i) = \alpha(F_i) = \frac{\mathcal{V}(F_i)}{l} = \frac{v}{l}\left(1 - \frac{F_i}{F_{\mathrm{s}}}\right), \tag{3.22}$$

and for relaxation,

$$\omega_{\mathrm{r}}(i) = \alpha(-F_i) = \frac{\mathcal{V}(-F_i)}{l} = \frac{v}{l}. \tag{3.23}$$

We assume that the force-dependent unbinding does not depend on the direction of the force and use the unbinding rate $\epsilon_1(F)$ from eq. (2.14), leading to the effective unbinding rate from eq. (3.8),

$$\omega_{\mathrm{off}}(i) = 2\epsilon e^{F_i/F_{\mathrm{d}}}. \tag{3.24}$$

As a first approximation, we describe the elastic motor linker as a linear spring with spring constant κ as introduced in section 2.2.1. A cargo transported by two active motors moves the distance $l/2$ if one of the motors takes a step of length l. Therefore, the elastic force

$$F_i = \kappa\frac{il}{2} \equiv iF_\kappa \tag{3.25}$$

is generated per motor step in each elastic linker. Here, we introduce the elastic force per motor step

$$F_\kappa \equiv \frac{\kappa l}{2}. \tag{3.26}$$

The highest state N of the network corresponds to the largest force NF_κ that can occur. In our reduced description without back stepping the highest force is the stall force F_{s}. Thus, from $NF_\kappa = F_{\mathrm{s}}$ it follows that $N = \lceil F_{\mathrm{s}}/F_\kappa \rceil = \lceil 2F_{\mathrm{s}}/\kappa l \rceil$, where we use the ceiling function $\lceil\ \rceil$ to map the, in general, continuous variable F_{s}/F_κ to the discrete variable N correctly. Finally, we have to specify the initial conditions. We assume that, when one motor is active, the second motor initially binds to the filament in such a way that the linkers are relaxed. This is justified by estimating the energy that is needed to reach the next binding site

[2]Backward stepping can be included into the model and does not change the results substantially as discussed in appendix A.5

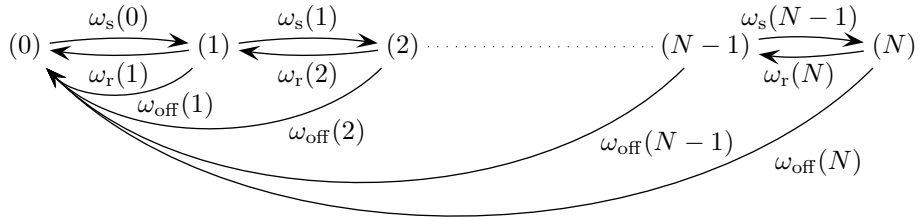

Figure 3.4 Closed network of network in fig. 3.3 with the special initial condition $w(0) = 1$ and $w(i) = 0$ for $i \neq 0$.

rates	$\omega_\mathrm{s}(0) = 2\mathcal{V}(0)/l = 2\frac{v}{l}$ $\omega_\mathrm{s}(i, f_\mathrm{s}) = \mathcal{V}(i, f_\mathrm{s})/l = \frac{v}{l}(1 - \frac{i}{f_\mathrm{s}})$ $\omega_\mathrm{r}(i) = \mathcal{V}(-i, f_\mathrm{s})/l = \frac{v}{l}$ $\omega_\mathrm{off}(i, f_\mathrm{d}) = \epsilon_1(i, f_\mathrm{d}) + \epsilon_1(-i, f_\mathrm{d}) = 2\epsilon e^{i/f_\mathrm{d}}$
parameters	$N(f_\mathrm{s}) = \lceil f_\mathrm{s} \rceil$ $v/l \simeq 125\,\mathrm{s}^{-1}$ $\epsilon \simeq 1\,\mathrm{s}^{-1}$

Table 3.2 Rates and parameters for the network shown in fig. 3.4 with the scaled forces $f_\mathrm{s} = 2F_\mathrm{s}/\kappa l$ and $f_\mathrm{d} = 2F_\mathrm{d}/\kappa l$ as variables. The only two numerical values, the single motor stepping rate v/l and the single motor unbinding rate ϵ are taken from table 2.1 for kinesin-1.

purely by diffusion. The elasticity of both motor linkers in series has an effective spring constant of $\kappa/2$. Using the equipartition theorem, we obtain the energy $\kappa \left\langle (\Delta l)^2 \right\rangle /2$ for such a thermally driven spring. With a distance to the next binding site of $\Delta l = 8\,\mathrm{nm}$ and a reasonable spring constant $\kappa \simeq 0.3\,\mathrm{pN/nm}$ from table 2.1, the needed energy is $9.6\,\mathrm{pN\,nm}$, which is more than twice of the thermal energy at room temperature, $k_\mathrm{B}T \simeq 4.1\,\mathrm{pN\,nm}$. Hence, it is most likely that the motors always start pulling the cargo in the relaxed state (0). Therefore, we let all runs start in state (0) with probability $w(0) = 1$ and $w(i) = 0$ for $i \neq 0$. However, our results are surprisingly robust to more general initial conditions, which will be discussed and explained in appendix A.8. For the initial condition $w(0) = 1$, the network of fig. 3.3 simplifies to the network shown in fig. 3.4 with rates summarized in table 3.1. The steady state master equation for this network can be solved iteratively, since the equation (3.12) for P_N, only depends on P_{N-1}, see appendix A.2.

3.3. Different transport regimes and the associated force scales

The average binding time t_2 and the average velocity v_2 characterize the activity state (C_2), as shown in fig. 3.1, in which both motors are active. Both quantities are determined from stepping and unbinding of the motors. Due to the stochastic stepping of the coupled motors, the distance between them fluctuates and induces an elastic force. In turn, this force dictates

the stepping of the motors via the force-velocity relation. In addition, stepping is terminated by the force-dependent unbinding. Thus, stepping and unbinding are coupled by the elastic force generation and lead to a strong interdependence. In other words: both quantities depend on the single motor dynamics and on the strength of their elastic coupling. In this way, strongly coupled and/or fast motors can quickly build up a large elastic strain force that pulls one of the motors from the filament, while weakly coupled and/or slow motors may unbind spontaneously prior to reaching such a large force, see fig. 3.5. These processes are related to three force scales: (i) the detachment force F_d, which is the force scale for single motor unbinding from eq. (2.14), (ii) the stall force F_s which is the force scale for single motor steps from eq. (2.7), and (iii) the strain force F_κ, which is the force scale for the elastic coupling as in eq. (3.26). Since unbinding and stepping are governed by the strain force, we introduce the scaled detachment force

$$f_\mathrm{d} \equiv \frac{F_\mathrm{d}}{F_\kappa} \tag{3.27}$$

and the scaled stall force

$$f_\mathrm{s} \equiv \frac{F_\mathrm{s}}{F_\kappa}. \tag{3.28}$$

Together with these scaled forces, we rewrite the force-dependent part of the force-velocity relation, eq. (2.20),

$$\mathcal{V}(i) = v\left(1 - \frac{iF_\kappa}{F_\mathrm{s}}\right) = v\left(1 - \frac{i}{f_\mathrm{s}}\right), \tag{3.29}$$

and the unbinding rate, eq. (2.14)

$$\epsilon_1(i) = \epsilon e^{\frac{i\kappa l}{2F_\mathrm{d}}} = \epsilon e^{\frac{i}{f_\mathrm{d}}}. \tag{3.30}$$

The influence of the elastic force onto stepping and/or unbinding now depends on the scaled forces f_s and f_d, respectively. In order to compare the motor pair quantities t_2 and v_2 to single motor parameters, we introduce the scaled binding time

$$\tilde{t}_2 \equiv \frac{t_2}{t_1} \tag{3.31}$$

and the scaled velocity

$$\tilde{v}_2 \equiv \frac{v_2}{v}. \tag{3.32}$$

For independent motors without interference, we have $\tilde{t}_2 = 1/2$ and $\tilde{v}_2 = 1$. To obtain $\tilde{t}_2$ and $\tilde{v}_2$ as a function of the scaled forces f_s and f_d, the only free parameters that we have to specify are the force-free stepping rate v/l and the single motor binding time $t_1 = 1/\epsilon$. We take the standard values for kinesin-1 from table 2.1 for these parameters, $v/l \simeq 125\,\mathrm{s}^{-1}$ and $\epsilon \simeq 1\,\mathrm{s}^{-1}$. In this way, we have now specified all rates of the network shown in fig. 3.4, with rates summarized in table 3.2. Now, we solve the master equation for this network using a recursion explained in appendix A.2. With the probability distribution P_i, we plot

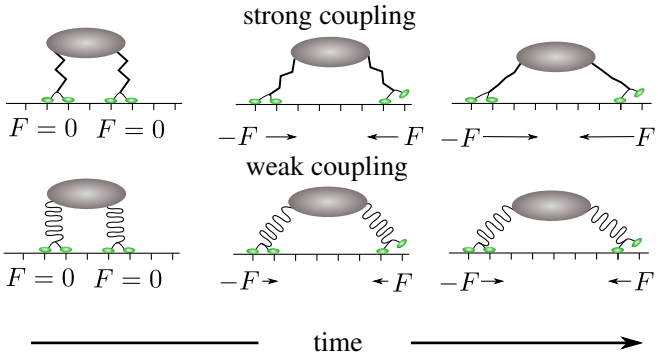

Figure 3.5 Two molecular motors coupled via elastic linkers to their cargo. The motors step forward stochastically and stretch their linkers, thereby inducing an elastic interaction that generates the strain force F. Strong elastic coupling leads to a fast build-up of large forces whereas weakly coupled motors experience only relatively small forces.

the scaled binding time from eq. (3.31) with eq. (3.9) and the scaled velocity from eq. (3.32) with eq. (3.18) as a function of the scaled forces f_s and f_d, see fig. 3.6. In both plots we restrict $f_\mathrm{s} \geq 1$ and $f_\mathrm{d} \geq 1$. This is reasonable, since for $f_\mathrm{s} < 1$ and $f_\mathrm{d} < 1$ the induced strain force would exceed the stall force or the detachment force already for an extension that corresponds to one motor step. The four corners of fig. 3.6 correspond to different transport regimes. In the upper right corner, both the velocity and the binding time are hardly affected by the coupling. This region corresponds to a weak coupling regime (I). In contrast, both quantities are strongly reduced in a strong coupling regime (II) located at the lower left corner. Furthermore, in the upper left corner, we find a reduced velocity regime (III) that is characterized by a reduced value of $\tilde{v}_2$ but an essentially unchanged binding time $\tilde{t}_2$. In contrast, the lower right corner exhibits a reduced binding time but an essentially unchanged velocity. We call this transport regime the enhanced unbinding regime (IV). Thus, in addition to the weak and the strong coupling regimes, which one may expect naively, we identify the two regimes (III) and (IV).

The four different transport regimes can be understood, in a qualitative manner, from the competition of the three different force scales. In the weak coupling regime (I), $F_\kappa \ll F_\mathrm{d}$ and $F_\kappa \ll F_\mathrm{s}$. When F_κ is comparable to both F_d and F_s, the coupling affects the unbinding and the stepping which is the case in the strong coupling regime (II). In the reduced velocity regime (III), $F_\kappa \simeq F_\mathrm{s} \ll F_\mathrm{d}$ and thus unbinding is not affected. For $F_\kappa \simeq F_\mathrm{d} \ll F_\mathrm{s}$, unbinding is enhanced without a reduced velocity, which characterized the enhanced unbinding regime (IV). Which of the processes of either stepping or unbinding are predominantly induced by the strain forces, depends on the relative magnitude of the detachment and stall forces. Force-induced unbinding dominates for $F_\mathrm{d} \ll F_\mathrm{s}$, whereas the reduction of the motor velocity occurs for $F_\mathrm{s} \ll F_\mathrm{d}$. In previous studies, the ratio $f \equiv \frac{F_\mathrm{s}}{F_\mathrm{d}}$ has been introduced to characterize the dynamics of cargo transport by two antagonistic motor teams resulting in a tug of war [51, 109]. Qualitatively, it is the ratio of the force a

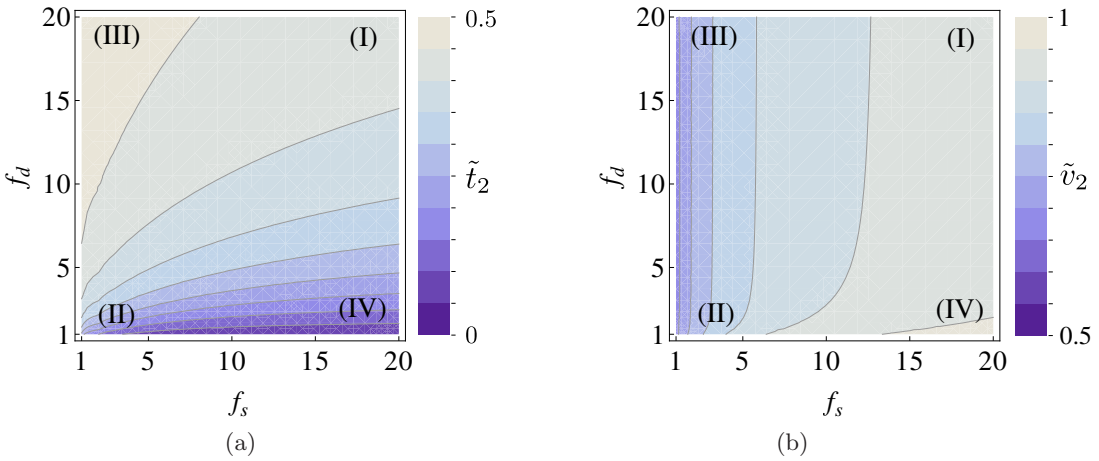

Figure 3.6 (a) Average scaled binding time $\tilde{t}_2$ and (b) velocity $\tilde{v}_2$ of a cargo pulled by two active motors with rates and parameters from table 3.2. The scales are the single motor binding time t_1 and single motor velocity v, respectively. Both quantities are displayed in a colored contour plot as a function of the rescaled single motor stall force $f_\mathrm{s} \equiv F_\mathrm{s}/F_\kappa$ and the rescaled detachment force $f_\mathrm{d} \equiv F_\mathrm{d}/F_\kappa$, where the force scale $F_\kappa \equiv \kappa l/2$ is the elastic strain force between the motors per motor step. Four distinct transport regimes can be identified: (I) *weak coupling* with essentially unchanged velocity and binding time; (II) *strong coupling* with both reduced binding time and reduced velocity; (III) *reduced velocity* with no effect on the binding time and (IV) *enhanced unbinding* with no effect on the velocity.

motor can produce and the force a motor can sustain for an extended period of time. In this way, motors with large f are 'strong', and those with small f are 'weak'. Interestingly, only strong motors with $f > 1$ can access the enhanced unbinding region (IV), whereas the reduced velocity region (III) is only accessible for weak motors with $f < 1$.

However, how quickly the strain force is generated between the motors, depends both on F_κ and on the stepping dynamics. For example, in the extreme case that the motors do not move at all, no strain force is generated between them and hence, there is no interference. So far, we have identified the different regimes of transport. For a more precise description of the boundaries between these transport regimes, we need to take the dynamics and thus different time scales into account.

3.3.1. Different timescale for strain force generation

In this section, we compare different time scales in order to estimate which of the processes of spontaneous unbinding, force-induced unbinding or reduced stepping of the motors occurs first. In this way, we obtain the crossover lines between the four transport regimes. These time scales provide a framework to qualitatively predict and explain the behavior of two coupled motors based on the description of a single motor. Therefore, we can use these

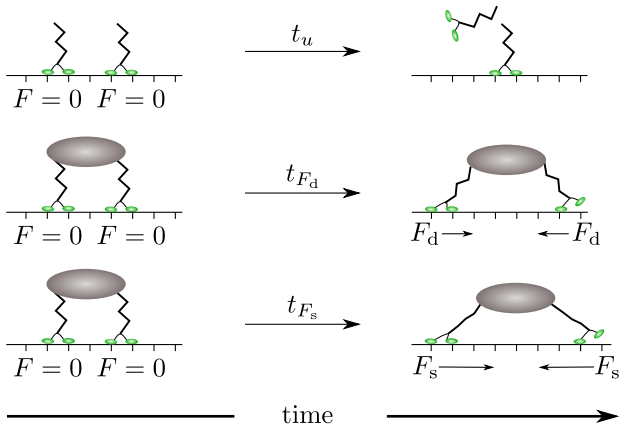

Figure 3.7 Illustration of different time scales. It takes the time t_u for one of two non-interacting motors to unbind. The time t_{F_d} is required to build up strain forces between two motors comparable to the detachment force F_d. It takes the time t_{F_s} to generate strain forces that are in the order of the stall force F_s.

arguments to discuss refinements and extensions of our description, as we present in section 3.4. Furthermore, it provides a way to understand why previous studies arrived at different conclusions about cooperative motor transport.

The dynamics of motors that collectively pull the cargo is governed by the interplay of two processes: the unbinding of the motors and the generation of elastic forces via stepping. We now consider these processes separately, and identify the characteristic time scales associated with them. Similar considerations have been used to study the dynamics and force generation during the rupture of biomolecular bonds [138,139]. We compare three different time scales as illustrated in fig. 3.7: (i) The time t_u for spontaneous unbinding of one of the two motors, (ii) the time t_{F_d} required to build up elastic strain forces that are greater than or equal to the *detachment* force, and (iii) the time t_{F_s} required to build up strain forces greater than or equal to the *stall* force. The timescale t_u for spontaneous unbinding is estimated by ignoring interactions between the motors and therefore given by

$$t_\mathrm{u} \equiv \frac{1}{2\epsilon}. \tag{3.33}$$

To obtain the other two times t_{F_s} and t_{F_d}, we neglect unbinding, i.e. we set all rates $\omega_\mathrm{off}(i) = 0$ and consider two motors that start in the relaxed state (0). We estimate the time t_{F_d} from the time that passes until these motors first reach the target state with index $i_\mathrm{t} = \lceil F_\mathrm{d}/F_\kappa \rceil = \lceil f_\mathrm{d} \rceil$, in which the strain force is greater than or equal to the detachment force. In the same way, we derive the time t_{F_s} with the corresponding target state index $i_\mathrm{t} = \lceil f_\mathrm{s} \rceil$. To calculate this mean first passage time, we use a network with a reflecting and

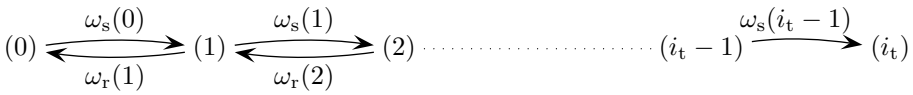

Figure 3.8 Network to calculate the average time that it takes for a run to start in state (0) and end in state (i_t). This network is a modification of the network in fig. 3.4. The state (i_t) is promoted to an absorbing state and unbinding is omitted.

an absorbing boundary shown in fig. 3.8 and, in this way, obtain the time

$$t_{i_t} = \sum_{i=0}^{i_t-1} \sum_{j=0}^{i} \frac{\omega_r(i)\omega_r(i-1)\dots\omega_r(j+1)}{\omega_s(i)\omega_s(i-1)\dots\omega_s(j+1)\omega_s(j)}, \tag{3.34}$$

as explained in section 2.3.2 and in [86].

Using the definition of the rates form eq. (3.21) - eq. (3.23) and the force-velocity relation eq. (3.29), we obtain the time scale associated with the detachment force,

$$t_{F_d} = \sum_{i=0}^{\lceil f_d \rceil - 1} \left(\frac{\prod_{k=1}^{i} \alpha(-kF_\kappa)}{2\prod_{k=0}^{i} \alpha(kF_\kappa)} + \sum_{j=1}^{i} \frac{\prod_{k=1+j}^{i} \alpha(-kF_\kappa)}{\prod_{k=j}^{i} \alpha(kF_\kappa)} \right) \tag{3.35}$$

$$= \frac{l}{v} \sum_{i=0}^{\lceil f_d \rceil - 1} \left(\frac{1}{2\prod_{k=0}^{i}(1-\frac{k}{f_s})} + \sum_{j=1}^{i} \frac{1}{\prod_{k=j}^{i}(1-\frac{k}{f_s})} \right). \tag{3.36}$$

Note that this sum diverges for $f_d > f_s$, since the forces between the motors are bounded by the stall force F_s. Hence, they never reach the detachment force if $F_d > F_s$.

The comparison of the two time scales t_u and t_{F_d} leads to two distinct unbinding regimes: (i) A regime of *spontaneous unbinding* for $t_{F_d} > t_u$, in which motors spontaneously unbind before they build up sufficiently large strain forces; and (ii), a regime of *strain-induced unbinding* for $t_{F_d} < t_u$. In this regime, the time to generate forces comparable to the detachment force is shorter than the time for spontaneous unbinding. The transport regimes of weak coupling (I) and reduced velocity (III) belong to the category of spontaneous unbinding, whereas unbinding in the transport regimes of strong coupling (II) and enhanced unbinding (III) is strain-induced. In this way, the crossover line between the regimes is defined by $t_{F_d} = t_u$, leading to

$$\frac{l}{v} \sum_{i=0}^{\lceil f_d \rceil - 1} \left(\frac{1}{2\prod_{k=0}^{i}(1-\frac{k}{f_s})} + \sum_{j=1}^{i} \frac{1}{\prod_{k=j}^{i}(1-\frac{k}{f_s})} \right) = \frac{1}{2\epsilon}. \tag{3.37}$$

This equation implicitly defines the crossover line $f_d(f_s)$. The numerical solution [137] of the crossover line exhibits steps arising from the ceiling function in eq. (3.37) that is discussed in more detail in appendix A.3. In order to describe this crossover line qualitatively, we approximate it with a Michaelis-Menten like behavior

$$f_d(f_s) = \frac{f_d^* f_s}{f_d^* + f_s - 1} \tag{3.38}$$

that satisfies the constraint $f_\mathrm{d}(1) = 1$. The saturation value f_d^* is obtained by taking the limit $f_\mathrm{s} \to \infty$ of eq. (3.37), leading to

$$\frac{l\lceil f_\mathrm{d}\rceil^2}{2v} = \frac{1}{2\epsilon}. \tag{3.39}$$

The left hand side of this equation is discrete, while the right hand side is continuous. Therefore, we determine the smallest value f_d^* for which $t_{F_\mathrm{d}} \geq t_\mathrm{u}$, leading to

$$f_\mathrm{d}^* = \left\lceil \sqrt{\frac{v}{l\epsilon}} \right\rceil. \tag{3.40}$$

Here, we see that f_d^* increases for increasing $v/l\epsilon$. This approximation is displayed in fig. 3.9 as the broken black line.

The time t_{F_s}, required to generate forces comparable to the stall force is obtained from eq. (3.35) with the target state index $i_\mathrm{t} = (\lceil f_\mathrm{s}\rceil)$,

$$t_{F_\mathrm{s}} = \frac{l}{v}\sum_{i=0}^{\lceil f_\mathrm{s}\rceil-1}\left(\frac{1}{2\prod_{k=0}^{i}(1-\frac{k}{f_\mathrm{s}})} + \sum_{j=1}^{i}\frac{1}{\prod_{k=j}^{i}(1-\frac{k}{f_\mathrm{s}})}\right). \tag{3.41}$$

Whether the velocity is reduced before one of the motors unbinds can be concluded from the comparison of the time t_{F_s} and the unbinding time t_u,

$$\frac{l}{v}\sum_{i=0}^{\lceil f_\mathrm{s}\rceil-1}\left(\frac{1}{2\prod_{k=0}^{i}(1-\frac{k}{f_\mathrm{s}})} + \sum_{j=1}^{i}\frac{1}{\prod_{k=j}^{i}(1-\frac{k}{f_\mathrm{s}})}\right) \simeq \frac{1}{2\epsilon}. \tag{3.42}$$

This equation is independent of the scaled detachment force f_d. However, solving the equation for f_s in a unique way is not straightforward, because f_s appears in the ceiling function and in the denominator, see also discussion in appendix A.3. To circumvent these issues, we define the crossover line as the smallest integer f_s^* for which $t_{F_\mathrm{s}} \geq t_\mathrm{u}$ holds; it is displayed as a blue line in fig. 3.9. This crossover line distinguishes whether there is a reduction in the velocity or not. In this way, it divides the strong coupling regime (II) and the reduced stepping regime (III) from the weak coupling regime (I) and the enhanced unbinding regime (IV). To show that f_s^* increases with increasing $v/l\epsilon$, we rewrite t_{F_s} as

$$t_{F_\mathrm{s}} = \frac{l}{v}A(f_\mathrm{s}), \tag{3.43}$$

where

$$A(f_\mathrm{s}) \equiv \sum_{i=0}^{\lceil f_\mathrm{s}\rceil-1}\left(\frac{1}{2\prod_{k=0}^{i}(1-\frac{k}{f_\mathrm{s}})} + \sum_{j=1}^{i}\frac{1}{\prod_{k=j}^{i}(1-\frac{k}{f_\mathrm{s}})}\right). \tag{3.44}$$

From the numerical evaluation of this sum, we find that $A(f_\mathrm{s})$ can be approximated by $A(f_\mathrm{s}) \simeq 0.65\exp(f_\mathrm{s})$ for integer f_s, see appendix A.3. Therefore, the sum increases exponentially, i.e.,

$$A(f_\mathrm{s}) \sim e^{f_\mathrm{s}}. \tag{3.45}$$

Using the definition of the crossover line, we derive the scaling of this line as

$$f_{\mathrm{s}}^{*} \sim \left\lceil \ln \frac{v}{2l\epsilon} \right\rceil . \tag{3.46}$$

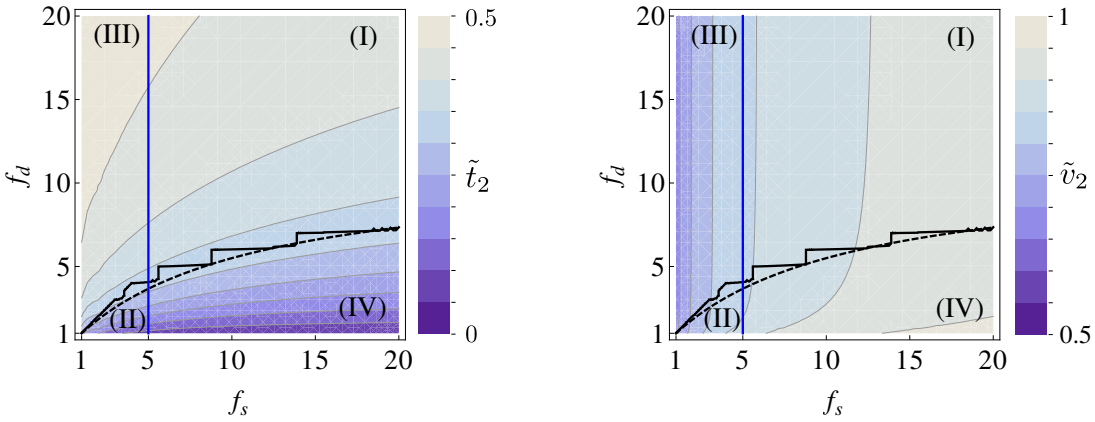

Figure 3.9 Distinct transport regimes of a cargo pulled by two active motors as a function of the rescaled stall force $f_{\mathrm{s}} = F_{\mathrm{s}}/F_{\kappa}$ and the rescaled detachment force $f_{\mathrm{d}} = F_{\mathrm{d}}/F_{\kappa}$. The crossover lines separating these regimes are obtained from the comparison of time scales, with the associated rates and parameters listed in table 3.2. Both contour plots are taken from fig. 3.6 and represent (a) the averaged scaled binding time $\tilde{t}_2$ and (b) the averaged scaled velocity $\tilde{v}_2$ with the four transport regimes: (I) weak coupling, (II) strong coupling, (III) reduced velocity and (IV) enhanced unbinding. The solid blue line separates the region with and without a reduced velocity, whereas the solid black line separates the region of spontaneous and force-induced unbinding. The dashed lines correspond to the approximated crossover line as given by eq. (3.38).

To summarize in terms of these time scales, the four transport regimes are now (I) *weak coupling* for $t_{\mathrm{u}} < t_{F_{\mathrm{d}}}$ and $t_{\mathrm{u}} < t_{F_{\mathrm{s}}}$; (II) *strong coupling* for $t_{\mathrm{u}} > t_{F_{\mathrm{d}}}$ and $t_{\mathrm{u}} > t_{F_{\mathrm{s}}}$; (III) *reduced velocity* for $t_{F_{\mathrm{s}}} < t_{\mathrm{u}} < t_{F_{\mathrm{d}}}$; and (IV) *enhanced unbinding* for $t_{F_{\mathrm{d}}} < t_{\mathrm{u}} < t_{F_{\mathrm{s}}}$. These crossover lines take the single motor parameters and especially the dynamics into account. Furthermore, the time scales allow us to estimate the change of parameters. The values f_{d}^{*} and f_{s}^{*} decrease with decreasing $v/l\epsilon$, see eq. (3.40) and eq. (3.46), which is the single motor run length in units of the motor step size. Therefore, for highly processive motors with a large run length, such as kinesin-8 [140], the crossover lines are shifted to higher values of f_{s} and f_{d} leading to a reduced *weak coupling* regime. If the motors are slowed down, e.g. by decreasing the ATP concentration, the crossover lines are shifted to smaller values leading to an increased *weak coupling* region, compare section 3.4.3 and appendix A.6.

The time scales $t_{F_{\mathrm{d}}}$ and $t_{F_{\mathrm{s}}}$ also provide an intuitive understanding of the effects arising from the elastic coupling. For stiffer linkers, it takes less time to build up high strain forces between the motors and thus the times $t_{F_{\mathrm{d}}}$ and $t_{F_{\mathrm{s}}}$ are rather small. In previous

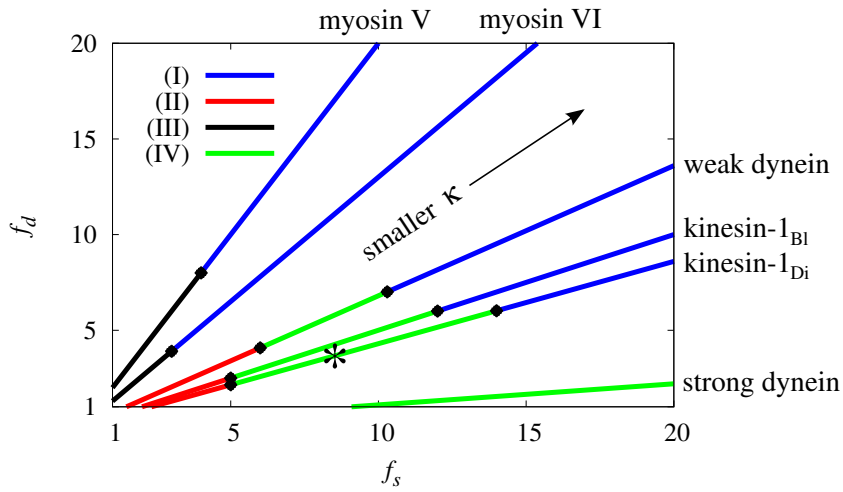

Figure 3.10 Transport regimes for pairs of different motors characterized by different dependencies between the rescaled detachment force $f_\mathrm{d} = F_\mathrm{d}/F_\kappa$ and the rescaled stall force $f_\mathrm{s} = F_\mathrm{s}/F_\kappa$ corresponding to different straight lines $f_\mathrm{d}(f_\mathrm{s}) = (F_\mathrm{d}/F_\mathrm{s})f_\mathrm{s}$. Each line represents a pair of two identical motors with fixed single motor parameters but variable elastic coupling strength κ which enters via $f_\mathrm{s} = F_\mathrm{s}/F_\kappa = 2F_\mathrm{s}/\kappa l$. We compare kinesin-$1_\mathrm{Bl}$ [94], kinesin-1_Di [25], weak dynein, strong dynein, myosin V, and myosin VI; the corresponding single motor parameters are listed in table 3.3. The different transport regimes (I) - (IV) are color coded and separated by crossover points (black diamonds); the precise locations of these points are given in table 3.4. The star indicates the pair of kinesin motors studied experimentally in [25].

models [43, 45], the motor linkers were described as cables to mimic a flexible polymer, see section 2.2.1. When both motors start working together in a compressed state, no force is built up until their linkers are stretched. This leads to an offset time, which is the time it takes until the motors start to interact via their linkers, and which contributes to the times t_{F_d} and t_{F_s}. Therefore, in models with cable-like linkers, one typically has $t_{F_\mathrm{d}} > t_\mathrm{u}$ and $t_{F_\mathrm{s}} > t_\mathrm{u}$ and thus relatively small interference effects [43, 45]. This will be discussed in more detail in section 3.4.5.

3.3.2. Transport regimes for pairs of different motor species

Next, we use the framework that we developed above to study the transport regimes for pairs of different motor species. In our reduced description, a specific motor is characterized by five parameters: the stall force F_s, the detachment force F_d, the force-free unbinding rate ϵ, the force-free velocity v and the step size l. These parameters have been measured or estimated for different motor species, see section 2.2.2. In the following, we use, for all motor species, the same shape of the force velocity relation and the same force-dependence of the unbinding rate. This first approximation can be refined as soon as more experimental data for different

motor species are available. We consider the coupling stiffness κ as the variable. In principle, the coupling stiffness can be changed by connecting the motors with different elastic elements or truncating their stalks [41]. In the Diehl lab, two kinesins have been coupled via a rigid DNA scaffold [25], but a connection with more flexible polypeptides should, in principle, be possible. For each motor species, varying the elastic coupling strength κ leads to the line $f_\mathrm{d}(f_\mathrm{s}) = (F_\mathrm{d}/F_\mathrm{s})f_\mathrm{s}$ in the $(f_\mathrm{s}, f_\mathrm{d})$-plane, see fig. 3.10. These lines intersect different transport regimes, which are indicated by different colors on each line. The crossover points between the transport regimes on a line are obtained as explained in the following. For each species of motor we calculate the two crossover lines of the transport regimes according to the time scales as presented in the previous section. These two crossover lines depend on the single motor stepping rate v/l and the force-free unbinding rate ϵ. Next, we determine the intersection of the crossover lines with the line $f_\mathrm{d}(f_\mathrm{s}) = (F_\mathrm{d}/F_\mathrm{s})f_\mathrm{s}$ that depend on the stall and detachment force. In this way, we obtain the transport regimes for different motor species on the corresponding line. For the different motor species, we use the parameters of table 3.3. The different sections on the lines are related to different ranges of coupling stiffness that we summarized in table 3.4. All of the motors access the weak coupling regime for a coupling stiffness that is sufficiently small. Pairs of kinesin-1 and weak dynein only operate in region (I), (II) or (IV). For kinesin-1, the different transport regimes have been discussed separately in the theoretical studies [30, 42–47, 134]. Myosin V and myosin VI, on the other hand, are only able to access region (I) or (III), provided that $F_\mathrm{d} > F_\mathrm{s}$, as indicated by a recent estimate [101].

	F_s [pN]	F_d [pN]	v [μm/s]	ϵ [s^{-1}]	l [nm]
kinesin-1_Bl	6 [94, 95]	3 [94]	1 [69, 94]	1 [94]	8 [69]
kinesin-1_Di	7 [26, 69]	3 [94]	0.5 [25]	0.61 [25]	8 [25]
strong dynein	7 [97]	0.75 [31]	0.65 [31]	0.27 [31]	8 [97]
weak dynein	1.1 [98]	0.75 [31]	0.65 [31]	0.27 [31]	8 [97]
myosin V	2 [101]	4 [101]	0.38 [101]	0.3 [101]	36 [101]
myosin VI	2 [101]	2.6 [101]	0.15 [101]	0.25 [101]	36 [101]

Table 3.3 Values of the single-motor parameters used to study the motor-motor interference of different pairs of elastically coupled motors. The values for kinesin-1_Bl were obtained in the Block lab with kinesin-1 extracted from squid. The values for kinesin-1_Di are obtained in the Diehl lab with human kinesin-1 and in the Cross lab with kinesin-1 from drosophila. For dynein two different stall forces were reported using dynein from different organisms. Therefore, we use two sets of parameters and label them with 'strong' dynein (from porcine brain) and 'weak' dynein (from bovine brain) according to the relative magnitude of their stall forces.

For a consistency check of our theory with the experimental data available, we determined the transport regimes for the kinesins that have been coupled in the Diehl experiment [25]. We denote this motor kinesin-1_Di in contrast to kinesin-1_Bl characterized by the parameters found in the Block lab [94]. In the Diehl experiment, two kinesin-1 motors have been

	(I) [pN/nm]	(II) [pN/nm]	(III) [pN/nm]	(IV) [pN/nm]
kinesin-1_{Bl}	$\kappa < 0.125$	$\kappa > 0.3$	-	$0.125 < \kappa < 0.3$
kinesin-1_{Di}	$\kappa < 0.125$	$\kappa > 0.35$	-	$0.125 < \kappa < 0.35$
strong dynein	$\kappa < 0.014$	-	-	$\kappa > 0.014$
weak dynein	$\kappa < 0.027$	$\kappa > 0.046$	-	$0.027 < \kappa < 0.046$
myosin V	$\kappa < 0.028$	-	$\kappa > 0.028$	-
myosin VI	$\kappa < 0.037$	-	$\kappa > 0.037$	-

Table 3.4 Ranges for the different transport regimes in terms of the coupling strength κ in pN/nm for different motor pairs with parameters from table 3.3. As discussed in the text, (I) is the weak coupling regime, (II) is the strong coupling regime, (III) is the reduced velocity regime and (IV) is the enhanced unbinding regime.

connected via a rigid DNA scaffold with an elastic coupling strength of $\kappa \simeq 0.2\,\mathrm{pN/nm}$ [25]. This system is represented by the star on the kinesin-1_{Di} line in fig. 3.10, which lies in the *enhanced unbinding* regime. Indeed, the motor pair studied in [25] was characterized by a strong reduction of the binding time, but essentially no effect on the cargo velocity as appropriate for this transport regime.

3.4. A motor pair with refined single motor properties

In the following, we apply the theoretical framework, developed in the previous section, to study the influence of refinements and extensions of our reduced motor description on the cooperative transport. In this way, we present several examples how our framework leads to additional insight into the dynamics of a motor pair. The extensions discussed in this subsection include different shapes of force-velocity relations, the dependence on ATP concentration and cable-like linkers.

3.4.1. Distribution of distances and forces between the two motors

First, we study the distributions of the distances and forces between two elastically coupled motors. We use the kinesin-1 rates and parameters given in table 3.1 and vary the stiffness κ of the coupling. Due to the stochastic stepping of the motors, the distance between the two motors fluctuates while they pull the cargo together. The distribution of the distances in units of the step size is given by the steady state probability distribution of the network shown in fig. 3.4. For decreasing κ, i.e., for weaker coupling, the tails of these distributions becomes longer, see fig. 3.11(a). They all exhibit a maximum at $i = 1$. The maximum is a consequence of the four pathways from state (0) to state (1) as discussed in section 3.2. The probability for distances of several steps between the motor decays. This decay results from the fact that large distances correspond to large forces, which in turn enhances unbinding and thus depopulates these states. For high strain forces, i.e. large values of κ, only a few steps between the motors are sufficient to induce unbinding, see fig. 3.11(a). Therefore,

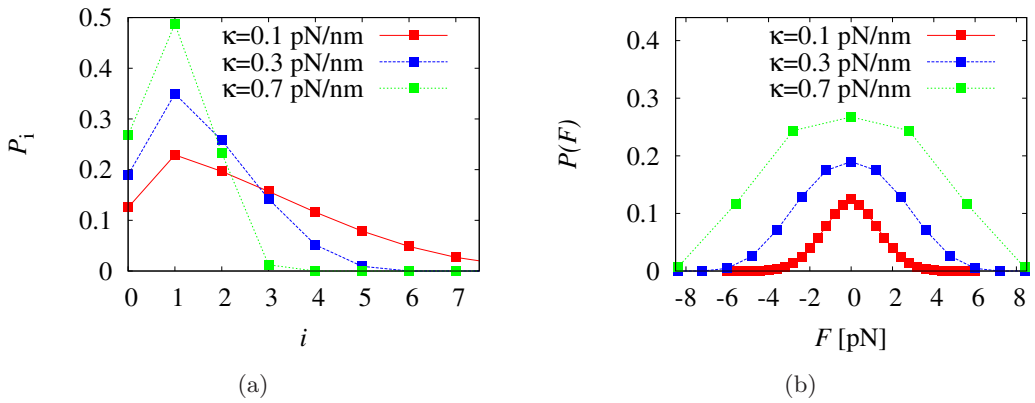

(a) (b)

Figure 3.11 (a) Distribution P_i of the effective distance in units of the step size corresponding to the index i of our description. (b) Distribution $P(F)$ of the forces acting on one motor for different values of the coupling stiffness κ. The rates and parameters are for kinesin-1, as listed in table 3.1.

strongly coupled motors have a narrow distribution.

According to the force extension relation, eq. (3.4), each distance between the motors corresponds to a certain strain force. Therefore, we map the distribution of the distances to a distribution of forces,

$$P(F_i) \equiv \begin{cases} P_i/2 & F_i < 0 \\ P_0 & F_i = 0 \\ P_i/2 & F_i > 0. \end{cases} \tag{3.47}$$

Because one motor feels F_i and the other $-F_i$, the probability distribution is symmetric with respect to $F_i = 0$. We plot the distribution of forces for different values of the coupling stiffness κ in fig. 3.11(b). For a reasonable coupling stiffness of $\kappa \simeq 0.3\,\mathrm{pN/nm}$, only forces smaller than stall force occur. Stronger coupling leads to broader probability distribution, see fig. 3.11(b). For a coupling constant of $\kappa = 0.7\,\mathrm{pN/nm}$, there is even a nonzero probability for a force larger than the stall force, see fig. 3.11(b). Such a large force is due to our reduced description, in which the force acting on the motor is determined by the present state and does not change during the transition to the next state. This means, the transition into a state with a force that exceeds the stall force is determined by its previous state, that is associated with a small force.

3.4.2. Influence of the shape of the force-velocity relation

Prior to discussing two generic types of force-velocity relations, we introduce a symmetry argument that we apply in our further study. The velocity of the cargo pulled by both motors is the average of the velocities of the single motors. One motor feels the force F_i and the other motor the opposing force $-F_i$. For a force-velocity relation that is point

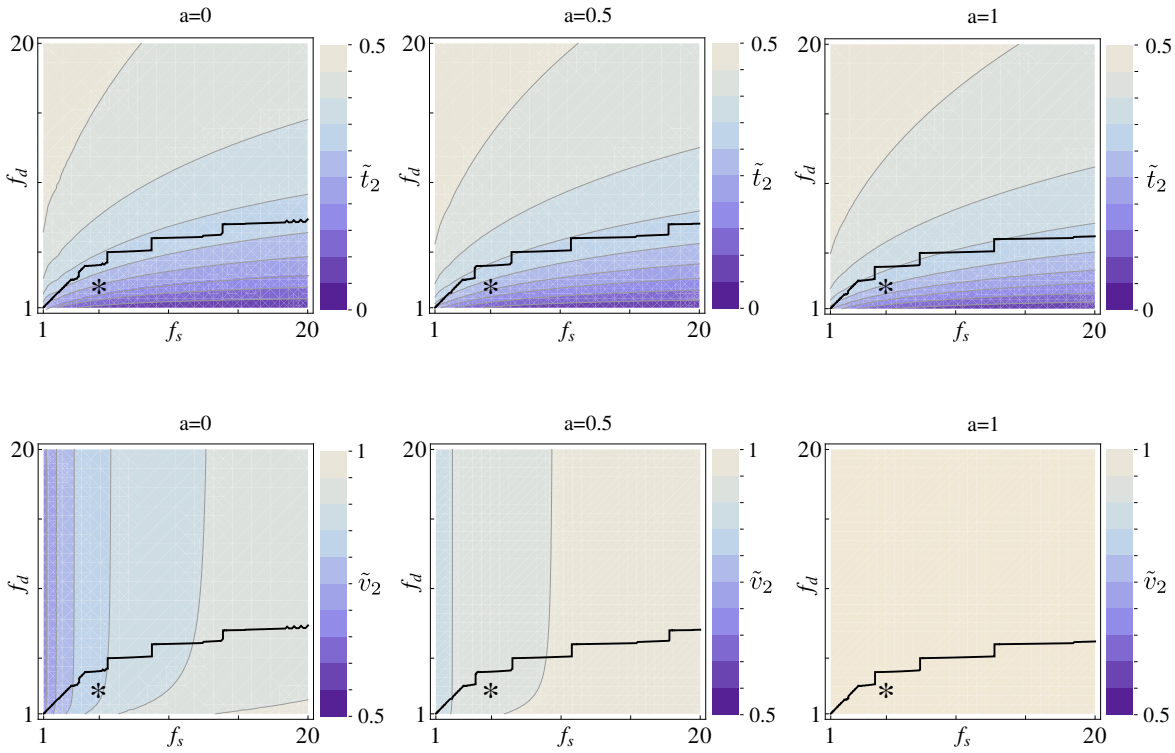

Figure 3.12 The scaled binding time $\tilde{t}_2$ (upper row) and velocity $\tilde{v}_2$ (lower row) of two active motors as a function of the scaled forces f_s and f_d, respectively. The shape of the force-velocity relation of the single motor is varied through the parameter a, as shown in fig. 3.13(a), with $a = 0$ for the left, $a = 0.5$ for the middle and $a = 1$ for the right column. The other parameters are summarized in table 3.2. The black line separates the regime of spontaneous unbinding (above the line) from the force-induced unbinding (below the line) determined from the time scale argument of section 3.3.1. For $a = 1$, the force-velocity relation is symmetric and $\tilde{v}_2$ is independent of the force and thus constant. The star represents the kinesin system with parameters from table 3.1 and is studied in detail in fig. 3.13.

symmetric with respect to $F = 0$, i.e.

$$\mathcal{V}(-F) + \mathcal{V}(F) = 2\mathcal{V}(0), \tag{3.48}$$

the average velocity of two active motors from eq. (3.18) does not depend on force,

$$v_2 = \mathcal{V}(0) \sum_i P_i = \mathcal{V}(0). \tag{3.49}$$

In this case, the average velocity of the cargo is never affected by forces between the motors, i.e. $v_\mathrm{ca} = v = v_2$. For this property, it is sufficient that the force-velocity relation

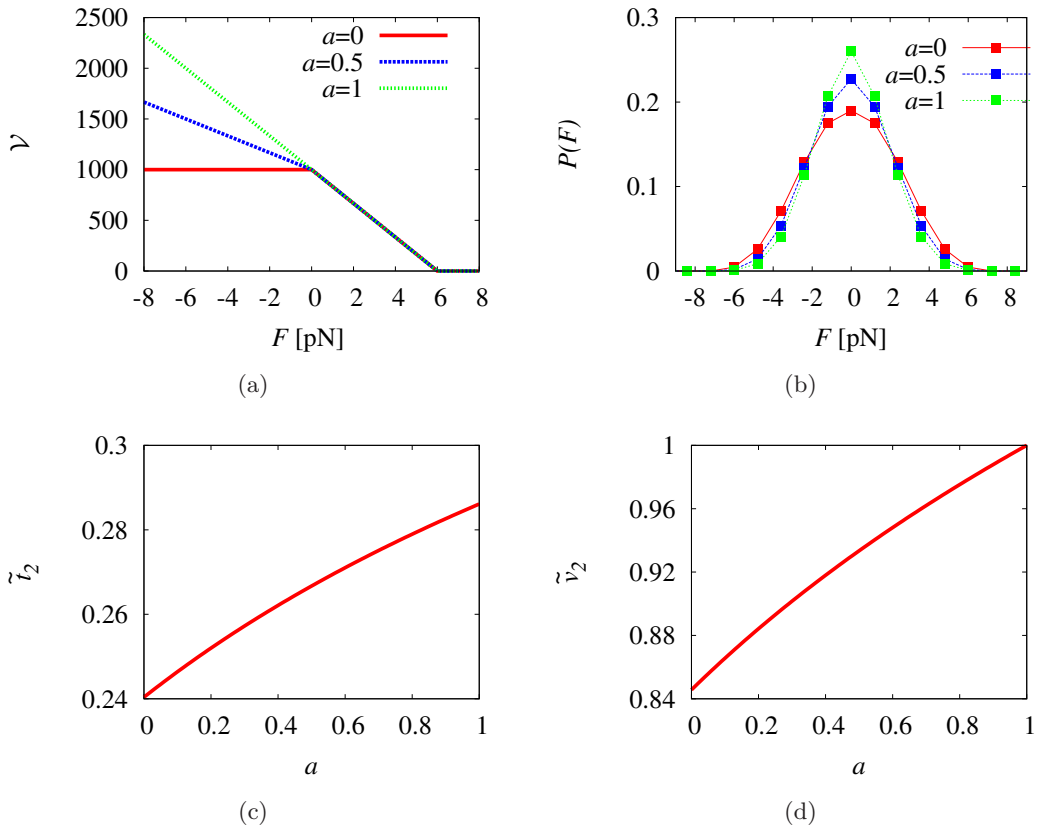

Figure 3.13 (a) Force-velocity relation $\mathcal{V}(F)$ as defined in eq. (3.50) for different parameters a. The force-velocity relation of (a) and the kinesin-1 parameters of table 3.1 are used to determine: (b) the distribution $P(F)$ of forces between the motors, (c) the scaled binding time $\tilde{t}_2$ and (d) the scaled velocity $\tilde{v}_2$ as a function of the force-velocity parameter a.

is symmetric over the range of forces, that are generated between the motors. This range of forces can be obtained from the width of the probability distribution of the forces as discussed in the previous subsection.

This symmetry argument indicates that the shape of the force-velocity relation influences the different transport regimes for a motor pair. In this way, for a symmetric force-velocity relation, the velocity v_2 is not reduced if the forces between the motors approach stall force. In this case, the stall force is not a suitable force scale to characterize the reduced stepping. Hence, the time scale t_{F_s} given by eq. (3.41) is not meaningful. Therefore, we only focus on the other time scale t_{F_d} for strain-induced unbinding, given by eq. (3.35). Note, both, the measured force-velocity relation, fig. 2.5(b), as well as the force-velocity relation used in our reduced description, fig. 2.6, are not symmetric and the time scale argument with respect to t_{F_s} is also applicable. In the following, we study the influence of the shape of the force-velocity relation in more detail using, as an example, two generic force-velocity relations.

The shapes of both force-velocity relations can lead to a force-independent velocity v_2, i.e., no interference effect on the velocity. However, in one case the interference effect on the binding time is pronounced, but not in the other.

First, we vary the force-dependence of the velocity for assisting forces, $F < 0$. In this range, experimental force-velocity curves from different studies exhibit the most pronounced differences [109]. We use piecewise linear force-velocity relations and vary the slope of the linear segment for $F < 0$ through the parameter a,

$$\mathcal{V}(F_i) \equiv \begin{cases} v(1 - aF_i/F_\mathrm{s}) & F_i < 0 \\ v(1 - F_i/F_\mathrm{s}) & 0 \leq F_i < F_\mathrm{s} \\ 0 & F_i \geq F_\mathrm{s} \end{cases} \tag{3.50}$$

see fig. 3.13(a). For $a = 0$, the velocity is constant for assisting forces $F < 0$, whereas for $a = 1$ the slopes of the force velocity relation for the region $F < 0$ and the region $0 < F < F_\mathrm{s}$ are identical.

Using the scaled forces f_s and f_d as variables with $\mathcal{V}(F)$ from eq. (3.50), we determine the scaled binding time $\tilde{t}_2$ and scaled velocity $\tilde{v}_2$ for different values of a, see fig. 3.12. In addition, we calculate the crossover lines between induced and spontaneous unbinding from the timescale argument $t_{F_\mathrm{d}} = t_\mathrm{u}$, see black line in fig. 3.12. As $a \to 1$, the force-velocity relation approaches a symmetric one and the region of induced unbind (below the black line) is slowly reduced. In the case of $a = 1$, the velocity is constant and independent of the strain force, see fig. 3.12.

Let us study the influence of the force-velocity parameter a onto the properties of a specific motor pair which is represented as a point marked with a star in fig. 3.12. We vary a between 0 and 1 and calculate the force distribution according to eq. (3.47), see fig. 3.13(b). The range of occurring forces is smaller than the stall force. For $a = 1$, the motors experience a linear force-velocity relation that is point symmetric with respect to $\mathcal{V}(0)$ over the range of occurring forces, leading to $v_2 = v$, i.e. $\tilde{v}_2 = 1$, see fig. 3.13(d).

Such a linear force-velocity relation with $a = 1$ reduces the strain between the motors, see fig. 3.13(c). The forward stepping rate $\mathcal{V}(-F)/l$ for the motor under $-F$ is higher than the forward stepping rate for the other motor under the force F. This motor pair tends to reduce the distance that separates the motors and thus the elastic strain force.

Decreasing the slope of the force-velocity relation for assisting forces leads to a smaller motor pair velocity $\tilde{v}_2$, since the motor under assisting force is slower, see fig. 3.13(d). Because of this slow motor, the tendency to step towards each other is also reduced. Hence, the binding time $\tilde{t}_2$ decreases with decreasing a, see fig. 3.13(c).

Next, we study force-velocity relations that exhibit a plateau around $F = 0$ motivated by force-velocity relations found in experiments [96]. To keep things simple, we use a piecewise linear force-velocity relation with a variable width of the plateau via the parameter b,

$$\mathcal{V}(F_i) \equiv \begin{cases} v & F_i < bF_\mathrm{s} \\ \frac{v}{F_\mathrm{s}(b-1)}(F_i - F_\mathrm{s}) & bF_\mathrm{s} \leq F_i < F_\mathrm{s} \\ 0 & F_i \geq F_\mathrm{s} \end{cases} \tag{3.51}$$

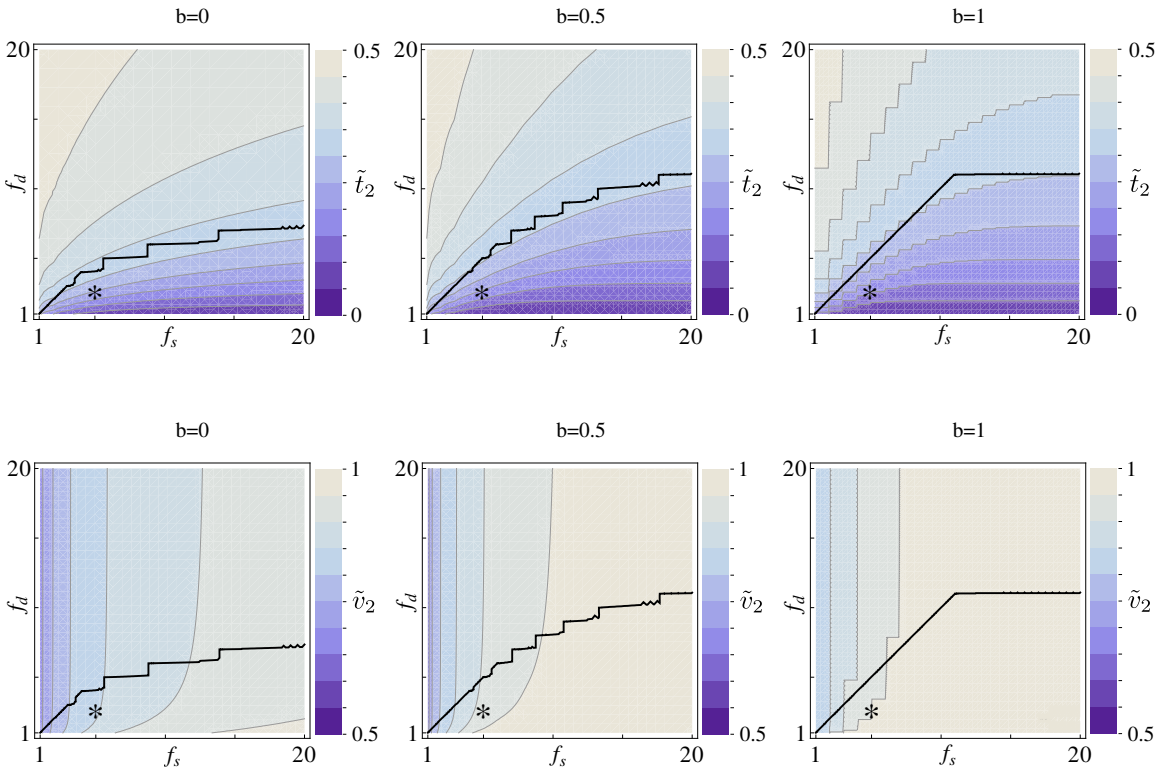

Figure 3.14 The scaled binding time $\tilde{t}_2$ (upper row) and velocity $\tilde{v}_2$ (lower row) of two active motors as a function of the scaled forces f_s and f_d. The shape of the single motor force velocity relation is varied through the parameter b as shown in fig. 3.15(a), with $b = 0$ for the left, $b = 0.5$ for the middle and $b = 1$ for the right column. The other parameters are summarized in table 3.2. The black line separates the regime of spontaneous unbinding (above the line) from the force-induced unbinding (below the line) determined from the time scale argument of section 3.3.1. For $b = 1$, the average velocity is almost not reduced, whereas unbinding is strongly enhanced. The star represents the kinesin system with parameters listed in table 3.1 and is studied in detail in fig. 3.15.

see fig. 3.15(a). For $b = 0$, the plateau is only in the region of the force-velocity relation for $F < 0$, whereas for $b = 1$, the force velocity relation is constant for all forces smaller than the stall force.

Using $\mathcal{V}(F)$ as defined by eq. (3.51), we determine $\tilde{t}_2$ and $\tilde{v}_2$ and the crossover line between induced and spontaneous unbinding from eq. (3.37) as a function of the scaled forces f_s and f_d, see fig. 3.14. For $b \to 1$, the induced unbinding region below the black line increases and the region with a reduced velocity shrinks, see fig. 3.14.

Next, we again focus on kinesin-1 represented as a star in fig. 3.14. As long as the forces between the motors are smaller than bF_s, the force-velocity relation is constant and the motors step independently of each other. Therefore, the forces between the motors

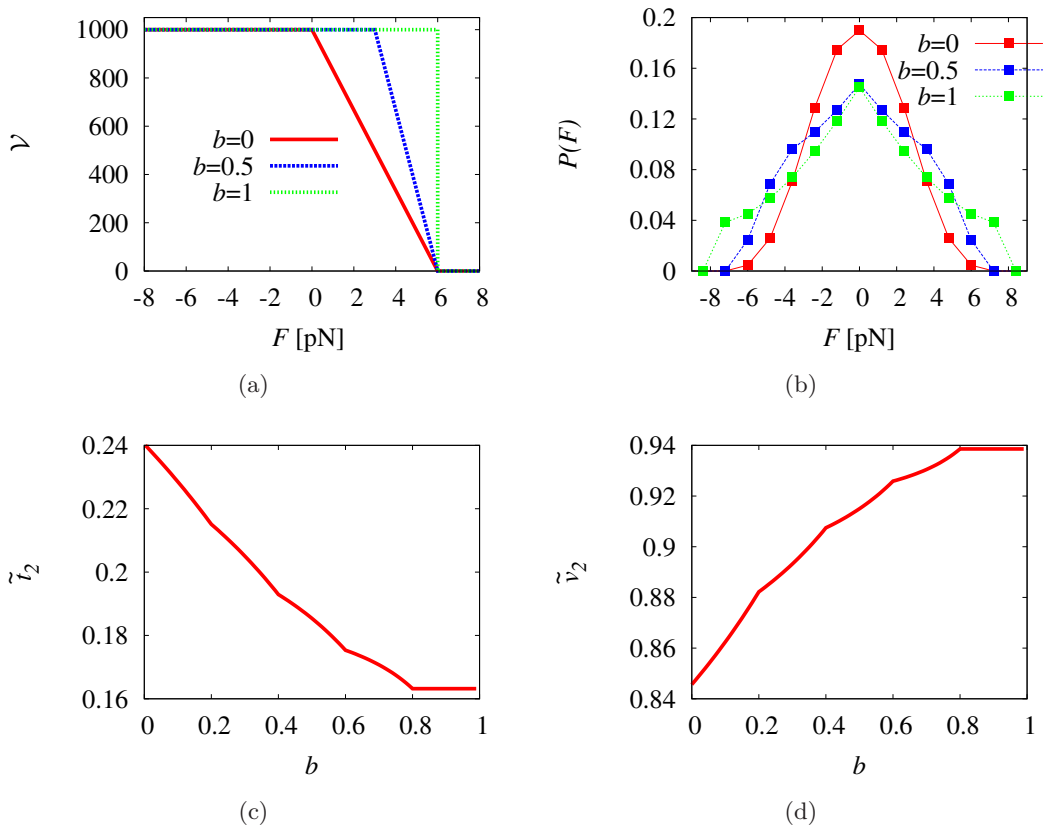

Figure 3.15 (a) Force-velocity relation $\mathcal{V}(F)$ as defined in eq. (3.51) for different parameters b. (b) Distribution of forces $P(F)$ between the motors for the force-velocity relations shown in (a) and parameters taken from table 3.1. For the same parameters, the scaled binding time $\tilde{t}_2$ and velocity $\tilde{v}_2$ as a function of the force velocity parameter b are shown in (c) and (d), respectively.

fluctuate strongly, which leads to a broad distribution of forces, see fig. 3.15(b). Note that even for $b = 1$ the distribution of forces has a considerably large contribution for forces around the stall force. For forces that are comparable to the stall force, it is reasonable to question the assumption of neglecting the occurrence of backward steps. We will address this issue in appendix A.5.

Inspection of the distribution of forces reveals the range of occurring forces between the motors, see fig. 3.15(b). The corresponding region of the force-velocity relation always includes the decreasing part. Therefore, the symmetry argument does not hold and we expect that $v_2 \neq v$, i.e. $\tilde{v}_2 \neq 1$. Indeed, even for $b = 1$, forces larger than stall force occur and thus the region of the force-velocity relation accessed by the motors is not point symmetric. In fig. 3.15(d), we find that $\tilde{v}_2 < 1$, which is a consequence of the concave shape of the force velocity relation. Following this line of argument, a convex force-velocity

relation leads to $\tilde{v}_2 > 1$ which indeed has been found in a previous theoretical study [44]. As the force-velocity relation becomes flatter, the steps of each of the two motors turn more independent. Hence, the induced elastic strain force fluctuates strongly, and the binding time decreases with increasing values of b, see fig. 3.15(c). Note, these considerations lead to a qualitative insight and are of theoretical rather than of experimental interest, since the force-velocity relation with $b = 1$ has the form of a step function, which seems rather unlikely for a real motor system.

Taken together, as both force-velocity relations approach a symmetric function, i.e. for $a \to 1$ and $b \to 1$, respectively, the interference effect on the velocity is reduced. However, as we explained above, the effect on the binding time is different: in one case unbinding is enhanced, but not in the other, see fig. 3.13(c) and fig. 3.15(c). In addition, the results for an empirical force velocity relation based on experimental data for kinesin-1 are presented in appendix A.5.

3.4.3. Magnitude of the single motor velocity: [ATP] dependence

In single molecule experiments with molecular motors, the ATP concentration has been varied over a large range of a few μM to a few mM [94]. High ATP concentrations increase the frequency of stepping, and we thus expect that the build-up of forces between the motors is faster, which in turn leads to a smaller time scale t_{F_d} to generate forces comparable to the detachment force. For this reason, not only v_2 depends on the ATP concentration, but also the binding time t_2. For a qualitative study, we use the [ATP] dependent force-velocity relation introduced in section 2.2.1. A further example for two different ATP concentrations, based on an empirical force-velocity relation for kinesin-1, is presented in appendix A.6 and exhibits the same behavior. We determine the scaled binding time $\tilde{t}_2$ and scaled velocity $\tilde{v}_2$ as a function of the scaled forces f_s and f_d for different concentrations of ATP, see fig. 3.16. In addition, we calculate the crossover lines between the transport regimes as introduced in section 3.3.1 and include them in fig. 3.16. Slow motors with a low ATP concentration unbind before generating substantial strain forces. Hence, the regions of strong coupling, reduced velocity and enhanced unbinding are small. A higher ATP concentration enhances the generation of strain force between the motors, which leads to a shrinkage of the weak coupling region, see fig. 3.16. We expect exactly such a behavior from the approximated values f_d^* given by eq. (3.40) and f_s^* as in eq. (3.46) for smaller values of the single motor velocity v.

Next, we focus on kinesin-1 to study the impact of changing the ATP concentration in more detail. For vanishing ATP concentration, the motors do not step, no forces are built up between the motors and the scaled binding time $\tilde{t}_2$ approaches the value 0.5 for non-interacting motors, see fig. 3.17(a). Increasing the ATP concentration leads to faster stepping and the binding time $\tilde{t}_2$ decreases until it saturates at a minimum. Because of the motor-motor interference, the scaled average velocity decreases for increasing ATP concentration until it saturates at a minimum, see fig. 3.17(b).

In this section, we have shown that the interference of two motors depends on the concentration of ATP. This holds especially with respect to the binding time $\tilde{t}_2$. These generic

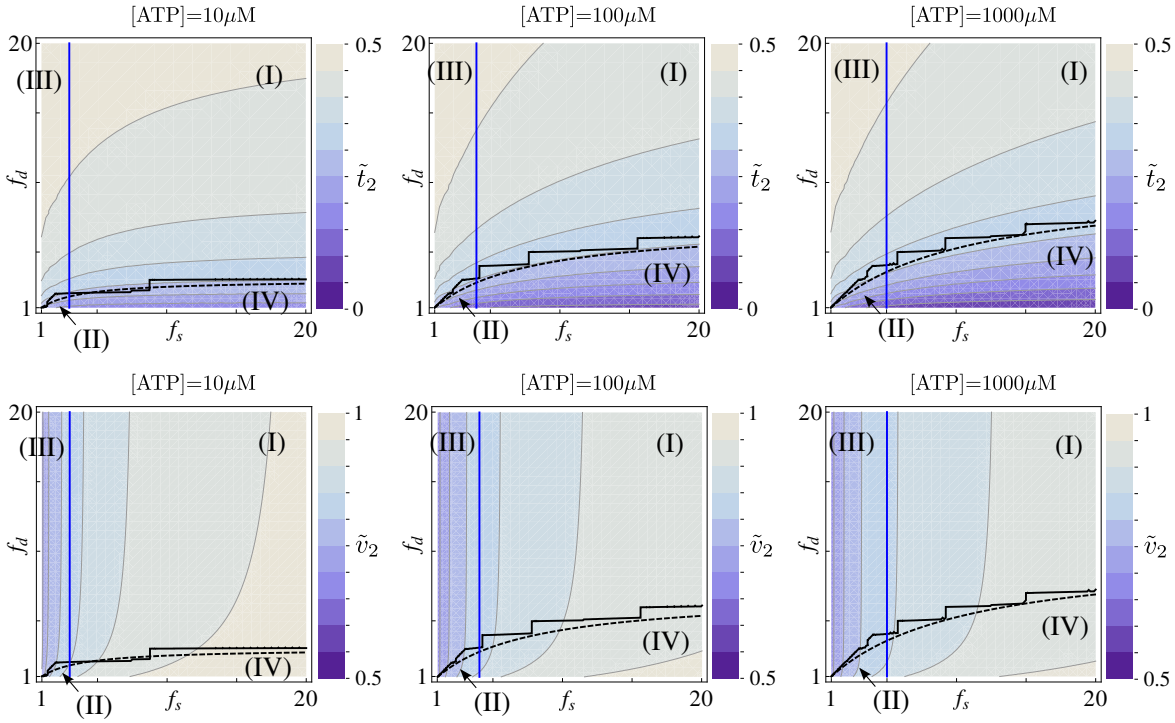

Figure 3.16 Scaled binding time $\tilde{t}_2$ (upper row) and velocity $\tilde{v}_2$ (lower row) for two active motors as a function of the scaled forces f_s and f_d for different concentrations of ATP. The single motors are described by the rates and parameters listed in table 3.2, and the ATP dependence is incorporated via eq. (2.21). The crossover lines between the transport regimes are obtained as explained in section 3.3.1. The solid blue and black line separates (I) the weak coupling, (II) the strong coupling, (III) reduced velocity and the (IV) enhanced unbinding regime. The dashed lines correspond to the approximated crossover line as given by eq. (3.38). Slow motors with low ATP concentration unbind before generating large strain forces between them. Therefore, the regions with a reduced velocity and an enhanced unbinding are rather small compared to the case of high ATP concentration.

predictions could, with the methods used in single molecule experiments, be tested experimentally.

3.4.4. Direction dependent detachment force

Several experiments, studying the rupture of motor-filament bonds, indicate that motor unbinding depends on the loading direction [102,119,120], see also section 2.2.2 for a detailed discussion. In order to study this effect, we introduce a direction dependent detachment

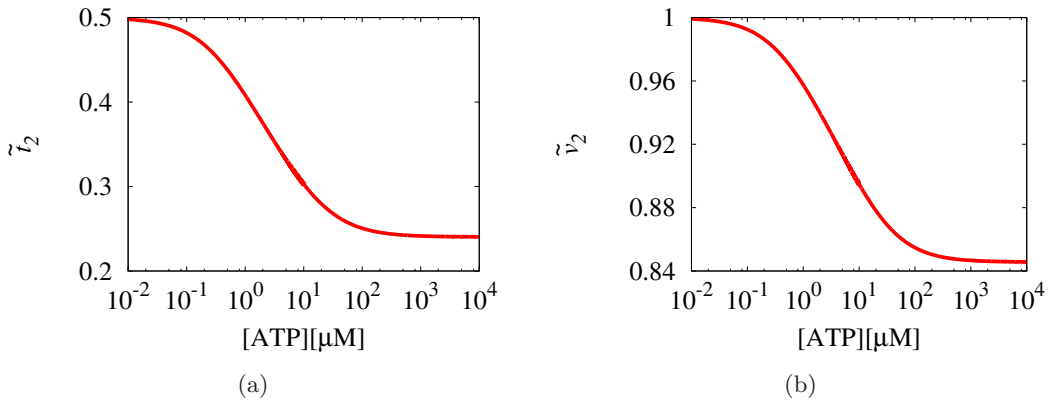

(a) (b)

Figure 3.17 Scaled binding time (a) and velocity (b) as a function of the ATP concentration for two active kinesins with parameters from table 3.1. The single motor velocity depends on the ATP concentration as introduced in eq. (2.21). Slow motors with low [ATP] do not interfere. Higher ATP concentrations lead to motor-motor interference which reduces the binding time (a) and the average velocity (b).

force,

$$F_{\mathrm{d}}(F) = \begin{cases} F_{\mathrm{d}}^{-} & F \leq 0 \\ F_{\mathrm{d}}^{+} & F > 0. \end{cases} \tag{3.52}$$

Note that the plus and minus signs in the notation are chosen to be consistent with the definition of the direction of the load force. We extend our description with a modified unbinding rate from eq. (2.14),

$$\epsilon_1(F) = \epsilon \exp(|F|/F_{\mathrm{d}}(F)). \tag{3.53}$$

So far, we used a detachment force of $F_{\mathrm{d}} \simeq 3\,\mathrm{pN}$ for kinesin-1, which has been deduced from an experiment where a positive load force was applied [94]. Therefore, we set $F_{\mathrm{d}}^{+} \simeq 3\,\mathrm{pN}$ and introduce the ratio

$$\Theta \equiv \frac{F_{\mathrm{d}}^{-}}{F_{\mathrm{d}}^{+}}. \tag{3.54}$$

To obtain a qualitative estimate what to expect from this refinement, we use our time scale arguments developed in section 3.3.1: The time $t_{F_{\mathrm{d}}}$ it takes to generate forces between the motors that are larger or equal to the detachment force, has to be redefined. It is straightforward to define the time $t_{F_{\mathrm{d}}}$ as the time it takes to generate forces larger or equal to the *smallest* detachment force. This definition is motivated by the fact that the motor which pulls along the direction corresponding to the smaller detachment force is more likely to unbind than the other motor. Unbinding leads to termination of the two motor run. Therefore, reducing Θ decreases the time scale $t_{F_{\mathrm{d}}}$ and motor unbinding is induced.

Using the force-dependent detachment force given by eq. (3.52) and the rates and parameters for kinesin-1 listed in table 3.1, we plot the scaled binding time $\tilde{t}_2$ and the scaled

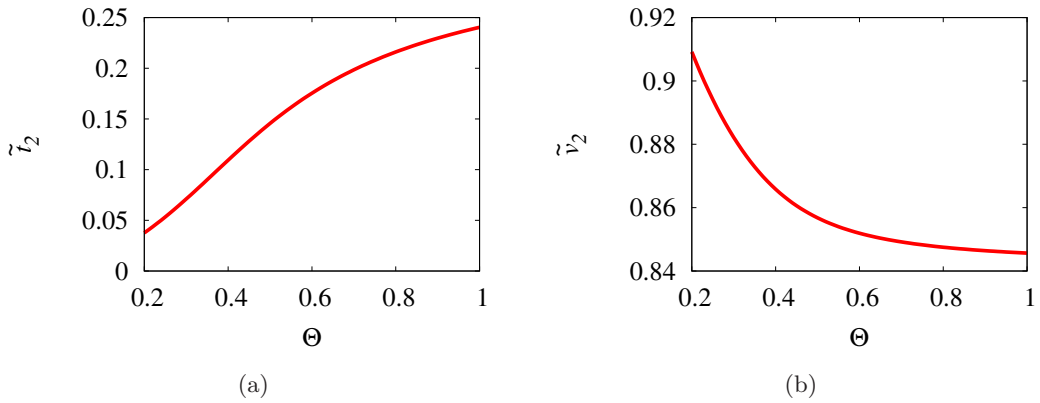

Figure 3.18 Scaled binding time (a) and velocity (b) for a pair of kinesins described by the rates and parameters from table 3.1 with a direction dependent detachment force, see eq. (3.52). The variable $\Theta = F_{\mathrm{d}}^{-}/F_{\mathrm{d}}^{+}$ is the ratio of the detachment force towards the minus and the plus load direction, F_{d}^{-} and F_{d}^{+}, respectively. Reducing this ratio leads to enhanced unbinding with a reduced interference effect on the velocity.

velocity $\tilde{v}_2$ as a function of the ratio Θ. For small Θ, the binding time is reduced and the motors unbind before generating considerably large forces, see fig. 3.18(a). Since the strain force generation between the motors is reduced by reducing Θ, we find an increase of the scaled velocity $\tilde{v}_2$ when decreasing Θ, see fig. 3.18(b). The experiments by Ishiwata et al. [102] indicate that $\Theta \simeq 0.69$.

3.4.5. Cables as non-linear elastic motor linkers

The description of elastic molecules as linear springs is only valid for small forces. For biomolecules, we expect a non-linear relation between the force and the extension of the molecule, that is, in contrast to the spring, limited by a finite length before rupture. In addition to the linear spring, we introduced a freely jointed chain (FJC), a worm like chain (WLC) and a cable model in section 2.2.1. Whereas our description, or, more precisely, the state space, has to be extended for the cables, the FJC and the WLC or any other force extension relation can be easily included into our description via eq. (3.4). A detailed study presented in appendix A.7 reveals that the overall effect of non-linear linkers, like the FJC and the WLC, on the properties of a motor pair is rather small. This result justify the approximation of the linkers as linear springs. In the following, we study the more interesting case of cable-like linkers and explain how to describe them with an extension of the state space.

In several different studies of cooperative motor transport, the elastic linker of a motor has been described by a cable model introduced in section 2.2.1. In this simple model of a polymer, the force extension relation is split into two regions, see eq. (2.16). In the compression mode, where the extension is smaller than its rest length l_0, no strain forces

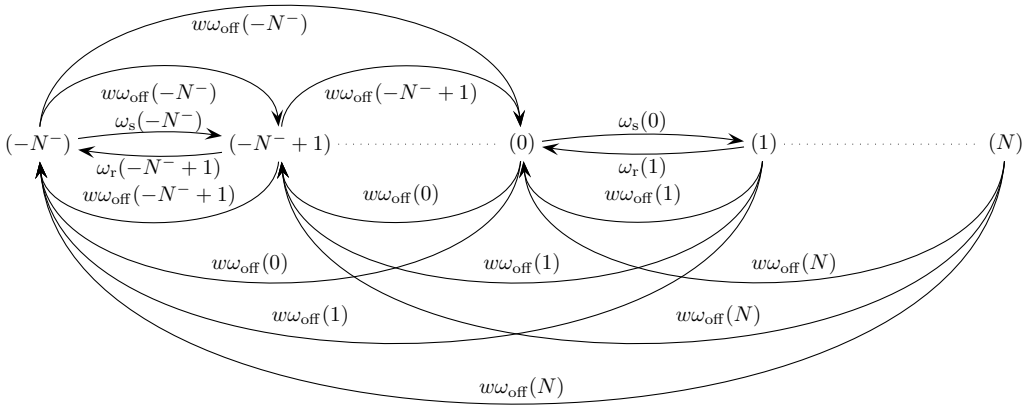

Figure 3.19 Extended state space of the network shown in fig. 3.4 to account for cable like linkers. In the states with the negative index $(-1)\dots(-N^-)$, the linkers are in the compression mode and no force is generated between the motors. All these states are possible starting states and the unbinding transitions are redirected to these states with equal probability $w(i) = w$.

are generated. In the stretch mode, where the extension is larger than the rest length l_0, a linear force extension relation applies.

In the case of two coupled motors, two cables corresponding to the stalk of each motor are connected, which results in an effective rest length of $2l_0$. Before we incorporate such a behavior into our description, let us use the timescale arguments from section 3.3.1 to discuss what we expect qualitatively. When both motors start working together in the compression mode, where the linkers are relaxed, no forces are built up between the motors until their linkers are stretched at a distance larger than $2l_0$. The motors need a certain time to leave the compression mode. This results in an offset time, which is the time it takes until the motors interact via their linkers. For the extreme case, where two kinesins have to walk away from each other for a distance of $2l_0 \simeq 160\,\text{nm}$ [122] to leave the compression mode, we estimate the offset time. Since the motors do not interact in the compression mode, the distance between them is either increased by a step of the motor and decreased by a step of the other motor and both transitions take place with the same rate α. This results in a one dimensional random walk with a mean first passage time $\tau_{\text{D}} = \frac{(2l_0)^2}{2D}$, where $D = l^2\alpha$, since the average dwell time per site is $1/2\alpha$. Thus, we estimate, using $\alpha \simeq 125\,\text{s}^{-1}$ from table 3.1, an offset time $\tau \simeq 1.6\,\text{s}$, which contributes to the time $t_{F_{\text{d}}}$ it takes to generate forces comparable to the detachment force. For this reason, we expect, that in models using cable-like linkers, $t_{F_{\text{d}}} > t_{\text{u}}$, and thus the interference is rather small or even vanishing [43, 45, 133].

To account for such cable-like linkers in our description, we have to extend the state space of fig. 3.4. We add N^- states with a negative index[3], which are associated with the

[3]The choice of a negative index ensures that the state in which the motors are one step apart still corresponds to state (1) as before.

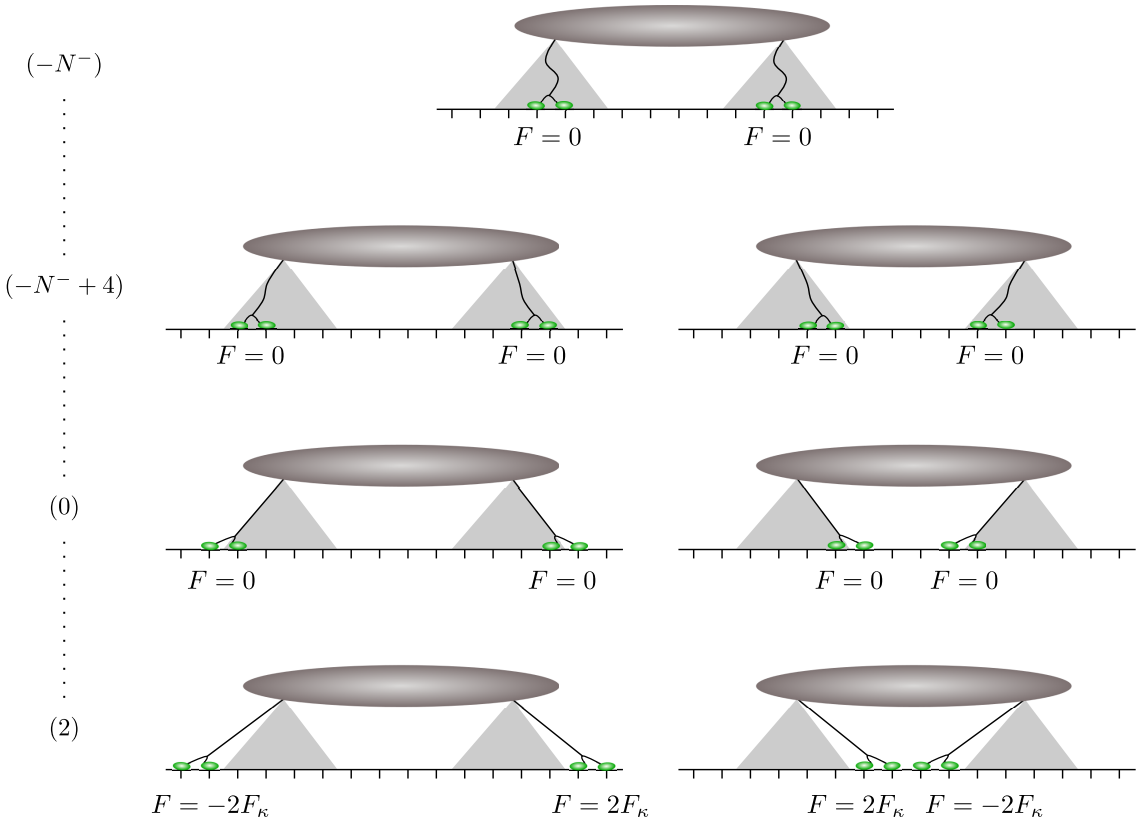

Figure 3.20 State space and the corresponding motor configurations. Because of the geometry assumed, all states except for state $(-N)$ have two motor configurations. The areas shaded in gray are associated with the compression mode of the linkers. When the motors are in this area, no force is built up.

compression mode, i.e. $F_i = 0$ for all these states, see fig. 3.19. The number N^- of these states depends on the rest length l_0. For example, if $l_0 = 0$, there is no compression mode and therefore $N^- = 0$ and we recover the case of a linear spring. For convenience, we choose the rest length l_0 as a multiple of the step size l and therefore $N^- = 2l_0/l$. Otherwise an appropriate rounding function has to be introduced. We illustrate the system in fig. 3.20, in which the shaded gray areas are associated with the compression modes. Because of the assumed geometry, we do not distinguish whether motors walk towards each other or away from each other, compare fig. 3.2(a). Therefore, we assign to every state $(-N^- + 1) \dots (N)$ two configurations that correspond to the two columns in fig. 3.20. The only state with a unique configuration is the state (N^-), in which the effective distance is zero. Accordingly,

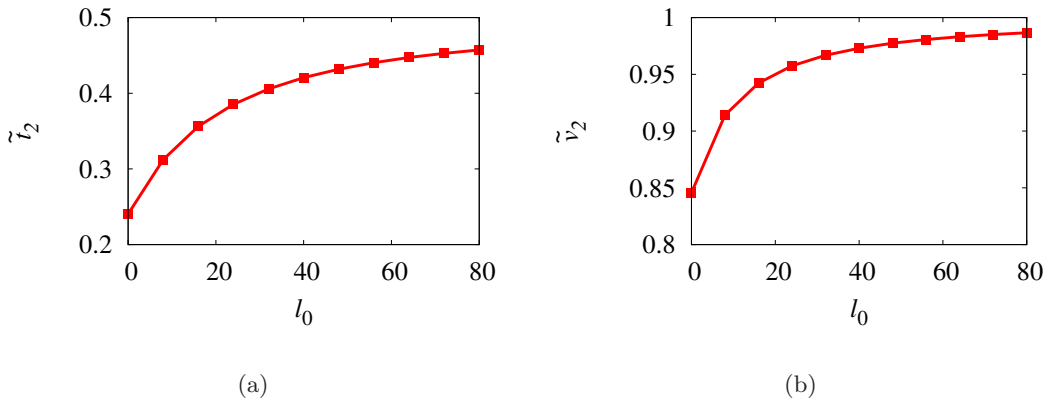

(a) (b)

Figure 3.21 (a) Scaled binding time $\tilde{t}_2$ and (b) scaled velocity $\tilde{v}_2$ of two active kinesins described by the rates and parameters from table 3.1 with cable like linkers as a function of the rest length l_0 of the cable. For l_0 approaching the length of kinesin-1, 80 nm, see table 2.1, the interference effect of the binding time and the velocity is strongly reduced.

we adjust the rates for stretching, relaxation and unbinding:

$$\omega_{\mathrm{s}}(i) = \begin{cases} 2[\alpha(0)+\beta(0)] & i = N^- \\ \alpha(0)+\beta(0) & N^- < i \leq 0 \\ \alpha(F_i)+\beta(-F_i) & 0 < i < N, \end{cases} \tag{3.55}$$

$$\omega_{\mathrm{r}}(i) = \begin{cases} \alpha(0)+\beta(0) & N^- < i \leq 0 \\ \alpha(-F_i)+\beta(F_i) & 0 < i \leq N, \end{cases} \tag{3.56}$$

$$\omega_{\mathrm{off}}(i) = \begin{cases} 2\epsilon_1(0) & N^- \leq i \leq 0 \\ \epsilon_1(F_i)+\epsilon_1(-F_i) & 0 < i \leq N. \end{cases} \tag{3.57}$$

Note, for $N^- = 0$, we obtain the rates specified in eqs. (3.5) - (3.7).

There are now $N^- + 1$ force-free states, in which the linkers are relaxed. All of these states are possible initial states. Again, we assume that when on motor is active, the other motor binds with equal probability $w = 1/(N^- + 1)$ into one of these $N^- + 1$ force-free states shown in fig. 3.19.

Using the standard rates and parameters from table 3.1, we determine the steady state probability distribution for the closed network of fig. 3.19. In fig. 3.21, we show the scaled binding time $\tilde{t}_2$ and the scaled velocity $\tilde{v}_2$ as a function of the rest length l_0. This rest length determines the number of states in the compression mode. For large rest length l_0, the interference effect on the binding time and the velocity vanishes. Hence, the motors unbind spontaneously before generating substantially large forces. Returning to our time scale argument, we calculate the time scale $t_{F_{\mathrm{d}}}$ by setting all $\omega_{\mathrm{off}} = 0$ and promoting the state, where the force is equal to or higher than the detachment force, to an absorbing state. As argued in the beginning of this section, the time $t_{F_{\mathrm{d}}}$ increases with the rest length l_0,

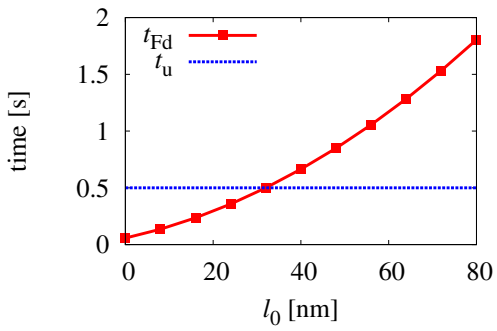

Figure 3.22 Time scale t_{F_d} and t_u as a function of the rest length l_0 of cable-like linkers. For large rest length, the time t_{F_d} to generate forces comparable to the detachment force is longer than the time t_u for spontaneous unbinding. Thus, the system mainly unbinds spontaneously and the interference effect is rather small.

see fig. 3.22. Already for a rest length of $l_0 > 30\,\mathrm{nm}$, we have $t_{F_d} > t_u = 1/2\epsilon \simeq 0.5\,\mathrm{s}$ and the system is dominated by spontaneous unbinding.

In summary, describing the motor linkers as cables leads to a decrease of the elastic coupling strength and thus of the interferences. Therefore, the interference was rather small or even vanishing in previous studies, where motor linkers were described as cables [43, 45, 133].

3.5. General inequalities involving transport quantities of motor pairs

In this section, we derive quite general relations between transport quantities of two elastically coupled motors. These relations are useful to estimate and deduce single motor parameters and coupling forces from experimental data.

Using the probability distribution of the fluctuating forces between the motors, we rewrite the inverse binding time, eq. (3.9), with eq. (3.47) as

$$t_2^{-1} = \sum_i 2\epsilon e^{|F_i|/F_d} P(F_i) \equiv \left\langle 2\epsilon e^{|F|/F_d} \right\rangle . \tag{3.58}$$

For an estimate, we use Jensens's inequality, $\exp(\langle x \rangle) \leq \langle \exp(x) \rangle$, and obtain an upper bound for the average of the absolute value of the force exerted on one motor,

$$F_d \ln \frac{t_1}{2t_2} \geq \langle |F| \rangle , \tag{3.59}$$

where $t_1 = 1/\epsilon$. The left hand side of this equation should be, in principle, accessible in experiments. The values F_d and ϵ can be determined by force-dependent run time measurements of single motor proteins [94] and t_2 has been estimated in the Diehl experiment [25].

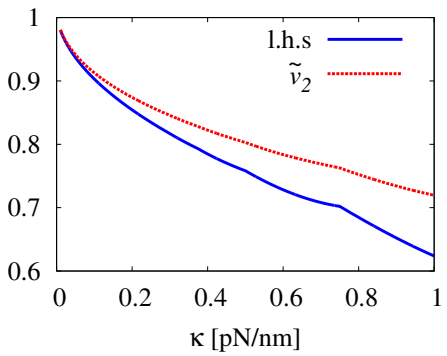

Figure 3.23 Illustration of the inequality given by eq. (3.63). We use the standard kinesin rates and parameters summarized in table 3.1 and calculate $\tilde{t}_2$ and $\tilde{v}_2$ using our framework as discussed in the text. We plot the left hand side (l.h.s.) of eq. (3.63) and $\tilde{v}_2$ as a function of κ.

Note, this inequality is independent of the precise description of the coupling, which makes the relation remarkably general. Obviously, for non-interacting motors, where $t_2 = t_1/2$, there are no average forces between the motors, i.e. $\langle |F| \rangle = 0$. Using the experimental values for kinesin-1, $\epsilon_2 \simeq 4\,\mathrm{s}^{-1}$ and $\epsilon \simeq 0.61\,\mathrm{s}^{-1}$ from the Diehl experiment [25] and $F_\mathrm{d} \simeq 3\,\mathrm{pN}$ [94], we obtain the estimated average force $\langle |F| \rangle = 3.56\,\mathrm{pN}$ that is roughly one half of the stall force. Assuming the linear force extension relation given by eq. (3.25), we find

$$\langle |F| \rangle = \frac{\kappa l}{2} \langle i \rangle \,, \tag{3.60}$$

where $\langle i \rangle$ is the effective distance between the motors.

In future experiments, it should be possible to obtain values for this distance. Recently, the distances between molecular motors have been measured with nanometer precision using a method that combines different colored Qdots and TIRF-microscopy [101]. Another possibility might be to use quick-freeze deep-etch EM [10] to image a large ensemble of motor pair complexes constructed as in the Diehl experiment [25] and analyze their motor-motor distance.

Using the force-velocity relation of eq. (2.20), we rewrite the definition of the average velocity given by eq. (3.18), as

$$v_2 = \frac{1}{2}\left(2v + \frac{\kappa l}{2F_\mathrm{s}} \sum_i i P_i\right). \tag{3.61}$$

Inserting eq. (3.60) and eq. (3.59) into this expression, we obtain the inequality

$$1 - \frac{F_\mathrm{d}}{2F_\mathrm{s}} \ln \frac{t_1}{2t_2} \leq \frac{v_2}{v}, \tag{3.62}$$

which becomes, with using the scaled time and velocity given by eq. (3.31) and eq. (3.32),

$$1 + \frac{F_\mathrm{d}}{2F_\mathrm{s}} \ln 2\tilde{t}_2 \leq \tilde{v}_2. \tag{3.63}$$

This inequality relates the average binding time and the average velocity of two active motors. For non-interacting motors, we have $v_2 = v$ and $t_2 = t_1/2$ and the equality holds. For the standard kinesin rates and parameters summarized in table 3.1, we calculate t_2 and v_2 from our two motor description as a function of the coupling strength κ and plot the inequality in fig. 3.23. As expected, the inequality approaches the equality as the coupling becomes small.

3.6. Analytical estimates for the binding time and velocity of a motor pair

In this section, we derive a non-algebraic equation for approximating t_2. Furthermore, we use this approximation to estimate the average velocity v_2. To calculate t_2 according to eq. (3.9), we need to know the distribution P_i of the distances between the motors. The basic idea of the approximation is to use the distribution of distances from non-interacting motors. For non-interacting motors which are not able to unbind, the distribution of the absolute value of the effective distance is obtained from the Skellam distribution [141],

$$P_\mathrm{sk}(i,t) = \begin{cases} e^{-2\alpha t} I_{(0)}(2\alpha t) & i = 0 \\ 2e^{-2\alpha t} I_{(i)}(2\alpha t) & i > 0 \end{cases} \tag{3.64}$$

where i is the absolute value of the distance in units of the step size l between the two motors, α is the stepping rate, t the time and $I_{(i)}$ are the modified Bessel functions. This distribution of the distance between two identical Poisson walkers has been first derived by Irwin [142]. It is obtained from the cross-correlation of two identical Poisson distributions.

Since the elastic coupling of the motors leads to an effective attractive interaction, the distances between the motors have a finite distribution. In contrast, the average distance between two non-interacting motors increases with time. Using the distances between two non-interacting motors to calculate the forces between two coupled motors, we always overestimate the distance and thus the forces between the motors. Next, we have to choose a point in time to evaluate the distribution given by eq. (3.64). On average, one of the two coupled motors unbinds after the time $t = 1/\epsilon_2$. Therefore, we use the Skellam distribution at that time and obtain the non-algebraic equation for the binding time from eq. (3.9)

$$t_2^{-1} = 2e^{-2\alpha t_2} I_{(0)}(2\alpha t_2) + \sum_{i=1}^{\infty} 4\epsilon e^{\frac{F_i}{F_\mathrm{d}} - 2\alpha t_2} I_{(i)}(2\alpha t_2). \tag{3.65}$$

Since we overestimate the forces, this equation provides a lower bound for t_2. A very good and reasonable improvement of this lower bound is to restrict the summation in such a way that only forces equal to or smaller than the stall force appear. Together with the linear

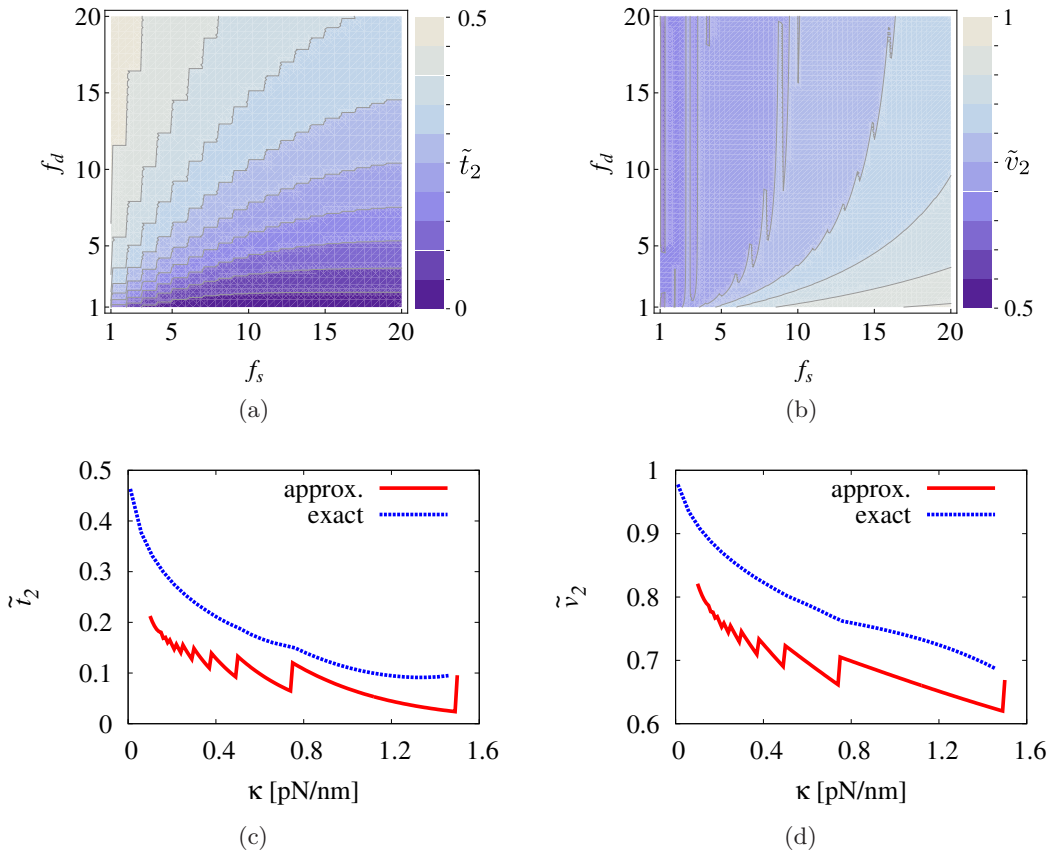

Figure 3.24 (a) Scaled binding time $\tilde{t}_2 = t_2/t_1$ as estimated via eq. (3.66) with parameters from table 3.2 as a function of the scaled detachment force f_d and the scaled stall force f_s. (b) Scaled velocity $\tilde{v}_2 = v_2/v$ as estimated via eq. (3.67) with parameters listed in table 3.2 and t_2 from eq. (3.66) as a function of the scaled detachment force f_d and the scaled stall force f_s. Both quantities are underestimated compared to the exact solution shown in fig. 3.6. (c) Approximated scaled binding time $\tilde{t}_2$ and (d) scaled velocity $\tilde{v}_2$ as a function of the stiffness κ with kinesin rates and parameters of table 3.1 compared to the corresponding exact solution.

force extension relation of eq. (3.25) and the scaled forces, the approximation for the binding time reads

$$t_2^{-1} = \mathcal{N} 2e^{-2\alpha t_2} I_{(0)}(2\alpha t_2) + \mathcal{N} \sum_{i=1}^{\lceil f_\mathrm{s} \rceil} 4\epsilon e^{\frac{i}{f_\mathrm{d}} - 2\alpha t_2} I_{(i)}(2\alpha t_2). \tag{3.66}$$

Here, $\mathcal{N}$ is a normalization factor which ensures that the truncated probability distribution is normalized, i.e. $\sum_{i=0}^{\lceil f_\mathrm{s} \rceil} PS(i, t_2) = 1$, and $\alpha = v/l$ is the stepping rate. Using a numerical root finding algorithm [137], we plot this approximation as a function of the scaled forces in fig. 3.24(a). In comparison to the exact solution shown in fig. 3.9(a), we underestimate

the binding time as expected. The sharp steps in the contour lines arise from the ceiling function in the upper limit of summation in eq. (3.66).

Together with the approximated binding time t_2, it is straightforward to determine the average velocity from eq. (3.18),

$$v_2 = \frac{1}{2}\mathcal{N}\sum_{i=0}^{\lceil f_\mathrm{s}\rceil}(\mathcal{V}(F_i)+\mathcal{V}(-F_i))P_\mathrm{sk}(i,t_2). \tag{3.67}$$

We plot the average velocity as a function of the scaled forces in fig. 3.24(b). Compared to the full solution displayed in fig. 3.9(b), the average velocity is also underestimated and the spikes of the contour line are artifacts from the ceiling function.

As a detailed example, we consider a pair of kinesin-1 motors and approximate the scaled binding time $\tilde{t}_2$ form eq. (3.66) and the and the scaled velocity $\tilde{v}_2$ from eq. (3.67) as a function of the coupling stiffness κ and compare them to the exact solution from eq. (3.9) and eq. (3.18) in fig. 3.24(c) and fig. 3.24(d). In both cases, the approximation underestimates the exact solution. Note, the steps in the function arise again from the ceiling function in the equation.

Furthermore, the advantage of the approximation is that it relates t_2 to single motor parameters. With the parameters listed in table 3.1, the binding time from eq. (3.65) is $t_2 \simeq 0.15\,\mathrm{s}$. This lower bound value can be used to estimate, through eq. (3.59), an upper bound for the average force between the motors, $\langle|F|\rangle < 3.6\,\mathrm{pN}$. This force is comparable to the detachment force $F_\mathrm{d} \simeq 3\,\mathrm{pN}$ for kinesin.

In conclusion, the strain force estimated from the approximation is large enough to enhance the unbinding. Indeed, such an effect on the binding time has been found experimentally and will be discussed quantitatively in the next section.

3.7. Comparison to experimental results

In this section, we quantitatively discuss the experiments of the Diehl lab carried out by Rogers et al. [25]. In this study, the transport of two coupled kinesins has been characterized. Using our framework, we propose a set of single motor parameters, which reproduces the experimental results of the two kinesin constructs.

Recently, the Diehl lab successfully fused two kinesin-1 (K560) via a DNA scaffold, see fig. 1.4. The kinesins are truncated after 560 amino acids and fused with a polypeptide linker to a DNA strand. This DNA scaffold provides a spacing of 50 nm between the motors [25]. Following a Qdot attached to the DNA, they have been able to study transport by precisely two kinesin-1 motors. The average velocity was $(492 \pm 85)\,\mathrm{nm/s}$, similar to single kinesin assays of $(490 \pm 132)\,\mathrm{nm/s}$ determined in a control experiment. The overall average run length of the cargo was $(1380 \pm 81)\,\mathrm{nm}$ and, as expected larger compared to the run length of a single kinesin $(800 \pm 60)\,\mathrm{nm}$ recorded in the corresponding control experiment. Analyzing their trajectories Rogers et al. were able to estimate the effective unbinding rate of two active motors as $\epsilon_2 \simeq 4\,\mathrm{s}^{-1}$, where as the single unbinding rate has been determined as

		(i) simple approach without fit	(ii) simple approach with fit	results from Diehl experiment
input	$\mathcal{V}(F)$	eq. (3.50), $a = 1$	eq. (3.50), $a = 1$	-
	v [nm/s]	490 [25]	490 [25]	490 ± 132 [25]
	κ [pN/nm]	0.2 [25]	0.2 [25]	0.2 [25]
	F_s [pN]	6 [95]	6 [95]	-
	F_d [pN]	3 [94]	3 [94]	-
	Θ	-	-	-
	ϵ [s^{-1}]	0.61 [25]	0.61 [25]	0.61 [25]
	π [s^{-1}]	5 [24]	fit	-
fit		-	$\pi \simeq 1.46\,\mathrm{s}^{-1}$	
results	ϵ_2 [s^{-1}]	1.89	1.89	4 [25]
	v_2 [nm/s]	490	490	-
	$\langle \Delta x_\mathrm{ca} \rangle$ [nm]	2928	1424	1380 ± 81 [25]
	v_ca [nm/s]	490	490	492 ± 85 [25]

		(iii) Carter and Cross data	(iv) proposed parameters	results from Diehl experiment
input	$\mathcal{V}(F)$	eq. (A.13)	eq. (A.13)	-
	v [nm/s]	490 [25]	490 [25]	490 ± 132 [25]
	κ [pN/nm]	0.2 [25]	0.2 [25]	0.2 [25]
	F_s [pN]	7 [26]	7 [26]	-
	F_d [pN]	3 [94]	1.8 [41]	-
	Θ	-	0.69 [102]	-
	ϵ [s^{-1}]	0.61 [25]	0.61 [25]	0.61 [25]
	π [s^{-1}]	fit	fit	-
fit		$\pi \simeq 1.84\mathrm{s}^{-1}$	$\pi \simeq 3.39\,\mathrm{s}^{-1}$	
results	ϵ_2 [s^{-1}]	2.24	4.35	4 [25]
	v_2 [nm/s]	450	459	-
	$\langle \Delta x_\mathrm{ca} \rangle$ [nm]	1409	1390	1380 ± 81 [25]
	v_ca [nm/s]	472	476	492 ± 85 [25]

Table 3.5 Overview of different sets of parameters used to explain the results from the Diehl experiment (right column) of a cargo transported by two kinesin-1 motors. The parameters of the row named 'input' are used for the single motor description. In the case of using a fit parameter, it is listed in the row 'fit' and the fitting procedure is explained in appendix A.9. The unbinding rate $\epsilon_2 = 1/t_2$ and the velocity v_2 of two active motors are obtained from our two motor descriptions and summarized in the row 'results'. There, the average run length of a cargo transported by two motors is calculated from eq. (3.2) and its velocity from eq. (3.3).

$\epsilon \simeq 0.61\,\mathrm{s}^{-1}$, leading to a single motor binding time $t_1 = 1/\epsilon \simeq 1.64\,\mathrm{s}$ and a motor pair binding time $t_2 = 1/\epsilon_2 \simeq 0.25\,\mathrm{s}$. These results are summarized in table 3.5.

As already discussed in section 3.3.2, we expect the two kinesins to operate in the enhanced unbinding region, see the star in fig. 3.10. From this point of view, our two motor description is qualitatively consistent with the experimental data. In order to compare numerical values from our two motor description to the experimental data, we have to specify all single motor parameters. Since no force-dependent measurements of the single motors have been done in the Diehl experiment, we use single motor parameters obtained in other experiments. However, we also discuss the case of fitting the binding rate π, since we expect that this parameter could be very different for different experiments as discussed in section 2.2.2. In this case the binding rate is obtained from a least square fit to the run length distribution of the experimental data as explained in appendix A.9. We present results for four different sets of single motor parameters, summarized in table 3.5: (i) Rates from the most simple approach with a linear force-velocity relation, eq. (3.50) with $a = 1$, and all parameters taken from experiments; (ii) The same parameters as (i), except that the binding rate is obtained from a fit; (iii) Forward and backward stepping rates from an empirical force-velocity relation, eq. (A.13), introduced in appendix A.4 and scaled to match the single motor velocity obtained in the Diehl experiment. The binding rate π is fitted; (iv) Proposed set of parameters that yield a good agreement to the experimental data. Here, we use the force-velocity realtion as for (iii) with the stall force obtained by Carter and Cross [69] and the detachment force estimated from an assay experiment [41] with the direction dependence discussed in section 3.4.4. Additionally, we obtain the binding rate π from a fit.

The results from our two motor description for each set of parameters are summarized in table 3.5 and compared to the results from the Diehl experiment. The enhanced unbinding rate obtained in the experiment is rather large. With the coupling stiffness $\kappa \simeq 0.2\,\mathrm{pN/nm}$ determined in the same experiment, a good agreement between experiment and theory can be obtained by reducing the single motor detachment force. In this way, our proposed parameters, listed in table 3.5, are in a good agreement with the experimental data, see also fig. 3.25. The unbinding rate $\epsilon_2 = 1/t_2$ is too small for all other sets of parameters. However, a good agreement of the average run length is always obtained when π is fitted via the run length distribution.

3.8. Properties of the overall cargo run

Finally, we integrate our results into the general framework developed in [30], to describe the properties of a cargo transported by two motors. Such a cargo is described by three states shown in fig. 3.1. Since we introduced a theory that relates the parameters $\epsilon_2 = 1/t_2$ and v_2 to single motor properties, we are able to determine all rates and velocities for the network from single motor parameters. Together with the rebinding rate $\pi \simeq 5\,\mathrm{s}^{-1}$ (see table 2.1), the parameters given in table 3.2 and the two motor parameters $\epsilon_2 = 1/t_2$ and v_2 as determined in fig. 3.9, we obtain the average binding time $\langle \Delta t_{\mathrm{ca}} \rangle$, eq. (3.1), the average run length, $\langle \Delta x_{\mathrm{ca}} \rangle$, eq. (3.2), and the average velocity v_{ca} of the cargo, eq. (3.3), as a

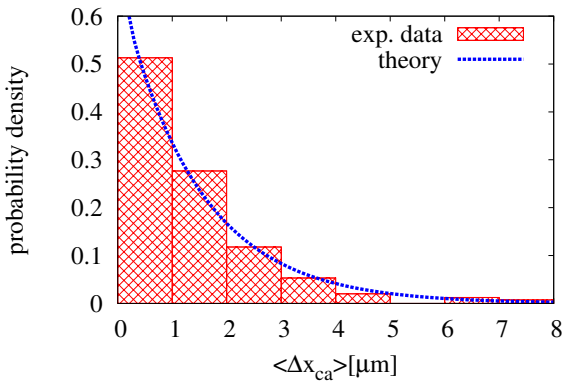

Figure 3.25 Probability density for the run length distribution of the overall run length of the two kinesin complex. The experimental histogram is taken from the Diehl experiment [25] and has been normalized. The theoretical probability density is determined from the parameters we proposed, listed in table 3.5 and the binding rate π as a single fit parameter.

function of the scaled detachment force f_d and scaled stall force f_s, shown in fig. 3.26. The average binding time and the average velocity of the cargo reveal the four distinct transport regimes of: (I) weak coupling, (II) strong coupling, (III) reduced velocity and (IV) enhanced unbinding. The crossover lines are taken from fig. 3.9 and separate the transport regimes. However, the occurrence of these regimes on the cargo level crucially depends on the binding rate. For small binding rates, the cargo is primarily transported by one active motor and the transport regimes of the state, in which both motor actively pull the cargo, does not influence the overall cargo run substantially. The average run length shown in fig. 3.26(c) is larger compared to the single motor run length of 1 μm in all transport regimes, even in the strong coupling regime in the lower left corner.

3.9. Summary

We introduced a general theoretical framework to describe and understand cooperative cargo transport by two identical molecular motors. The stochastic stepping of the motors leads to the build-up of elastic strain forces between them. However, whether these forces have a significant effect on the binding time and/or the velocity, depends on the single motor parameters and on the type and strength of the elastic coupling. More precisely, we identified four distinct transport regimes: (I) a *weak coupling* regime in which the binding time and the velocity are hardly affected by coupling; (II) a *strong coupling* regime with a reduced velocity and a reduced binding time; (III) a *reduced velocity* regime characterized by a reduced velocity without an effect on the binding time and (IV) an *enhanced unbinding* regime with a reduced binding time but an essentially unchanged velocity, see fig. 3.9. To understand the emergence of these transport regimes, we introduced three time scales

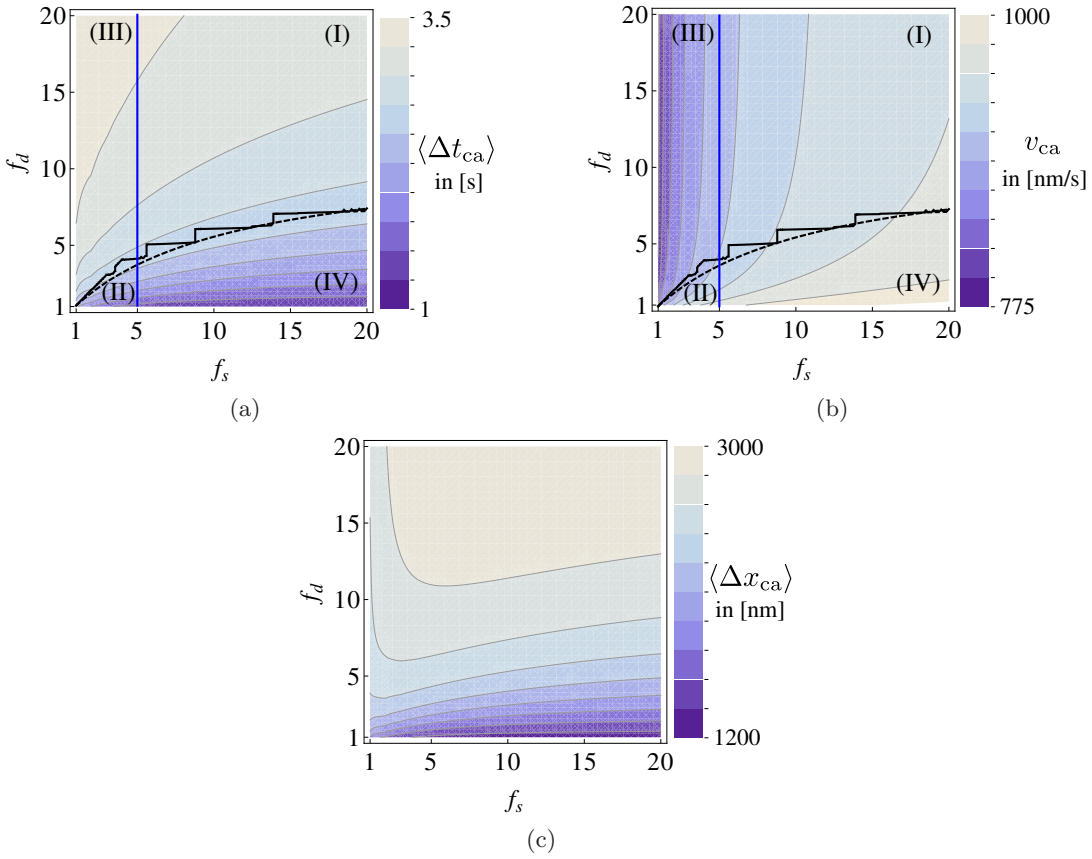

Figure 3.26 Quantities describing a cargo transported by two motors considering the overall cargo run. The motors can unbind from and rebind to the filament as described by the reduced model introduced in section 3.2.1 with rates from table 3.2 and the additional binding rate $\pi \simeq 5\,\mathrm{s}^{-1}$. Together with v_2 and t_2 of fig. 3.9, we plot (a) the average binding time $\langle \Delta t_{\mathrm{ca}} \rangle$ of the cargo from eq. (3.1), (b) the average velocity v_{ca} of the cargo from eq. (3.3) and (c) the average run length $\langle \Delta x_{\mathrm{ca}} \rangle$ of the cargo from eq. (3.1) as a function of the scaled detachment force f_{d} and scaled stall force f_{s}. The binding time and the velocity reveal the four distinct transport regimes as in fig. 3.9 even on this cargo level taking the state with only one bound motor explicitly into account. The crossover lines are taken from fig. 3.9.

associated with the three main processes: spontaneous unbinding, force-induced unbinding, and reduced stepping. Together with the time scale arguments our description allowed us to study transport by two motors using refined single motor properties. In this way, we elucidated the influence of different functional forms of force-velocity relations, of a force-dependent detachment force and cables as motor-cargo linkers. Furthermore, we could clarify why previous studies based on different single motor descriptions came to different

conclusions about the relevance of strain forces and motor-motor interference.

We found a set of single motor parameters, which leads to a transport behavior of a motor pair as found experimentally in the Diehl lab [25], see table 3.5. From our study with different types of motor-cargo linkers, we concluded that the strong motor-motor interference revealed in the experiments can not be explained by a description with cable-like motor-cargo linkers.

Our theory is consistent with the available experimental data [25] and provides quantitative predictions which can be tested experimentally. We predict that different subsets of transport regimes should be observed for different motor types when their coupling strength is varied, see fig. 3.10. In addition, we find that the binding time depends on the ATP concentrations. This effect could also be verified in future experiments.

4. Cargo transport by actively pulling and passively diffusing motors

In the following we present a stochastic description for the transport of a single cargo by one myosin V and one kinesin-1 along a microtubule, as considered in the *in vitro* experiment in [29], see fig. 4.1. Each motor can bind to and unbind from the filament. When bound, the kinesin actively walks into one direction, while myosin V diffuses along the filament. We infer the rates for these stochastic events from part of the experimental data, and then use our model to predict all experimentally measured quantities, finding good agreement. The latter argument implies that the motion of the actively pulling kinesin-1 motor is not influenced by the passively diffusing myosin V. This situation is different from the one discussed in the previous chapter. Now, we consider two different motor species: the passive motor is dragged along the filament and no strain forces are induced that influence the dynamics of the pulling motor. In this way, all kinesin rates remain unchanged in the presence of myosin V. In contrast, however, the myosin V motor experiences a force arising from the kinesin motor and is thus more likely to unbind from the microtubule. Despite this enhanced unbinding, myosin V is still capable of increasing the cargo processivity by a factor of two. We also investigate the effect of several myosins and several kinesins on a cargo, which leads to an exponential increase of the cargo's run length and to an effect on the velocity depending on which motor number is increased.

4.1. Experimental findings

In this section, we briefly review the relevant experimental findings and the setup of the *in vitro* experiment by Ali et al. [29]. First, they mixed 10 nm sized quantum dots (Qdots), which serve as cargos, with full length kinesin-1 in a molar ratio 16:1 to ensure that 95% of Qdots have only a single motor bound [38]. Using a total internal reflection fluorescence (TIRF) microscope, they recorded the trajectories of the Qdots along microtubules which were adhered to a glass coverslip. These Qdots performed a directed movement with an average velocity of $v_\mathrm{k} \simeq (0.88 \pm 0.2)\,\mu\mathrm{m/s}$ and a average run length of $\langle \Delta x_\mathrm{ca} \rangle \simeq (1.7 \pm 0.1)\,\mu\mathrm{m}$. Similar to a previous experiment [58], they found that Qdots coated with full length myosin V diffuse on microtubules with a diffusion coefficient of $D_\mathrm{m} \simeq (0.18 \pm 0.16)\,\mu\mathrm{m}^2/\mathrm{s}$, presumably due to a nonspecific electrostatic interaction [58]. To construct Qdots with both motors bound, first Qdots and kinesin were mixed in a 16:1 molar ratio and then excess myosin V was added. Therefore, the precise number of attached myosins was unknown; however, the small size of the cargo suggests that only a single myosin V was attached to it. Since myosin V and kinesin are roughly of the same length of 80 nm, see table 2.1, Qdots

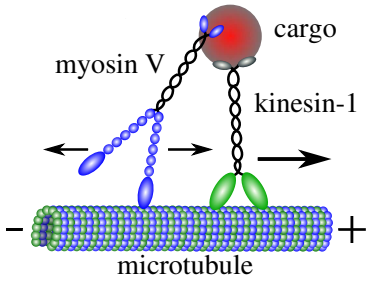

Figure 4.1 A cargo particle that is bound to a microtubule by one actively pulling kinesin-1 and one passively diffusing myosin V. The cargo is transported towards the plus end of the microtubule by kinesin, whereas it diffuses along the microtubule when it is only bound by myosin V, as indicated by the arrows. Motors and filament are not drawn to scale.

could in principle be bound simultaneously by both motors to the filament. Such Qdots coated with both types of motors exhibited a average run length of $\langle \Delta x_{\mathrm{ca}} \rangle \simeq (3.7 \pm 0.3)\,\mu\mathrm{m}$ and an averaged velocity of $\langle v \rangle_{\mathrm{ca}} \simeq (0.73 \pm 0.3)\,\mu\mathrm{m/s}$ on microtubules. These trajectories consisted of directed motion interrupted by diffusive events, see fig. 4.5(a). The parts of the trajectories corresponding to the directed motion had an average length of $(1.8 \pm 0.1)\,\mu\mathrm{m}$ and a average velocity of $(0.84 \pm 0.13)\,\mu\mathrm{m}$. An overview of the quantities measured in [29] is given in table 4.1.

4.2. Stochastic network description

As pointed out in section 2.3.1, in order to establish an appropriate theoretical description, we have to chose a state space and introduce the dynamics on that state space. Our goal is to understand the cooperative motor behavior based on the single motor properties. Since we know the transport properties of the cargo when it is only transported by kinesin or myosin V from the experiment, we chose a state space, in which these cases are included. In this way, we described the cargo in a discrete state space, in which we associate every state with the number of motors bound to the filament.

Since the motors stochastically bind to and unbind from the filament, the cargo transported by one kinesin and one myosin V can be in one of four possible states $(n_{\mathrm{m}}, n_{\mathrm{k}})$ characterized by the numbers n_{m} and n_{k} of bound myosins and kinesins to the filament, respectively, see fig. 4.2. In state $(1, 0)$ only myosin V is bound and in state $(0, 1)$ only kinesin. The dynamics of these states are known from the experiments with only kinesin and only myosin V attached to the cargo. Both motors are bound to the filament in state $(1, 1)$. The state $(0, 0)$ refers to the case in which both motors are unbound. Since in experiments only trajectories on the filament are recorded, we consider the state $(0, 0)$ as an absorbing state. Stochastic motor binding and unbinding events correspond to transitions between the four states, as indicated by the arrows in fig. 4.2. It is unlikely for a freely diffusive cargo to bind

kin.	myo.	$\langle \Delta x_{\mathrm{ca}} \rangle [\mu\mathrm{m}]$	$\langle v \rangle_{\mathrm{ca}} [\mu\mathrm{m/s}]$	$D_{\mathrm{m}} [\mu\mathrm{m}^2/\mathrm{s}]$	n	type of events analyzed
+	-	1.7 ± 0.1	0.88 ± 0.2	-	61	all runs
-	+	-	-	0.18 ± 0.16	-	diffusive motion
+	+	3.7 ± 0.3	0.73 ± 0.3	0.11 ± 0.12	74	all runs
+	+	7.1 ± 1.7	0.55 ± 0.15	-	21	only runs that had obvious diffusive events interspersed
+	+	1.8 ± 0.2	0.84 ± 0.13	-	54	analysis of run segments between diffusive events

Table 4.1 Experimental results from [29] where the transport of Qdots on microtubules has been monitored. The first two columns indicate if kinesin or myosin V is present on the cargo (+) or not (-). Here $\langle \Delta x_{\mathrm{ca}} \rangle$ is the average cargo run length, $\langle v \rangle_{\mathrm{ca}}$ the average velocity of the cargo, D_{m} the diffusion coefficient of the cargo and n is the number of analyzed trajectories. Cargos that are transported by kinesin and myosin V exhibit longer run length compared to single kinesin transport.

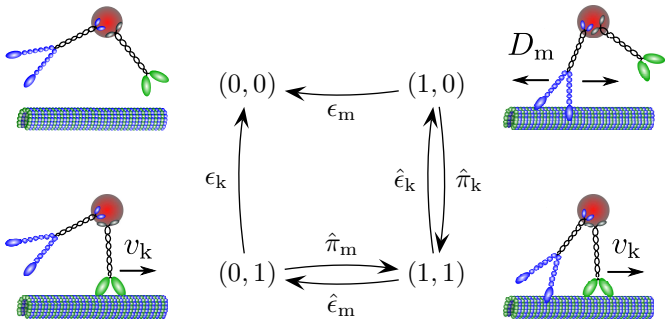

Figure 4.2 State space of a cargo particle transported by one kinesin and one myosin V. The particle can be bound to the microtubule by kinesin only [state $(0,1)$], myosin V only [state $(1,0)$], or both motors [state $(1,1)$], or be in the unbound state $(0,0)$. The transition rates are summarized in table 4.2. Whenever the cargo is bound by kinesin it moves with the velocity v_{k}. Whereas when the cargo is only bound by myosin V, it diffuses along the microtubule with the diffusion constant D_{m}. Motors and filaments are not drawn to scale.

kinesin parameter	myosin V bound?	symbol	value
binding rate	yes	$\hat{\pi}_\mathrm{k}$	$0.2\,\mathrm{s}^{-1}$
unbinding rate	no	ϵ_k	$0.52\,\mathrm{s}^{-1*}$
unbinding rate	yes	$\hat{\epsilon}_\mathrm{k}$	$0.52\,\mathrm{s}^{-1}$
velocity		v_k	$0.88\,\mu\mathrm{m/s}^*$
binding probability		w_k	0.95
myosin V parameter	**kinesin bound?**	**symbol**	**value**
binding rate	yes	$\hat{\pi}_\mathrm{m}$	$0.2\,\mathrm{s}^{-1}$
unbinding rate	no	ϵ_m	$0.020\,\mathrm{s}^{-1*}$
unbinding rate	yes	$\hat{\epsilon}_\mathrm{m}$	$0.1\,\mathrm{s}^{-1}$
diffusion coef.	no	D_m	$0.18\,\mu\mathrm{m}^2/\mathrm{s}^*$

Table 4.2 Single motor parameters for kinesin-1 and myosin V of the model defined in fig. 4.2. Values with an asterisk are determined from the experiments in [29]. The other values were deduced from our model as described in the text.

to the filament in state $(1,1)$ because then kinesin has to bind exactly at the same time as myosin V. Thus, we assume that runs only start either with one kinesin in state $(0,1)$, with probability w_k or with one myosin V in state $(0,1)$, with probability $(1-w_\mathrm{k})$. We expect that the probability for a 'kinesin start' in state $(1,0)$, is much higher than the probability $(1-w_\mathrm{k})$ for a 'myosin V start' in $(1,0)$ since it should be more probable for kinesin to bind to its appropriate filament, the microtubules, than for the actin-motor myosin V. After a kinesin of a freely diffusive cargo has bound to the filament in state $(0,1)$, it can either unbind with transition rate ϵ_k to the absorbing state $(0,0)$ or myosin V of the cargo can bind with binding rate $\hat{\pi}_\mathrm{m}$ leading to state $(1,1)$. Taking possible interactions, which might influence the transition rates, into account, we denote the rates of a motor with a hat when the other motor is bound. From state $(1,1)$ kinesin unbinds with rate $\hat{\epsilon}_\mathrm{k}$ and myosin V with rate $\hat{\epsilon}_\mathrm{m}$. Two transitions from the state $(1,0)$ with only one myosin V bound are possible: into the absorbing state $(0,0)$ with unbinding rate ϵ_m and into state $(1,1)$ with binding rate of kinesin $\hat{\pi}_\mathrm{k}$. An overview of the notation of the rates are given in table 4.2.

In state $(0,1)$ with only kinesin bound, the cargo is pulled with the kinesin velocity $v_\mathrm{k} \simeq 0.88\,\mu\mathrm{m/s}$ measured experimentally in [29]. Since single myosin V diffuses randomly on microtubules, a cargo in state $(1,0)$ moves on average with zero velocity. According to the Einstein relation [143], myosin V's diffusion constant $D_\mathrm{m} \simeq 0.18\,\mu\mathrm{m}^2/\mathrm{s}$ [29] corresponds to a friction coefficient

$$\gamma = \frac{k_\mathrm{B}T}{D_\mathrm{m}} \simeq 0.02\,\mathrm{pN\,s}/\mu\mathrm{m} \tag{4.1}$$

for motion of myosin V on microtubules. When kinesin and myosin V are both bound, the moving kinesin experiences a rather small friction coefficient. It can easily drag myosin V along when moving with its velocity of $v_\mathrm{k} \simeq 0.88\,\mu\mathrm{m/s}$, since myosin V's friction force is

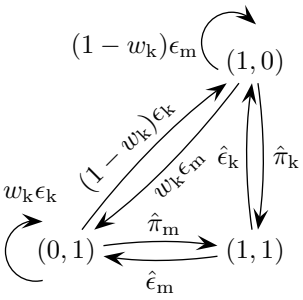

Figure 4.3 (b) Closed network obtained from fig. 4.2 by redirecting all arrows that lead into the absorbing state $(0,0)$ back into the starting states $(0,1)$ and $(1,0)$, weighted with the respective starting probabilities w_k and $(1-w_\mathrm{k})$.

only about

$$F_\mathrm{m} = \gamma v_\mathrm{k} \simeq 0.02\,\mathrm{pN} \tag{4.2}$$

and thus negligible for kinesin that has a stall force of about $6-7\,\mathrm{pN}$, see table 2.1. Therefore, we assume that a cargo in state $(1,1)$ moves with the kinesin velocity v_k.

4.3. Analytical expressions for experimental quantities

To specify the parameters of our model from the experimental data, we derive analytical expressions for averaged quantities measured in the experiments, such as the average run length and the average duration of stepping events.

In order to calculate such quantities, we use our generalization of the method proposed by Hill [126, 128] as presented in section 2.3.3. We recall this method for the calculation of the average run time $\langle \Delta t_\mathrm{ca} \rangle$, which is the average time to absorption in state $(0,0)$. The time $\langle \Delta t_\mathrm{ca} \rangle$ can be determined by averaging the run times of an ensemble of trajectories, each of which starts at time $t=0$ in state $(0,1)$ with probability w_k and in state $(1,0)$ with probability $(1-w_\mathrm{k})$. If one concatenates these trajectories, one obtains a single trajectory which, upon reaching the absorbing state $(0,0)$, immediately continues at state $(0,1)$ with probability w_k, or at state $(1,0)$ with probability $(1-w_\mathrm{k})$. The network that describes such a trajectory is shown in fig. 4.3, which is constructed by 'closing' the 'open' network shown in fig. 4.2, i.e. by eliminating the absorbing state $(0,0)$ and redirecting all arrows that ended in $(0,0)$ to the starting states. For example, the arrow from state $(0,1)$ to state $(0,0)$ with rate ϵ_k is redirected to state $(0,1)$ with the probability weight w_k and to state $(1,0)$ with probability weight $(1-w_\mathrm{k})$. The stationary probabilities $P(n_\mathrm{m}, n_\mathrm{k})$ of the closed network can be calculated by matrix methods [86] or using a diagrammatic method [130, 131], which leads to

$$P(0,1) \equiv \left[\hat{\epsilon}_\mathrm{m}\hat{\pi}_\mathrm{k} + \epsilon_\mathrm{m} w_\mathrm{k}(\hat{\epsilon}_\mathrm{k} + \hat{\epsilon}_\mathrm{m})\right]/\mathcal{N}, \tag{4.3}$$

$$P(1,0) \equiv \left[\hat{\epsilon}_\mathrm{k}\hat{\pi}_\mathrm{m} + (1-w_\mathrm{k})\epsilon_\mathrm{k}(\hat{\epsilon}_\mathrm{k} + \hat{\epsilon}_\mathrm{m})\right]/\mathcal{N}, \tag{4.4}$$

$$P(1,1) \equiv \left[(1-w_\mathrm{k})\epsilon_\mathrm{k}\hat{\pi}_\mathrm{k} + \hat{\pi}_\mathrm{m}(\hat{\pi}_\mathrm{k} + \epsilon_\mathrm{m} w_\mathrm{k})\right]/\mathcal{N}, \tag{4.5}$$

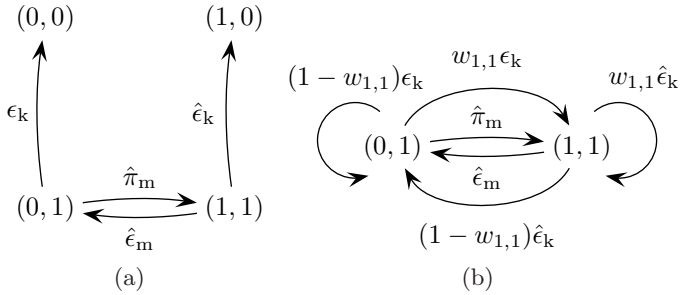

Figure 4.4 (a) Network with absorbing states $(0, 0)$ and $(1, 0)$ modified from fig. 4.2; (b) Closed network obtained from (a) by redirecting the arrows from the states $(0, 0)$ and $(1, 0)$ into the states $(0, 1)$ and $(1, 1)$. The transitions are weighted with the probability $w_{1,1}$ to start in state $(1, 1)$ and $1 - w_{1,1}$ to start in state $(0, 1)$.

where $\mathcal{N}$ is determined by the normalization condition $P(0, 1) + P(1, 0) + P(1, 1) = 1$.

Now, we derive **the average run length** of the cargo. In the steady state, the average rate of arrivals at state $(0, 0)$ is given by the probability current $J \equiv \epsilon_m P(1, 0) + \epsilon_k P(0, 1)$, see section 2.3.2. For the open network in fig. 4.2, this arrival rate corresponds to the average rate of absorptions in $(0, 0)$. Thus, the average time to absorptions is given by

$$\langle \Delta t_{ca} \rangle \equiv \frac{1}{J} = \frac{1}{\epsilon_m P(1, 0) + \epsilon_k P(0, 1)}. \tag{4.6}$$

This average absorption time can also be calculated for the open network in fig. 4.2 using the general theory of Markov processes. The latter calculation confirms the expression (4.6) and provides a non-trivial check of our approach.

The probability $P(n_m, n_k)$ gives the average fraction of time spent in state (n_m, n_k) per run [126], as explained in section 2.3.2. Since there is no cargo displacement in the state $(1, 0)$, the cargo moves only in the kinesin-bound states $(0, 1)$ and $(1, 1)$, i.e. during the time $[P(0, 1) + P(1, 1)] \langle \Delta t_{ca} \rangle$. Since it moves with velocity v_k in these states, the average run length is

$$\begin{aligned} \langle \Delta x_{ca} \rangle &\equiv v_k [P(0, 1) + P(1, 1)] \langle \Delta t_{ca} \rangle \\ &= v_k \frac{\hat{\pi}_k(\epsilon_k + \hat{\epsilon}_m + \hat{\pi}_m) + w_k(\epsilon_m(\hat{\epsilon}_k + \hat{\epsilon}_m + \hat{\pi}_m) - \epsilon_k \hat{\pi}_k)}{\epsilon_k \hat{\epsilon}_m(\epsilon_m + \hat{\pi}_k) + \epsilon_m \hat{\epsilon}_k(\epsilon_k + \hat{\pi}_m)}. \end{aligned} \tag{4.7}$$

Next, we calculate **the average time $\langle \Delta t_{se} \rangle$ of a stepping event**, i.e. the average time spent continuously in the stepping states $(0, 1)$ and $(1, 1)$. In the open network in fig. 4.2, a stepping event can start either from $(0, 1)$ or $(1, 1)$. We first determine the probability $w_{1,1}$ for a stepping event to start in state $(1, 1)$. The average number of transitions from $(1, 0)$ to $(1, 1)$ per unit time in the network of fig. 4.3 is given by the probability current $J_k(1, 1) \equiv \hat{\pi}_k P(1, 0)$. Since a stepping event which starts in state $(0, 1)$ can only occur at the beginning of a run, the average number of these latter events per unit time in the network

of fig. 4.3 corresponds to the probability current

$$J_k(0,1) \equiv w_\mathrm{k}\epsilon_\mathrm{k}P(0,1) + w_\mathrm{k}\epsilon_\mathrm{m}P(1,0) \tag{4.8}$$

from $(0,1)$ and $(1,0)$ to $(0,1)$. This is exactly the sum of the redirected currents which represent a new run starting in state $(0,1)$. Hence, the probability for a stepping event to start in state $(1,1)$ takes the form

$$w_{1,1} \equiv \frac{J_k(1,1)}{J_k(1,1) + J_k(0,1)}. \tag{4.9}$$

A stepping event is finished when the diffusive state $(1,0)$ or the unbound state $(0,0)$ in the network of fig. 4.2 is reached. We therefore promote the state $(1,0)$ to an absorbing state, so that we now have the two absorbing states $(0,0)$ and $(1,0)$, see fig. 4.4(a). By redirecting all arrows from the absorbing states $(0,0)$ and $(1,0)$ to the starting states $(1,1)$ and $(0,1)$, we obtain the network in fig. 4.4(b). Using the stationary probabilities for the latter network, given by

$$Q(0,1) \equiv \frac{\hat{\epsilon}_\mathrm{m} + \hat{\epsilon}_\mathrm{k}(1-w_{1,1})}{\hat{\epsilon}_\mathrm{k}(1-w_{1,1}) + w_{1,1}\epsilon_\mathrm{k} + \hat{\pi}_\mathrm{m} + \hat{\epsilon}_\mathrm{m}} \tag{4.10}$$

$$Q(1,1) \equiv 1 - Q(0,1), \tag{4.11}$$

and the starting probability $w_{1,1}$ from eq. (4.9), we derive the average time of a stepping event $\langle \Delta t_\mathrm{se} \rangle$ from the sum of the probability current into the absorbing states,

$$\langle \Delta t_\mathrm{se} \rangle \equiv \frac{1}{\epsilon_\mathrm{k}Q(0,1) + \hat{\epsilon}_\mathrm{k}Q(1,1)} = \frac{A+B}{\epsilon_\mathrm{k}A + \hat{\epsilon}_\mathrm{k}B}, \tag{4.12}$$

where

$$A \equiv w_\mathrm{k}\epsilon_\mathrm{m}\hat{\epsilon}_\mathrm{k} + w_\mathrm{k}\epsilon_\mathrm{m}\hat{\epsilon}_\mathrm{m} + \hat{\pi}_\mathrm{k}\hat{\epsilon}_\mathrm{m} \tag{4.13}$$

and

$$B \equiv w_\mathrm{k}\epsilon_\mathrm{m}\hat{\pi}_\mathrm{m} + \hat{\pi}_\mathrm{k}\hat{\pi}_\mathrm{m} + (1-w_\mathrm{k})\hat{\pi}_\mathrm{k}\epsilon_\mathrm{k}. \tag{4.14}$$

Another quantity which has been measured in the experiment is **the fraction ϕ_nde of runs without diffusive events**. All of these runs start in state $(0,1)$, and leave the network of fig. 4.2 with the transition to state $(0,0)$ without ever visiting state $(1,0)$. Equivalently, we may ask for the probability of starting in state $(0,1)$ in the network of fig. 4.4(a) and being absorbed in state $(0,0)$ rather than in state $(1,0)$. This splitting probability $w_{0,0}$ is given by the ratio of the probability current from state $(0,1)$ to $(0,0)$ and the total probability current out of the network [128, 131],

$$w_{0,0} \equiv \frac{\epsilon_\mathrm{k}Q(0,1)}{\epsilon_\mathrm{k}Q(0,1) + \hat{\epsilon}_\mathrm{k}Q(1,1)}. \tag{4.15}$$

Since we now consider only runs that start in state $(0,1)$, we use the relations (4.10) and (4.11) with $w_{1,1} = 0$. Finally, we have to take into account that only the fraction w_k of runs

in the original network in fig. 4.2 can contribute to runs without diffusive events. Therefore, the fraction of these latter runs is found to be

$$\phi_{\mathrm{nde}} = w_{\mathrm{k}} w_{0,0} = w_{\mathrm{k}} \frac{\epsilon_{\mathrm{k}}(\hat{\epsilon}_{\mathrm{k}} + \hat{\epsilon}_{\mathrm{m}})}{\epsilon_{\mathrm{k}}(\hat{\epsilon}_{\mathrm{k}} + \hat{\epsilon}_{\mathrm{m}}) + \hat{\epsilon}_{\mathrm{k}}\hat{\pi}_{\mathrm{m}}}. \tag{4.16}$$

Next, we calculate **the average time $\langle \Delta t_{\mathrm{de}} \rangle$ of a diffusive event**. Since only $(1,0)$ is a diffusive state, the average waiting time $\langle \Delta t_{\mathrm{de}} \rangle$ in this state is given by

$$\langle \Delta t_{\mathrm{de}} \rangle = \frac{1}{\epsilon_{\mathrm{m}} + \hat{\pi}_{\mathrm{k}}}. \tag{4.17}$$

In order to compare **the velocity** of the cargo particle with our network description, we point out that the run length and the binding time of the cargo are not independent. In the following, we determine the average over the velocities of the single trajectories,

$$\langle v \rangle_{\mathrm{ca}} \equiv \left\langle \frac{\Delta x_{\mathrm{ca}}}{\Delta t_{\mathrm{ca}}} \right\rangle. \tag{4.18}$$

This velocity $\langle v \rangle_{\mathrm{ca}}$ provides a new quantity, which is useful for the comparison of our description with the experimental data. To calculate the average of the velocities $\langle v \rangle_{\mathrm{ca}}$ as explained in section 2.3.5, we need the probability distribution $P(\Delta x_{\mathrm{ca}}, \Delta t_{\mathrm{ca}})$ of the run length and the binding time of the cargo. We consider the full network of fig. 4.2 with the absorbing state $(0,0)$ and introduce a spatial coordinate x for the position of the cargo. Its position at time t is then described by explicitly taking into account that the cargo moves with velocity v_{k} in state $(0,1)$ and $(1,1)$ and diffuses with diffusion constant D_{m} in state $(1,0)$. The probability $r_{n_{\mathrm{m}},n_{\mathrm{k}}}(x,t)$ of being in state $(n_{\mathrm{m}}, n_{\mathrm{k}})$ is then governed by the following set of equations:

$$\partial_t r_{0,0}(x,t) = \epsilon_{\mathrm{k}} r_{0,1}(x,t) + \epsilon_{\mathrm{m}} r_{1,0}(x,t) \tag{4.19}$$

$$\partial_t r_{0,1}(x,t) = -v_{\mathrm{k}} \partial_x r_{0,1}(x,t) - (\epsilon_{\mathrm{k}} + \hat{\pi}_{\mathrm{m}}) r_{0,1}(x,t) + \hat{\epsilon}_{\mathrm{m}} r_{1,1}(x,t) \tag{4.20}$$

$$\partial_t r_{1,1}(x,t) = -v_{\mathrm{k}} \partial_x r_{1,1}(x,t) - (\hat{\epsilon}_{\mathrm{m}} + \hat{\epsilon}_{\mathrm{k}}) r_{1,1}(x,t) + \hat{\pi}_{\mathrm{m}} r_{0,1}(x,t) + \hat{\pi}_{\mathrm{k}} r_{1,0}(x,t) \tag{4.21}$$

$$\partial_t r_{1,0}(x,t) = D_{\mathrm{m}} \partial_x^2 r_{1,0}(x,t) - (\hat{\pi}_{\mathrm{k}} + \epsilon_{\mathrm{m}}) r_{1,0}(x,t) + \hat{\epsilon}_{\mathrm{k}} r_{1,1}(x,t). \tag{4.22}$$

To solve this set of ordinary differential equations, we have to specify an initial condition. We place the cargo particle at time $t = 0$ at the position $x = 0$ in state $(0,1)$ with probability w_{k} and in state $(1,0)$ with probability $1 - w_{\mathrm{k}}$ resulting in

$$r_{0,0}(x,0) = 0 \tag{4.23}$$

$$r_{0,1}(x,0) = w_{\mathrm{k}} \delta(x) \tag{4.24}$$

$$r_{1,1}(x,0) = 0 \tag{4.25}$$

$$r_{1,0}(x,0) = (1 - w_{\mathrm{k}}) \delta(x). \tag{4.26}$$

Here, $\delta(x)$ is the Dirac delta function. Using the Fourier-Laplace transform from eq. (2.52), the set of equations for $r_{n_{\mathrm{m}},n_{\mathrm{k}}}(x,t)$ can be transformed in a set of linear equations for

$\hat{r}_{n_\mathrm{m},n_\mathrm{k}}(k,\lambda)$ and the average cargo run length and binding time are obtained from derivatives of the current into the absorbing state

$$\hat{J}(k,\lambda) \equiv \epsilon_\mathrm{k}\hat{r}_{0,1}(k,\lambda) + \epsilon_\mathrm{m}\hat{r}_{1,0}(k,\lambda), \tag{4.27}$$

see section 2.3.4. In this way, following from the definition of the Fourier-Laplace transformation of eq. (2.52), we obtain the average run length of the cargo $\langle \Delta x_\mathrm{ca} \rangle$ from eq. (2.55) and the average binding time $\langle \Delta t_\mathrm{ca} \rangle$ from eq. (2.54). These two equation yield the same result as eq. (4.7) and eq. (4.6) and provide a non-trivial check of the derivation using the closed networks. The actual quantity that we are interested in is the average of the velocities, which we also derive from the Fourier-Laplace transform as in eq. (2.58),

$$\langle v \rangle_\mathrm{ca} = \left\langle \frac{\Delta x_\mathrm{ca}}{\Delta t_\mathrm{ca}} \right\rangle = \int_{-\infty}^{+\infty} \int_0^{+\infty} \frac{x}{t}\, J(x,t)\, dt\, dx = -\mathrm{i} \int_0^{+\infty} \partial_k \hat{J}(k,\lambda)|_{k=0}\, d\lambda. \tag{4.28}$$

We have now obtained expressions for the average run length $\langle \Delta x_\mathrm{ca} \rangle$, the average time $\langle \Delta t_\mathrm{se} \rangle$ of stepping events, the average time $\langle \Delta t_\mathrm{de} \rangle$ of diffusive events, the fraction ϕ_nde of runs without diffusive events and the velocity $\langle v \rangle_\mathrm{ca}$. Next, we use these expressions to determine all parameters of our description from the measured quantities.

4.4. Parameters deduced from experiment

When combining the results derived above with the experimental data of [29], we are able to determine all six rates of our model in fig. 4.2, as well as, the starting probability w_k. All parameters are summarized in table 4.2. From different single molecule experiments with only kinesin ($N_\mathrm{m} = 0, N_\mathrm{k} = 1$) and with only myosin V ($N_\mathrm{m} = 1, N_\mathrm{k} = 0$), the unbinding rates of myosin V, ϵ_m, and kinesin, ϵ_k, can directly be derived as the inverse of the average binding time $\langle \Delta t_\mathrm{k} \rangle \simeq 1.93\,\mathrm{s}$ of kinesin and $\langle \Delta t_\mathrm{m} \rangle \simeq 50\,\mathrm{s}$ of myosin V on microtubules [29]. From the measured average time $\langle \Delta t_\mathrm{de} \rangle \simeq 4.5\,\mathrm{s}$ of a diffusive event, we obtain with eq. (4.17) the binding rate $\hat{\pi}_\mathrm{k} \simeq 0.2\,\mathrm{s}^{-1}$. In the experiments, the average time $\langle \Delta t_\mathrm{se} \rangle$ of a stepping event has numerically the same value as the binding time for single kinesin $\langle \Delta t_\mathrm{k} \rangle = 1/\epsilon_\mathrm{k}$. Therefore, we deduce from eq. (4.12) that the unbinding rate $\hat{\epsilon}_\mathrm{k}$ is equal to the unbinding rate ϵ_k. Furthermore, they found in the experiments an average cargo run length $\langle \Delta x_\mathrm{ca} \rangle \simeq 3.7\,\mu\mathrm{m}$, a fraction of 72% of runs that did not show diffusive events and a average velocity $\langle v \rangle_\mathrm{ca} \simeq 0.73\,\mu\mathrm{m/s}$. Using these values, we determine by combining eq. (4.7), eq. (4.16) and eq. (4.28), the remaining parameters $\hat{\epsilon}_\mathrm{m} \simeq 0.1\,\mathrm{s}^{-1}$, $\hat{\pi}_\mathrm{m} \simeq 0.2\,\mathrm{s}^{-1}$ and the probability $w_\mathrm{k} \simeq 0.95$.

In the following, we like to discuss two interesting facts of the values determined above. First, the observation that the binding time of single kinesin $\langle \Delta t_\mathrm{k} \rangle$ is numerically equal to the time of a stepping event suggests that kinesin unbinding is not affected by the presence of myosin V. Second, the binding rates $\hat{\pi}_\mathrm{k}$, for kinesin, and $\hat{\pi}_\mathrm{m}$, for myosin V, are numerically the same. It is important to emphasize here, that these rates are associated with the binding process, when the cargo is bound by the other motor not with the binding process of a freely diffusive cargo to the filament. Our study suggests that the probability w_k for a free cargo

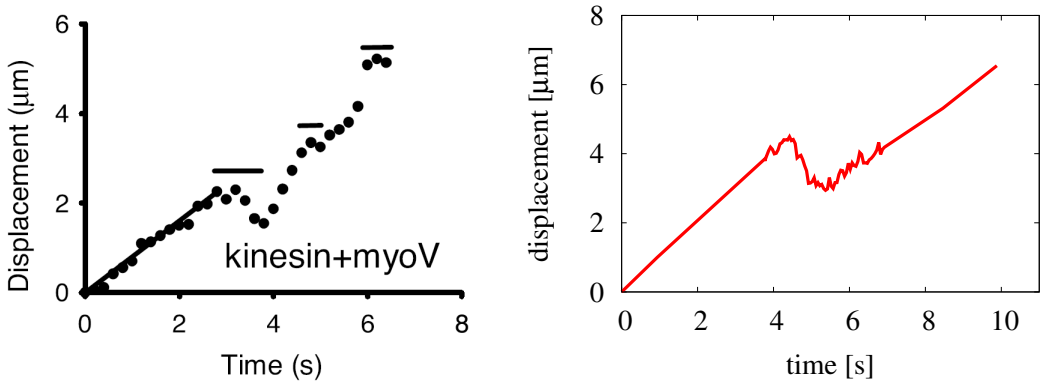

(a) (b)

Figure 4.5 Trajectory of a cargo transported by one myosin V and one kinesin. (a) Experimental trajectory taken from [29]. (b) Simulated trajectory with parameters as in table 4.2.

to initially bind to the microtubule via a kinesin is 0.95. If we introduce an initial binding rate π_k and π_m for kinesin and myosin V, respectively when the other motor is not bound, we obtain from $w_\mathrm{k} = \pi_\mathrm{k}/(\pi_\mathrm{k} + \pi_\mathrm{m}) \simeq 0.95$ the ratio $\pi_\mathrm{k}/\pi_\mathrm{m} \simeq 19$. In contrast, this ratio is reduced when the cargo is bound by the other motor, $\hat{\pi}_\mathrm{k}/\hat{\pi}_\mathrm{m} \simeq 1$. Since the molecular details for the binding of myosin V to the microtubule is not know, we can only speculate about the reduction of the ratio of the binding rates. Using the literature value for kinesin's binding rate $\pi_\mathrm{k} \simeq 5\,\mathrm{s}^{-1}$ [24, 90], we deduce from $\pi_\mathrm{k}/\pi_\mathrm{m} \simeq 19$ that $\pi_\mathrm{m} \simeq 0.26\,\mathrm{s}^{-1}$ which is about the same value as $\hat{\pi}_\mathrm{m}$. This suggests, that myosin V's binding rate is not affected by the presence of kinesin, whereas kinesin's binding rate is strongly reduced, when the cargo diffuses along the filament by the myosin V tether.

4.5. Comparison between theory and experiment

We have now determined all parameters needed in our description by using a subset of the experimental data of [29]. Next, we test our description by comparing it to additional data measured in the experiment [29]. In order to do so, we simulate the system depicted in fig. 4.2 with the rates of table 4.2 using Gillespie's algorithm [144]. With this algorithm the dwell time in each state is drawn from an exponential distribution. Once the dwell time is determined, we determine the position of the cargo over this time window according to the dynamics of the state. In state $(0, 1)$, the cargo performs a discrete time continuous space random walk with the diffusion constant D_m of myosin V. In states $(1, 0)$ and $(1, 1)$, the cargo moves deterministically with a velocity chosen according to a Gaussian distribution with average value $v_\mathrm{k} \simeq 0.88\,\mu\mathrm{m/s}$ and standard deviation $0.2\,\mu\mathrm{m/s}$, as determined experimentally in [29]. A sample trajectory of our simulation is shown in fig. 4.5(b); it

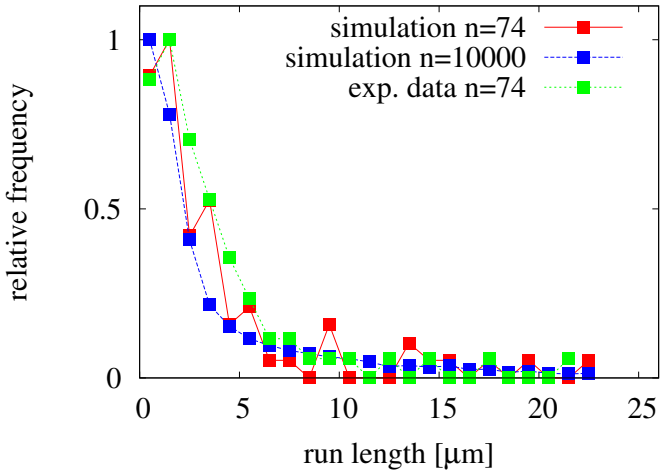

Figure 4.6 Run length distribution of a cargo transported by one kinesin and one myosin V on microtubule. Simulated run length distribution from the network description shown in fig. 4.2 with parameters as given in table 4.2. The results of two simulation are shown: (i) with 74 runs as in the experiment and (ii) with 10000 runs. The experimental distribution is taken from [29]. The simulation with $n = 74$ mimics qualitatively the limited statistics of the experiment.

exhibits alternating sequences of diffusive and stepping events and is remarkably similar to the experimental trajectories, shown in fig. 4.5(a).

First, these simulations reproduce the experimental values that we used to determine the model parameters, namely the run length $\langle \Delta x_{\mathrm{ca}} \rangle \simeq 3.7\,\mu\mathrm{m}$, the stepping time $\langle \Delta t_{\mathrm{se}} \rangle \simeq 1.93\,\mathrm{s}$, the fraction of runs without diffusive events $\phi_{\mathrm{nde}} \simeq 0.72$, the cargo average velocity $\langle v \rangle_{\mathrm{ca}} \simeq (0.73 \pm 0.3)\,\mu\mathrm{m/s}$ and the diffusive time $\langle \Delta t_{\mathrm{de}} \rangle \simeq 4.5\,\mathrm{s}$ in agreement with eqs. (4.7), (4.12), (4.16), (4.17) and (4.28). Second, we find (i) that the average length of runs which exhibit at least one diffusive event is $9.83\,\mu\mathrm{m}$, which is comparable to the experimental value of $7.1 \pm 1.7\,\mu\mathrm{m}$, and (ii) that the average velocities of runs with diffusive events in the simulation are $0.36\,\mu\mathrm{m/s}$, which is comparable to the experimental results $0.55 \pm 0.15\,\mu\mathrm{m/s}$. In fig. 4.6 and fig. 4.7 we compare the run length and velocity distribution from the simulations with the experimental data. We show the results of a simulation with 10000 runs, for a good convergence, and additional of a simulation with only 74 runs to illustrate a possible effect of the limited statistics of the experimental data.

There is a clear difference between the run length distribution from the simulations and the experimentally obtained run length distribution in the region $\langle \Delta x_{\mathrm{ca}} \rangle < 5\,\mu\mathrm{m}$, see fig. 4.6. This discrepancy could result from the fact that only a limited number of trajectories, namely 74, were recorded in the experiment. To get an idea how strongly the run lengths vary between single realizations, we calculate its standard deviation. From the Fourier-Laplace transform of probability current $\hat{J}(k, \lambda)$ into the absorbing state, we obtain the

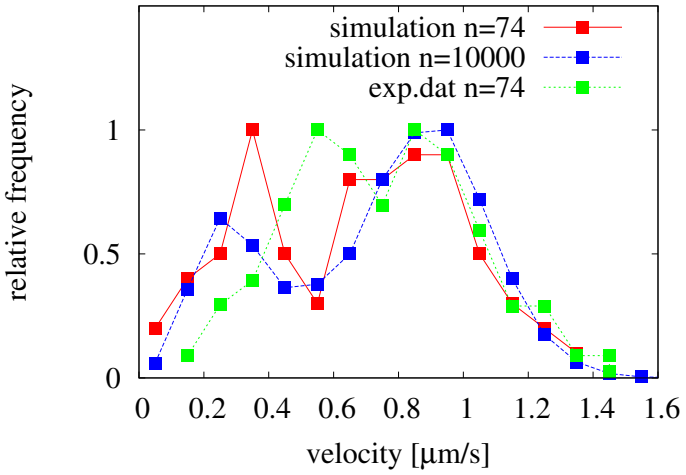

Figure 4.7 Velocity distribution of a cargo transported by one kinesin and one myosin V on microtubule. Simulated velocity distribution from the network description shown in fig. 4.2 with parameters given in table 4.2. The results of two simulation are shown: (i) with 74 runs as in the experiment and (ii) with 10000 runs. The experimental distribution is taken from [29]. The simulation with 74 runs mimics qualitatively the limited statistics of the experiment.

mean square run length as

$$\langle \Delta x_{\mathrm{ca}}^2 \rangle = \int_{-\infty}^{+\infty} \int_{0}^{+\infty} x^2 \, J(x,t) \, dt \, dx = -\partial_k^2 \hat{J}(k,0)|_{k=0}. \tag{4.29}$$

Using this equation together with eq. (4.7) and the values given in table 4.2, we find the standard deviation

$$\sigma(\langle \Delta x_{\mathrm{ca}} \rangle) = \sqrt{\langle \Delta x_{\mathrm{ca}}^2 \rangle - \langle \Delta x_{\mathrm{ca}} \rangle^2} \simeq 6.1 \mu\mathrm{m}. \tag{4.30}$$

This rather large standard deviation indicates a large variance in the run length. Therefore, we suspect that the 74 trajectories evaluated experimentally are not enough to obtain the probability distribution for the steady state. As an illustration of the fluctuation, we simulate only 74 trajectories and calculate a probability distribution for the run length, see fig. 4.6.

We expect the velocity distribution to consist of two overlapping Gaussian distributions, since there are two types of trajectories with different velocities realized in our system. Trajectories with diffusive events have lower average velocities compared to trajectories without diffusive events. The distribution from our simulations shows two peaks at around $0.2\,\mu$m/s and $0.9\,\mu$m/s, see fig. 4.7. The ratio of the two areas under these two Gaussian peaks should be the same as the ratio of the number of trajectories with diffusive events and the number of trajectories without diffusive events; this ratio is $\simeq 0.28$, see table 4.1. This

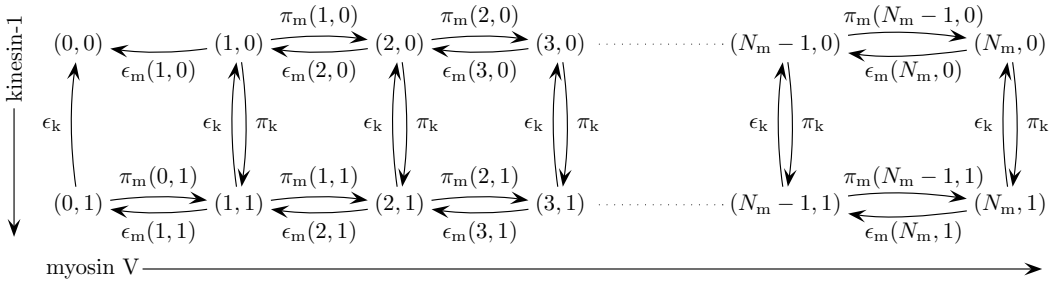

Figure 4.8 Generalized state space of a cargo transported by one kinesin and N_m myosins. Transitions between the states are associated with effective binding and unbinding rates. The rates π_k and ϵ_k are the binding and unbinding rates for kinesin and π_m and ϵ_m are the binding and unbinding rates for the myosin V motors.

crosscheck is somehow not apparent in the distribution of the experimental data. There, both areas under the two peaks are almost equal. It could be possible that the limited statistics with only 74 trajectories are not good enough as argued above. We use our simulations to obtain the standard deviation

$$\sigma(\langle v\rangle_\mathrm{ca}) = \sqrt{\langle v^2\rangle_\mathrm{ca} - \langle v\rangle_\mathrm{ca}^2} \simeq 0.31\mu\mathrm{m/s}, \tag{4.31}$$

which is almost 50% of the average value. To illustrate the spread in the data from a simulation with only 74 realizations, we show a distribution obtained from such a simulation in fig. 4.7.

In summary, concerning the run length and velocity distribution, we found a qualitative agreement between the experimental data and the results from our stochastic description. The discrepancy might be caused by the large variance of these quantities.

4.6. Generalization to several molecular motors

4.6.1. One kinesin motor and several myosin V motors

Before generalizing our model to the case of cargo transport by N_k kinesins and N_m myosins, we study cargo transport with one kinesin and several passive myosins. For this reason we extend the network in fig. 4.2 to the network shown in fig. 4.8. In this network, the unbinding and binding rates for a single myosin V in the cargo state $(n_\mathrm{m}, n_\mathrm{k})$ with n_m bound myosins and n_k bound kinesins are denoted as $\epsilon_\mathrm{m}(n_\mathrm{m}, n_\mathrm{k})$ and $\pi_\mathrm{m}(n_\mathrm{m}, n_\mathrm{k})$, respectively.

As we have seen before, the kinesin unbinding rate is not influenced by the presence of a single myosin V, i.e., $\hat{\epsilon}_\mathrm{k} = \epsilon_\mathrm{k}$. This equality reflects the very low friction of myosin V motion on the microtubule, leading to frictional forces of the order of 0.02 pN, as in eq. (4.2). Comparing this value to the kinesin stall force of about 6-7 pN, see table 2.1, we conclude that the kinesin unbinding rate remains equal to ϵ_k even if several myosins are bound.

Since an unbound motor is under no force, we take the binding rate of a single motor to be equal to its single motor binding rate, as discussed in [30]. This assumption implies that

the binding rate of kinesin is $\pi_k \equiv \hat{\pi}_k$, independent of the number of bound myosins, and that the rate for binding of one of the $(N_m - n_m)$ unbound myosins in state (n_m, n_k) is

$$\pi_m(n_m, n_k) \equiv (N_m - n_m)\pi_m, \tag{4.32}$$

with $\pi_m \equiv \hat{\pi}_m$. Likewise, the unbinding rate of one of the n_m bound myosin V in state $(n_m, 0)$ without bound kinesin is

$$\epsilon_m(n_m, 0) = n_m \epsilon_m. \tag{4.33}$$

We deduced from our stochastic description that the unbinding rate of myosin V changes from the single motor unbinding rate ϵ_m to $\hat{\epsilon}_m > \epsilon_m$ when it is dragged along the microtubule by kinesin, see table 4.2. We will now present two possible mechanisms for this effect, which lead to different unbinding rates $\epsilon_m(n_m, n_k)$ of a single bound myosin V in the cargo state (n_m, n_k). Because of the small frictional force in eq. (4.2), this enhanced unbinding is not caused by strain forces between the motors as it is the case of two actively pulling motors discussed in chapter 3.

Spring model versus free energy model for cooperativity

In the first scenario, *the free energy model*, we assume that the myosin V's motion along the microtubule can be described as diffusion on a rough free energy landscape formed by the microtubule. When myosin V is pulled along this landscape by kinesin, it is more likely to be dragged over free energy hills that it would not have passed when moving freely, which lowers its average free binding energy by ΔG. Using Kramer's theory [81,85], the unbinding rate of one bound myosin V pulled along by one kinesin is

$$\epsilon_m(1, 1) = \epsilon_m \exp[\Delta G / k_B T]. \tag{4.34}$$

With the rate $\epsilon_m(1, 1) = \hat{\epsilon}_m \simeq 0.1\,s^{-1}$ and $\epsilon_m \simeq 0.02\,s^{-1}$ from table 4.2, we find the exponential factor $\exp[\Delta G / k_B T] \simeq 5$.[1] If we now assume that the myosins do not influence each other, the unbinding rate of one of the n_m bound myosins in the cargo state $(n_m, 1)$ is

$$\epsilon_m(n_m, 1) = n_m \epsilon_m \exp[\Delta G / k_B T]. \tag{4.35}$$

In the second scenario, the *the spring model*, we treat the motion of a myosin V head pulled along by kinesin as diffusion in a moving potential generated by the walking kinesin. Since myosin V and kinesin head are connected via the two motor linkers and a rigid cargo, we can approximate this potential by a harmonic spring potential with spring constant κ_{tot}. Because the two motor linkers are in series, we have

$$\kappa_{tot}^{-1} \equiv \kappa_m^{-1} + \kappa_k^{-1}, \tag{4.36}$$

[1] For a high precision, we used in the simulations the numerical value $\hat{\epsilon}_m \simeq 0.104\,s^{-1}$, leading to $\exp[\Delta G / k_B T] \simeq 5.2$.

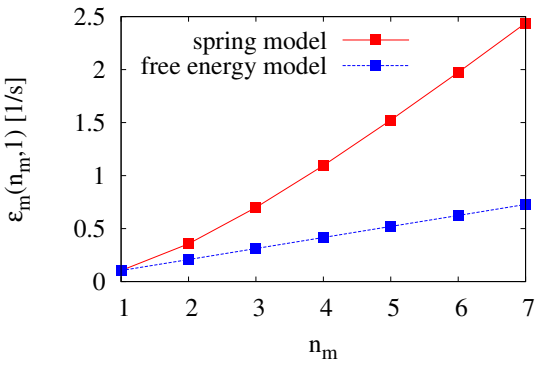

Figure 4.9 Unbinding rate ϵ_m for myosin V in the presence of one kinesin as a function of the number n_m of bound myosins. Here we compare two different models: myosin V's binding energy to the microtubule is reduced because kinesin pulls myosin V 'up the hills' on the ragged free energy landscape (free energy model), see eq. (4.35). In the second model, kinesin generates a moving potential for myosin V, which pulls myosin V along and off the filament (spring model), see eq. (4.40).

where κ_m and κ_k are the spring constants for myosin V and the kinesin linker, respectively, which are both of the order of 0.3 pN/nm [96, 102, 105]. We can thus consider the motion of the myosin V head as diffusion with friction coefficient γ in a harmonic potential. This motion is reminiscent of the motion of a single motor in an optical trap. This leads to a Gaussian distribution of the spring extension Δx,

$$P(\Delta x) = \sqrt{\frac{\kappa_\mathrm{tot}}{2\pi k_\mathrm{B}T}} \exp\left[-\frac{\kappa_\mathrm{tot}}{k_\mathrm{B}T}\left(\Delta x - \frac{v_\mathrm{k}\gamma}{\kappa_\mathrm{tot}}\right)^2\right], \tag{4.37}$$

with average $\langle\Delta x\rangle = v_\mathrm{k}\gamma/\kappa_\mathrm{tot}$, as enforced by mechanical equilibrium, and variance $\sigma^2(\Delta x) = k_\mathrm{B}T/\kappa_\mathrm{tot}$, as follows from the fluctuation-dissipation theorem [145]. Note, π is the circle number not the binding rate π. Hence, the average force $F = \kappa_\mathrm{tot}\langle\Delta x\rangle \simeq 0.02$ pN exerted onto myosin V is negligible, but the force fluctuations $F = \kappa_\mathrm{tot}\sqrt{\sigma^2(\Delta x)} \simeq 0.8$ pN are comparably large. Note that a force of 0.8 pN is a small force for kinesin with a stall force of 6-7 pN but a large force for myosin V with a stall force of 2 pN on actin, see table 2.1. For a myosin V that feels the force F, the unbinding rate is given by $\epsilon_\mathrm{m}\exp(F/\hat{F}_\mathrm{d,m})$, compare the force-dependent unbinding rate in eq. (2.14). This relation defines a detachment force $\hat{F}_\mathrm{d,m}$ for myosin V on microtubule. Averaging the unbinding rate over the Gaussian force distribution from eq. (4.37), we obtain

$$\begin{aligned}\epsilon_\mathrm{m}(1,1) &= \left\langle \epsilon_\mathrm{m}\exp[F/\hat{F}_\mathrm{d,m}]\right\rangle = \epsilon_\mathrm{m}\left\langle \exp[\kappa_\mathrm{tot}\Delta x/\hat{F}_\mathrm{d,m}]\right\rangle \\ &= \epsilon_\mathrm{m}\exp\left[\frac{\kappa_\mathrm{tot}k_\mathrm{B}T + 2\hat{F}_\mathrm{d,m}\gamma v_\mathrm{k}}{2\hat{F}_\mathrm{d,m}^2}\right]\end{aligned} \tag{4.38}$$

for one myosin V and one kinesin. Using the experimentally determined values for v_k, ϵ_m and $\epsilon_\mathrm{m}(1,1) = \hat{\epsilon}_\mathrm{m}$ as given in table 4.2, $\kappa_\mathrm{tot} \simeq 0.15\,\mathrm{pN/nm}$ (where we used $\kappa_\mathrm{k} = \kappa_\mathrm{m} \simeq 0.3\,\mathrm{pN/nm}$ [96, 102, 105]), and $\gamma = 0.02\,\mathrm{pNs/nm}$ from eq. (4.1), we obtain the detachment force $\hat{F}_\mathrm{d,m} \simeq 0.4\,\mathrm{pN}$ of myosin V on microtubule.

If there are n_m bound myosins pulled along by one kinesin, we can consider the myosins as n_m springs in parallel, such that the effective spring constant of the system becomes

$$\kappa_\mathrm{tot}^{-1}[n_\mathrm{m}] = (n_\mathrm{m}\kappa_\mathrm{m})^{-1} + \kappa_\mathrm{k}^{-1}. \tag{4.39}$$

Hence, the effective unbinding rate of the n_m identical myosins in state $(n_\mathrm{m}, 1)$ reads

$$\epsilon_\mathrm{m}(n_\mathrm{m}, 1) = n_\mathrm{m}\epsilon_\mathrm{m} \exp\left[\frac{\kappa_\mathrm{tot}(n_\mathrm{m})k_\mathrm{B}T + 2\hat{F}_\mathrm{d,m}\gamma v_\mathrm{k}}{2\hat{F}_\mathrm{d,m}^2}\right]. \tag{4.40}$$

In fig. 4.9, we show the unbinding rate of myosin V calculated from the the free energy model eq. (4.35) and the spring model eq. (4.40). Since the exponential factor of eq. (4.40) in the spring model is larger than the factor of the free energy model, the unbinding rate increases more rapidly.

To study the effect of the two models onto the quantities observed experimentally, we consider a cargo transported by one kinesin and up to $N_\mathrm{m} = 7$ myosins with the rates listed in table 4.2, using both models for myosin V unbinding. We simulate such a system that corresponds to the network in fig. 4.8 using Gillespie's algorithm [144]. In fig. 4.10(a), the cargo run length $\langle \Delta x_\mathrm{ca} \rangle$ increases with the number N_m of myosins for both models. Because the unbinding rates of myosin V in the spring model are larger compared to the free energy model, there is a slower increase of the run length as a function of the number of myosins. Both models lead to a dramatic increase of the run lengths: it is of the order of $100\,\mu\mathrm{m}$ for 3 to 4 myosins already, which is very large compared to the single motor run length of a few μm.

The cargo velocity decreases as a function of the number of myosins, see fig. 4.10(b). Whenever the cargo is in a diffusive state, i.e. only bound by myosins, the binding time increases, but its average position remains the same. Therefore the velocity decreases as the number or the duration of diffusive events increases. Interestingly, there is almost no difference in the velocity between the two models, indicating that the ratio of the run length and run time is independent of the details of myosin V unbinding rate.

4.6.2. Several kinesin motors and several myosin V motors

In this section, we extend our analysis to cargo transport by N_m passively diffusing myosins and N_k actively pulling kinesins. It is described by the network shown in fig. 4.11.

Assuming that the kinesins act independently from each other and are not influenced by the myosins, we use the effective binding rate

$$\pi_\mathrm{k}(n_\mathrm{m}, n_\mathrm{k}) \equiv (N_\mathrm{m} - n_\mathrm{m})\pi_\mathrm{k}, \tag{4.41}$$

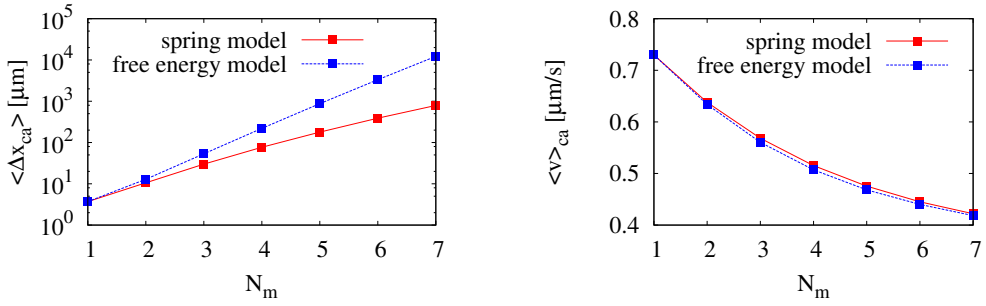

(a) (b)

Figure 4.10 (a) Logarithmic plot of the run length $\langle \Delta x_{\mathrm{ca}} \rangle$ as a function of the number N_{m} of myosins attached to the cargo. The increase is faster in the free energy model compared to the spring model. (b) Average velocity $\langle v \rangle_{\mathrm{ca}}$ of the cargo as a function of the number N_{m} of myosins attached to the cargo. Both models lead to a similar behavior.

the effective unbinding rate

$$\epsilon_{\mathrm{k}}(n_{\mathrm{m}}, n_{\mathrm{k}}) \equiv n_{\mathrm{k}} \epsilon_{\mathrm{k}} \tag{4.42}$$

and the velocity v_{k} for all states where at least one kinesin is bound, for details see [30]. As we learned in chapter 3, in general, elastically coupled motors can influence each other. Here, this simplification of independent motors is a first approximation and can be considered as the case of the weak coupling regime. In other words, we assume that the motors work in the weak coupling regime (I) in fig. 3.9; for example for large detachment forces F_{d}.

For myosin V, we use two sets of rates as specified in the free energy model and in the spring model discussed in the previous subsection and compare the two cases.

In the case of the free energy model, we have assumed that the myosins do not influence each other. Since the cargo velocity is v_{k} as long as at least one kinesin is pulling, we deduce from eq. (4.34) the unbinding rates

$$\epsilon_{\mathrm{m}}(n_{\mathrm{m}}, n_{\mathrm{k}}) = \begin{cases} n_{\mathrm{m}} \epsilon_{\mathrm{m}} & \text{for} \quad n_{\mathrm{k}} = 0 \\ n_{\mathrm{m}} \epsilon_{\mathrm{m}} \exp[\Delta G / k_{\mathrm{B}} T] & \text{for} \quad n_{\mathrm{k}} > 0, \end{cases} \tag{4.43}$$

as shown in fig. 4.12(a). Note that this rate is independent of the number n_{k} of active kinesins for $n_{\mathrm{k}} > 0$. In contrast, in the spring model, we have to take into account that the effective spring constant depends on both the number of active kinesins and the number of active myosins,

$$\kappa_{\mathrm{tot}}^{-1}[n_{\mathrm{m}}, n_{\mathrm{k}}] = (n_{\mathrm{m}} \kappa_{\mathrm{m}})^{-1} + (n_{\mathrm{k}} \kappa_{\mathrm{k}})^{-1}. \tag{4.44}$$

Hence, the unbinding rate defined in eq. (4.40) for the myosin V motors is a function of both numbers of active motors,

$$\epsilon_{\mathrm{m}}(n_{\mathrm{m}}, n_{\mathrm{k}}) = n_{\mathrm{m}} \epsilon_{\mathrm{m}} \exp\left[\frac{\kappa_{\mathrm{tot}}(n_{\mathrm{m}}, n_{\mathrm{k}}) k_{\mathrm{B}} T + 2 \hat{F}_{\mathrm{d,m}} \gamma v_{\mathrm{k}}}{2 \hat{F}_{\mathrm{d,m}}^2} \right], \tag{4.45}$$

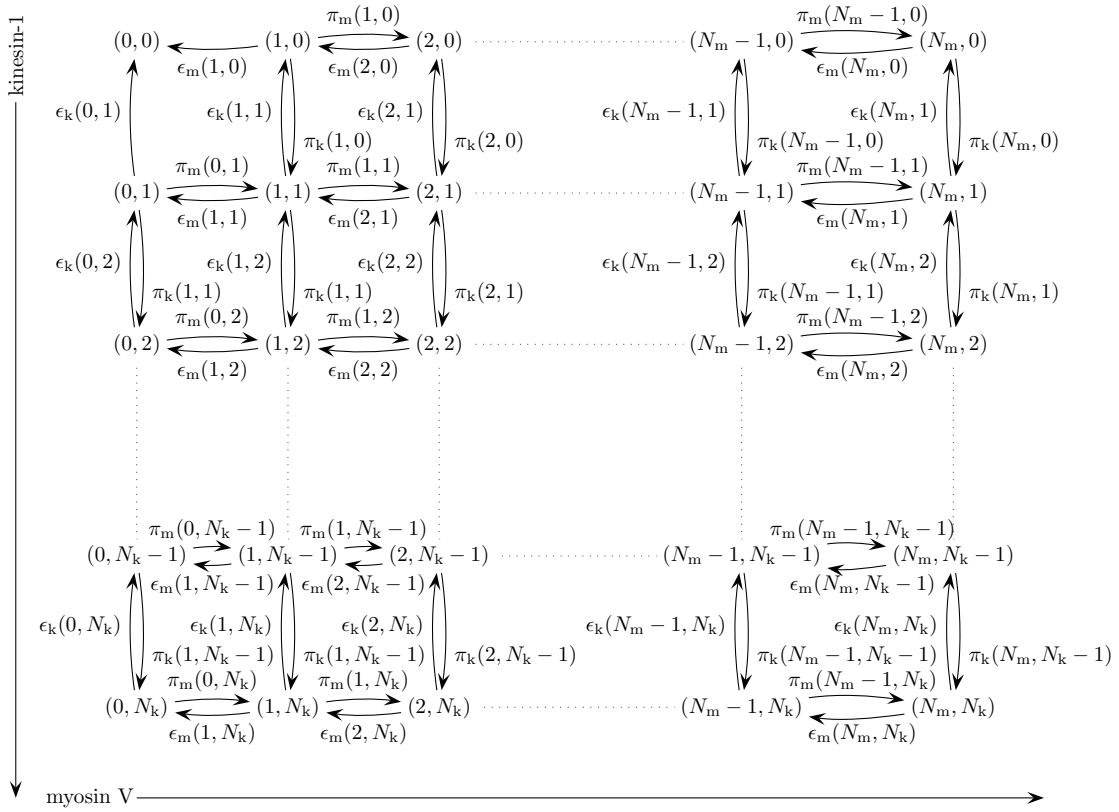

Figure 4.11 Generalized state space of a cargo transported by N_k kinesin and N_m myosins. Kinesin's binding and unbinding rates are denoted by π_k and ϵ_k, respectively and myosin's binding and unbinding rates are denoted by π_m and ϵ_m, respectively.

see fig. 4.12(b). Since κ_tot increases with the number of motors, the unbinding rate increases exponentially with the number of motors. For both models the binding rate for the myosin V motors is defined in eq. (4.32).

With the specified transition rates, and the values from table 4.2 and the previous subsection, we obtain the average cargo run length and velocity from a simulation using a Gillespie's algorithm [144] for the corresponding network shown in fig. 4.11. We determine results for the free energy model and the spring model shown in fig. 4.13. In the free energy model, the run length increases as a function of the motor number. This increase is more rapid with increasing the number of myosins N_m rather than the number of kinesins N_k, see fig. 4.13(a). Having more myosin V on the cargo increases the probability for diffusive events and thus the velocity decreases, see fig. 4.13, while increasing the number of kinesins keeps the cargo velocity constant. For $N_\mathrm{m} = 7$ and $N_\mathrm{k} = 7$, the cargo is transported over large distances with a velocity which almost equals the single kinesin velocity. Using the spring model for calculation of the unbinding rates, we find the same qualitative behavior for both $\langle \Delta x_\mathrm{ca} \rangle$ and $\langle v \rangle_\mathrm{ca}$, see fig. 4.13(c) and fig. 4.13(d), with an overall shorter run length

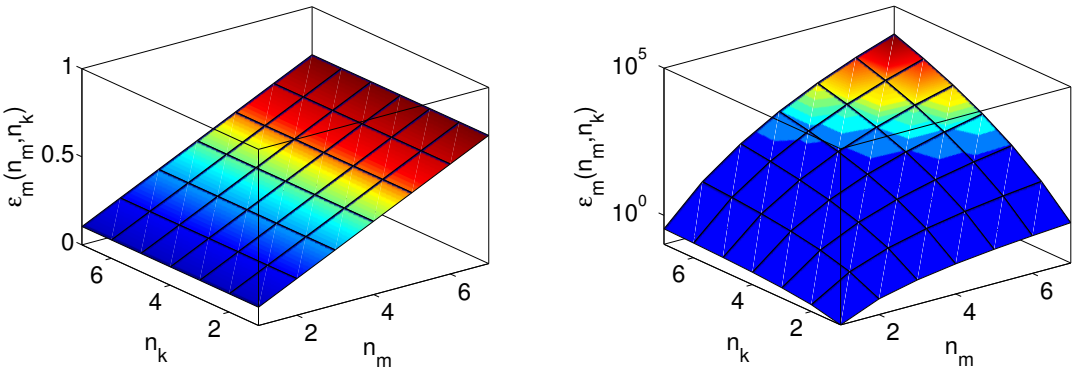

(a) (b)

Figure 4.12 Effective unbinding rates ϵ_m for the myosin V motors as a function of the number n_k of active kinesin and of the number n_m of bound myosin V motors. In both plots, the color code is a guide to the eye to indicate the value of the plotted quantities. (a) Unbinding rates obtained from the free energy model, eq. (4.43). The rates are independent of the number n_k of active kinesins. (b) Logarithmic plot of the unbinding rates obtained from the spring model, eq. (4.45). The rates depend on the number n_k of active kinesins.

compared to the free energy model. This shorter run length is a consequence of the large unbinding rate for the myosin motors in the spring model, see fig. 4.12(b). For $N_\mathrm{m} > 4$, the run length decreases with the number of kinesins due to the dependence of the myosins' unbinding rate on the number of kinesins. Using the spring model, the effective unbinding rate of the myosins increases with the number of active kinesins, see fig. 4.12(b). Therefore, more active kinesins enhance the unbinding of the myosin V motors and thus the probability for diffusive events is reduced. Less diffusive events result in a smaller run length, but a higher velocity.

Although both models lead to a similar behavior, there is an apparent difference in the dependence of the run length on the number of involved motors. Compared to the case of only one actively pulling motor, see fig. 4.10, a cargo transported by several active and passive motors covers large distances with a considerable velocity.

4.7. Summary and discussion

We presented a stochastic theory for cargo transport by simultaneously actively pulling and passively diffusing molecular motors. Our theoretical description is in good agreement with the results of a recent *in vitro* experiment on cargo transport along a microtubule by one active kinesin-1 and one passive myosin V motor [29]. In particular, our theory provides an analytical expression, eq. (4.7), for the observed increase of the cargo's run length, based on the single motor properties. Our study further showed that the kinesin

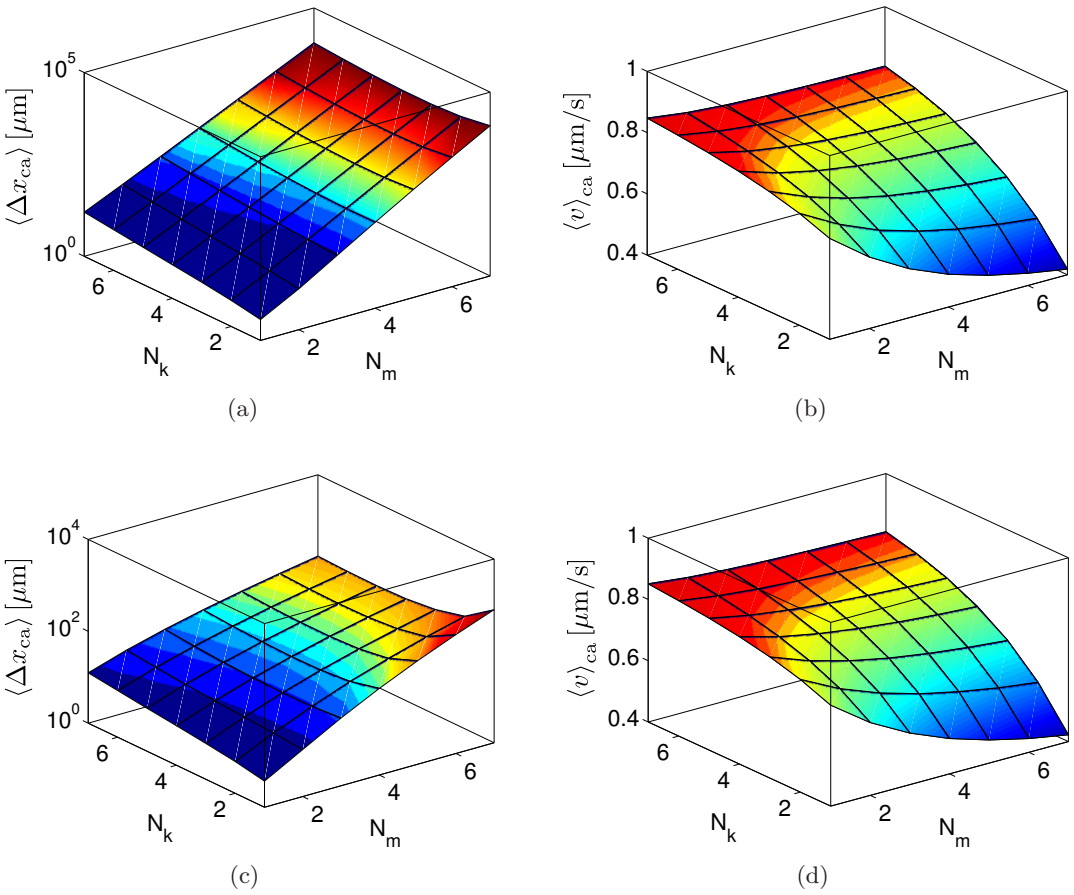

Figure 4.13 Comparison of (a,b) free energy model and (c,d) spring model. In all plots, the color code is a guide to the eye and indicates the value of the quantities shown. (a) Logarithmic plot of the cargo run length $\langle \Delta x_{ca} \rangle$ as a function of the kinesin number N_k and myosin number N_m, as obtained from the free energy model discussed in the text. (b) Average cargo velocity $\langle v \rangle_{ca}$ as a function of the kinesin number N_k and myosin number N_m in the free energy model. (c) Logarithmic plot of the cargo run length $\langle \Delta x_{ca} \rangle$ as a function of the kinesin number N_k and myosin number N_m as obtained from the spring model. The cargo run length increases less steeply in comparison to the free energy model. It attains its maximal value at the boundary with one kinesin and 7 myosins. (b) Average cargo velocity as a function of the kinesin number N_k and myosin number N_m in the spring model.

motion on the filament is not influenced by the presence of myosin V: the velocity of kinesin and its unbinding rate remain unchanged. In contrast, a myosin V that is dragged along by the kinesin exhibits an unbinding rate that is increased by a factor of five. We interpreted the latter observation within two models: In the first model, myosin's binding energy to

the microtubule is reduced because kinesin pulls myosin V 'up the hills' on the ragged free energy landscape experienced by myosin V while diffusing along the microtubule. In the second, kinesin generates a moving potential for myosin V, which pulls myosin V along and off the filament.

A generalization to several myosins based on these two models led to an increase of the run length, resulting in run lengths of tens of μm for already 2 or 3 myosins, see fig. 4.10(a). This large increase is independent of the precise form of the interaction of the myosins and the kinesins and has also previously been found for cargo transport with only actively pulling and no diffusive motors as tethers [30]. Combining several pulling kinesin and passively diffusing myosin V motors, we found that the run length increases more rapidly with the number of passive motors, which in turn slows the cargo down, see fig. 4.13. In order to transport the cargo at a high velocity more pulling kinesins have to be recruited to the cargo.

Although the qualitative behavior fo cargo transport is independent of the two models, quantitatively, they lead to different results. For example, the rate of the increase of the run length was found to depend on the precise model, see fig. 4.10(a) and fig. 4.13. An *in vitro* experiment could therefore be used to decide whether the myosins act as independent tethers, as in the free energy model, or influence each other, as in the spring model.

The fact that the motion of kinesin remains unchanged in the presence of myosin V motors while myosin V reacts strongly to kinesin's presence is consistent with the general observation that kinesin is a robust microtubule motor [14]. Myosin V, a robust motor on actin filaments, is only weakly bound to microtubules compared to kinesin. Therefore, myosin V can easily be influenced by kinesin when moving along microtubules. This feature is certainly useful for intracellular transport: the passive motor can be dragged along without effort which prevents hindrance of the pulling motor.

Our theory describes the case of kinesin as the pulling motor and myosin V as the diffusive tether. For this scenario, a sufficient amount of data is available to determine all rates used in our description. In [29], enhanced cargo transport on actin has been observed, where myosin V is the actively pulling motor and kinesin is the passively diffusing tether. Due to an insufficient amount of data, it is not possible, at present, to find all rates for the corresponding network description. However, a study discussing parameter spaces can be found in [146].

Finally, it is tempting to speculate that having kinesin and myosin V attached to the same cargo is advantageous, as the cargo is able to switch between actin to microtubule tracks and even has an increased run length on microtubule. Whether this type of motor cooperation is realized under physiological conditions, is however still an open question [147].

5. Concluding remarks

5.1. Summary

Cargo transport by the cooperative action of molecular motors is ubiquitous in all eukaryotic cells. In this thesis, we focused on two generic transport modes: unidirectional transport by two identical motors and transport on different filaments by actively pulling and passively diffusing motors, both studied by recent *in vitro* experiments.

Our theory was based on a reduced single motor description as introduced in section 2.2. We described the fundamental stochastic motor dynamics of stepping along, binding to, and unbinding from the filament with force-dependent rates. The parameters for such a description were deduced from single motor experiments as explained in section 2.2.2. To study a cargo transported by several molecular motors, we introduced a discrete state space associated with the single motor dynamics, see fig. 3.2(b) and fig. 4.2. Then, we considered a continues-time Markov process on the state space. We have developed a generalization of Hill's method for the average absorption time, which allowed us to calculate averaged quantities for arbitrary initial conditions, see section 2.3.3. After establishing this generalized method, we addressed cargo transport by two elastically coupled identical motors in chapter 3 and cargo transport by active and passive motors in chapter 4.

Two identical motors, elastically coupled via the cargo, exhibit four distinct regimes of transport, see fig. 3.9. In the *weak coupling* regime, both the binding time and the velocity are hardly effected by the coupling. In contrast, both quantities are reduced in the *strong coupling* regime. In addition to these two regimes that one may expect naively, there are two further transport regimes: a *reduced velocity* regime, in which the motors slow each other down without influencing the binding time and an *enhanced unbinding* regime, in which motors pull each other from the filament without reducing their velocity. The occurrence of these regimes depends on the coupling strength and on the parameters of the dynamics of the single motors. This complex interplay of force-dependent stepping, strain force generation and force-dependent unbinding can be understood by comparing three different time scales: (i) the time for spontaneous unbinding, (ii) the time for developing a strain force between the motors that is comparable to the detachment force and (iii) the time it takes to generate a strain force comparable to the stall force. These time scale arguments provide not only a quantitative but also an intuitive understanding of the cooperative behavior.

Our theoretical results are fully consistent with the available experimental data for two coupled kinesin-1 motors from the Diehl lab. We have found a set of parameters for the single motor description, which leads to very good agreement between theory and experiment, see table 3.5. Beyond explaining these experimental findings, we make novel predictions for different motor types. We predicted that different subsets of the transport regimes should

be observed for different motor types when their elastic coupling strength is varied. In this way, pairs of kinesins or dyneins exhibit the weak coupling regime, strong coupling regime and enhanced unbinding regime, whereas myosin motors attain a reduced velocity regime and the weak coupling regime, see fig. 3.10. These findings should be directly accessible to experiments using complexes of two coupled motors that can be synthesized by recently established methods [25].

The rather general framework together with the time scale arguments allowed us to study the dynamics of the motor pair for more detailed description of the single motor properties. To name a few, we discussed different force-velocity relations including backward steps, the [ATP] dependence of the strain force generation, and non-linear springs as motor-cargo linkers. In this way, we could clarify why previous studies based on different single motor descriptions came to different conclusions about the influence of motor-motor interference.

Our study provides a detailed description of the state, in which both motors are active. However, the whole trajectory of a cargo transported by two motors also contains segments in which only one motor is actively pulling the cargo. Our results can be integrated into the general framework for describing the dynamics of cargo transport by several motors [30]. Inspection of the binding time and the mean velocity of the overall cargo run reveals again the four distinct transport regimes, see fig. 3.26.

The other cooperative transport mode considered in this thesis was transport by actively pulling and passively diffusing motors in chapter 4. We presented a stochastic description for the transport of a single cargo by actively pulling and passively tethering motors. We applied this general model to the case of transport by one myosin V and one kinesin-1 along a microtubule, as investigated in the *in vitro* experiment in [29]. We deduced all rates for the description from a subset of the experimental data, and then used our model to describe all experimentally measured quantities, finding good agreement. Such a cargo exhibits fast directed motion interrupted by diffusive events. The overall run length of this cargo particle is more than twice that of a cargo transported by a single kinesin. We derived an analytical expression, eq. (4.7), for the enhanced run length of the cargo in terms of single motor parameters. Furthermore, our results suggested that the actively pulling kinesin motion is not influenced by the passive presence of myosin V. We also investigated the effect of several myosins on a cargo pulled by a single kinesin, which led to an exponential increase of the cargo's run length, see fig. 4.10(a). Finally, we addressed the case of several active kinesins and several passive myosins transporting the same cargo. In this case, the cargo's run length also increases exponentially with the number of motors, but the effect on the velocity is different depending on which motor number is increased: more passive motors slow the cargo down, whereas more active motors keeps the mean velocity of the cargo constant, see fig. 4.13.

In summary, we presented a theoretical approach that integrates the well-established properties of individual motors into a predictive theory for cooperative transport. In this way, it relates the behavior on the cargo level to the behavior of the individual motors working collectively. The comparison of quantitative theoretical predictions and experiments can then provide insights into mechanistic details that are not directly accessible in experiments. Until now, little is known experimentally about the detailed behaviors of individual motors

during collective transport, but our theory provides a general framework to address such problems and it suggests how to analyze data. For example, in the case of unidirectional transport, we predict different transport regimes depending on the single motor parameters that can be compared to new experimental data. In this way, our theory contributes to a quantitative understanding of cargo transport by several molecular motors.

5.2. Outlook

We presented a general theory of cooperative cargo transport based on a reduced single motor description. As soon as more experimental data for single motors are available and methods to couple motors in a defined way, our theory can be extended to make additional quantitative predictions. In the case of two coupled identical motors, our description can be extended to systematically study cargo transport by two motors with different single motor properties. A particular scenario is the cooperative action of slow and fast motors, in which the slow motor exerts drag on the fast motor and vice versa [148, 149]. Another example provides a very recent *in vitro* experiment [101], in which the stepping patterns of a tug-of-war between myosin V and myosin VI has been studied. Moreover, in our study, we didn't consider external forces, which is an interesting perspective, recently addressed experimentally [26], as well as theoretically [42, 43, 150]. We expect that the time scale arguments developed in this thesis will again be applicable, but further, more systematic studies are needed in order to reach definite conclusions.

With respect to transport by active and passive molecular motors, a recent *in vitro* experiment [59] found a nonprocessive actin motor Myo2p to be able to transport a cargo processively in the presence of a kinesin-related protein called Smy1p on the same cargo. In this case, Smy1p acts as a tether to enable the nonprocessive motor to transport cargo processively. Such a transport process can be understood by an appropriate adaptation of our theory.

In order to develop a systematic understanding of cooperative transport properties, it is important to study biomimetic model systems. It is necessary to reveal the relation between the single motor behavior and the transport properties involving several different motors. It is most likely that it will be possible to couple different motors in different defined ways within the next couple of years. Such a bottom-up approach together with a theoretical framework will lead to a comprehensive understanding of cooperative cargo transport. Such understanding may also be useful for the pathology of transport related diseases [151], as well as for constructing nanotechnological devices integrating molecular motors [152, 153]. The latter machines will work collectively in a lab on a chip and as carriers for specific drug delivery within organisms [154]. It is rather likely that the further development of such nano-bio applications will provide many fundamental and challenging questions about the complexity and diversity of cooperative cargo transport by molecular motors.

A. Appendix

A.1. Properties of the overall cargo run: distribution of binding time and run length

The state space of a cargo transported by two motors is shown in fig. 3.1. The distribution of the binding time is given from the time dependent solution of the master equation for such a network. This distribution of the binding time has been derived in a previous study of cargo transport by several motors [30] and reads

$$P(\Delta t_{\mathrm{ca}}) = \frac{\epsilon_1}{2}\Bigg[\left(1-\frac{\epsilon_1+\pi-\epsilon_2}{\sqrt{(\epsilon_1+\epsilon_2+\pi)^2-4\epsilon_1\epsilon_2}}\right)e^{-\frac{1}{2}\Delta t_{\mathrm{ca}}(\epsilon_1+\epsilon_2+\pi-\sqrt{(\epsilon_1+\epsilon_2+\pi)^2-4\epsilon_1\epsilon_2})} + \left(1+\frac{\epsilon_1+\pi-\epsilon_2}{\sqrt{(\epsilon_1+\epsilon_2+\pi)^2-4\epsilon_1\epsilon_2}}\right)e^{-\frac{1}{2}\Delta t_{\mathrm{ca}}(\epsilon_1+\epsilon_2+\pi+\sqrt{(\epsilon_1+\epsilon_2+\pi)^2-4\epsilon_1\epsilon_2})}\Bigg]. \quad \text{(A.1)}$$

The distribution of the run length of the cargo is obtained from the distribution of binding times eq. (A.1) by expressing the rates in units of the inverse distances rather than in units of inverse times, i.e., by substituting $\langle\Delta t_{\mathrm{ca}}\rangle$ by $\langle\Delta x_{\mathrm{ca}}\rangle$ and ϵ_i by ϵ_i/v_i and π by π/v_1, leading to

$$P(\Delta x_{\mathrm{ca}}) = \frac{\epsilon_1}{2v_1}\Bigg[\left(1-\frac{\frac{\epsilon_1}{v_1}+\frac{\pi}{v_1}-\frac{\epsilon_2}{v_2}}{\sqrt{(\frac{\epsilon_1}{v_1}+\frac{\epsilon_2}{v_2}+\frac{\pi}{v_1})^2-4\frac{\epsilon_1}{v_1}\frac{\epsilon_2}{v_2}}}\right)e^{-\frac{1}{2}\Delta x_{\mathrm{ca}}(\frac{\epsilon_1}{v_1}+\frac{\epsilon_2}{v_2}+\frac{\pi}{v_1}-\sqrt{(\frac{\epsilon_1}{v_1}+\frac{\epsilon_2}{v_2}+\frac{\pi}{v_1})^2-4\frac{\epsilon_1}{v_1}\frac{\epsilon_2}{v_2}})} + \left(1+\frac{\frac{\epsilon_1}{v_1}+\frac{\pi}{v_1}-\frac{\epsilon_2}{v_2}}{\sqrt{(\frac{\epsilon_1}{v_1}+\frac{\epsilon_2}{v_2}+\frac{\pi}{v_1})^2-4\frac{\epsilon_1}{v_1}\frac{\epsilon_2}{v_2}}}\right)e^{-\frac{1}{2}\Delta x_{\mathrm{ca}}(\frac{\epsilon_1}{v_1}+\frac{\epsilon_2}{v_2}+\frac{\pi}{v_1}+\sqrt{(\frac{\epsilon_1}{v_1}+\frac{\epsilon_2}{v_2}+\frac{\pi}{v_1})^2-4\frac{\epsilon_1}{v_1}\frac{\epsilon_2}{v_2}})}\Bigg]. \quad \text{(A.2)}$$

Note, in the force-free case, $v_1 = v$ and $\epsilon_1 = \epsilon$.

A.2. Iterative solution of master equations

In this section, we solve the master equation for the reduced motor description of section 3.2.1 by using a backward substitution. The steady state master equation describing the dynamics on the network shown in fig. 3.4 is given by

$$0 = \omega_{\mathrm{r}}(1)P_1 - \omega_{\mathrm{s}}(0)P_0 + \sum_{j=1}^{N}\omega_{\mathrm{off}}(j)P_j, \quad \text{(A.3)}$$

for $0 < i < N$,

$$0 = \omega_{\mathrm{s}}(i-1)P_{i-1} + \omega_{\mathrm{r}}(i+1)P_{i+1} - \omega_{\mathrm{r}}(i)P_i - \omega_{\mathrm{s}}(i)P_i - \omega_{\mathrm{off}}(i)P_i \tag{A.4}$$

and

$$0 = \omega_{\mathrm{s}}(N-1)P_{N-1} - \omega_{\mathrm{r}}(N)P_N - \omega_{\mathrm{off}}(N)P_N. \tag{A.5}$$

Now, we use a backward substitution to obtain from eq. (A.5),

$$P_{N-1} = \frac{\omega_{\mathrm{r}}(N) + \omega_{\mathrm{off}}(N)}{\omega_{\mathrm{s}}(N-1)} P_N, \tag{A.6}$$

and from eq. (A.4)

$$P_{i-1} = \frac{\omega_{\mathrm{r}}(i) + \omega_{\mathrm{s}}(i) + \omega_{\mathrm{off}}(i)}{\omega_{\mathrm{s}}(i-1)} P_i - \frac{\omega_{\mathrm{r}}(i+1)}{\omega_{\mathrm{s}}(i-1)} P_{i+1}, \tag{A.7}$$

where the index i runs backwards from $i = N-1$ to $i = 1$. In this way, for $i < N$, we obtain all P_i as a function of P_N. Either from eq. (A.3) or from the normalization,

$$\sum_{i=0}^{N} P_i = 1, \tag{A.8}$$

P_N can be obtained and thus all P_i are determined. For a numerical implementation of this backward substitution algorithm it is convenient first to choose an arbitrary value for P_N, obtain all P_i from eq. (A.7) and eq. (A.6) and then renormalize all P_i in such a way that $\sum_i P_i = 1$.

A.3. Detailed discussion of the time scales for strain force generation

In this section, we discuss difficulties that arise from the mapping of continuous variables to discrete values and from our reduced motor description. The crossover line $f_{\mathrm{d}}(f_{\mathrm{s}})$ between the regimes with and without strain-induced unbinding is implicitly given by the equation

$$t_{F_{\mathrm{d}}}(f_{\mathrm{d}}, f_{\mathrm{s}}) = t_{\mathrm{u}}. \tag{A.9}$$

However, for obtaining $t_{F_{\mathrm{d}}}$, we map the continuous variable f_{d} to a discrete variable by using the ceiling function, see eq. (3.35). As an example, we plot $t_{F_{\mathrm{d}}}(f_{\mathrm{d}})$ for $f_{\mathrm{s}} \simeq 6$ and $t_{\mathrm{u}} \simeq 0.5\,\mathrm{s}$ in fig. A.1(a). The intersection point at $f_{\mathrm{d}} = 5$ distinguishes strain-induced unbinding for $f_{\mathrm{d}} < 5$ and spontaneous unbinding for $f_{\mathrm{d}} > 5$. The steps in the function $t_{F_{\mathrm{d}}}(f_{\mathrm{d}})$ arise from the ceiling function in the upper limit of summation in eq. (3.37). Therefore, it can happen that for fixed f_{s} several values of f_{d} satisfy eq. (A.9) leading to steps in the crossover line $f_{\mathrm{d}}(f_{\mathrm{s}})$. The numerical solution [137] of the crossover line exhibits such steps and is displayed as a solid black line in fig. 3.9.

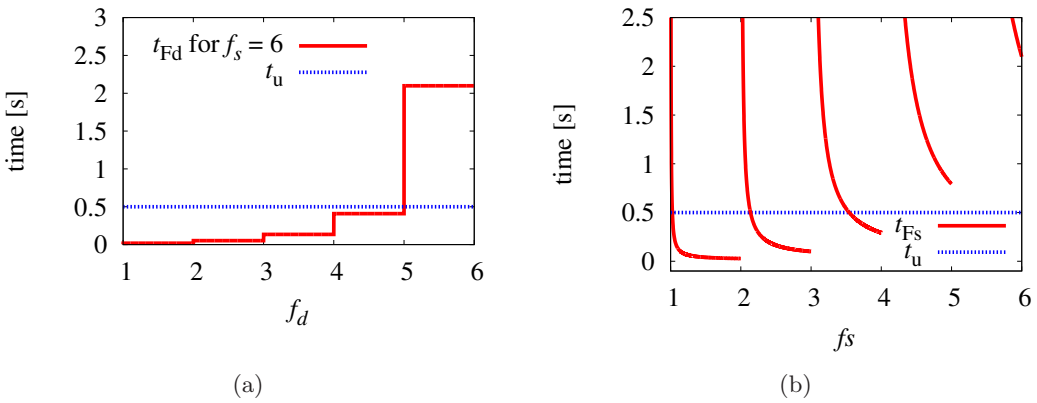

(a) (b)

Figure A.1 (a) The average time t_{F_d} (red line) it takes to generate a force comparable to the detachment force between the two coupled motors as a function of the scaled detachment force f_d for $f_s = 6$. (b) The average time t_{F_s} it takes to generate a force comparable to the stall force between the motors as a function of the scaled stall force f_s (red line). Both times are compared to the characteristic time for spontaneous unbinding t_u (blue broken line). For both plots, the rates and parameters are taken from table 3.2.

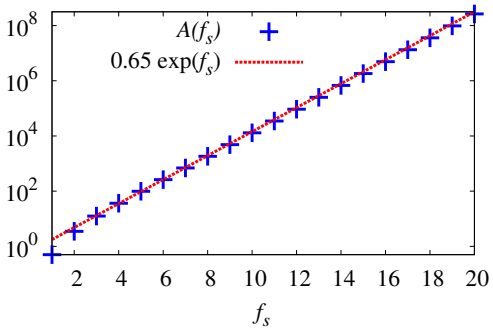

Figure A.2 Logarithmic plot of the sum $A(f_s)$ as given by eq. (3.44) and the numerical approximation $0.65\exp(f_s)$.

To estimate whether there is an interference effect on the velocity or not, we introduce the time scale t_{F_s} in section 3.3.1. The basic idea is the following: as soon as the motors produce a strain force which is comparable to the stall force, the average velocity of the cargo is strongly reduced. This is the case for our standard force-velocity relation in eq. (2.20). If the time t_{F_s} to reach such a force is smaller compared to the time for spontaneous unbinding t_u, the system exhibits a reduced velocity on average. For estimating t_{F_s}, we neglect unbinding and therefore eq. (3.41) is independent of the detachment force and thus t_{F_s} is only a function of f_s. Again, the continuous variable f_s appears in the ceiling function

in the upper limit of summation. In addition, the time $t_{F_s}(f_s)$ displays discontinuities, see fig. A.1(b). This behavior can be understood from the following considerations. For $f_s = 1+\delta$ with $\delta \ll 1$, the upper limit of summation in eq. (3.41) becomes $\lceil f_s \rceil - 1 = 1$ and

$$t_{F_s} = \frac{l}{v}\left[\frac{1}{2} + \frac{1}{2(1-\frac{1}{1+\delta})} + \frac{1}{(1-\frac{1}{1+\delta})}\right]. \tag{A.10}$$

In the denominator, the factor $(1-1/(1+\delta))$ can be arbitrarily small for arbitrarily small δ. As a consequence t_{F_s} is large for small δ. Beside of this rather mathematical explanation, we can also consider our two motor system for a more intuitive understanding. The discontinuity arises for f_s slightly larger than an integer value. As an example, we consider again the case $f_s = 1+\delta$ with $\delta \ll 1$. The state associated with a force larger than or equal to the stall force is then $(\lceil f_s \rceil) = (2)$. However, the transition from state (1) to state (2) is very small, since the the transition is determined by state (1). In this state the associated force is almost stall force, because $f_s \approx 1$. A force comparable to the stall force means that the rate for the next forward step which is the transition to state (2) is very small. For this reason, the time it takes to reach the state (2) is very long. To deal with these issues, we define the crossover line as the smallest integer f_s^* for which $t_{F_s} \geq t_u$. Note, other choice are also possible, but the essential point of our choice is that it ensures that there is on $f_s > f_s^*$ for which $t_{F_s} < t_u$.

Next, we explain the numerical approximation for t_{F_s}. As in eq. (3.44), the time t_{F_s} can be rewritten as

$$t_{F_s} = \frac{l}{v} A(f_s). \tag{A.11}$$

For more convenience, we restrict f_s to integer values and approximate $A(f_s)$ with the function $A(f_s) \approx a_0 \exp(f_s)$. The fit parameter $a_0 \simeq 0.65$ is obtained from a least square fit to the numerical solution of the sum for $f_s \in [1, 6]$.

A.4. Empirical stepping rates based on kinesin-1 experiments

Now, we consider an empirical force-velocity relation obtained from a fit to the kinesin-1 data from [69] including back stepping. In [69], Carter and Cross have measured the force-dependent ratio of forward and backward steps for kinesin-1, which could be approximated with

$$q(F) = q_0^{1-\frac{F}{F_s}}, \tag{A.12}$$

where $q_0 \simeq 800$ independent of the ATP concentration, see fig. A.3(a). Furthermore, they obtained the force-velocity relation for opposing and assisting forces for two different ATP concentrations, see fig. A.3(b). This data can be described by

$$\mathcal{V}(F) = \frac{v_{max}\frac{v_{min}-v}{v-v_{max}} + v_{min}\left(\frac{v_{max}}{v_{min}}\frac{v_{min}-v}{v-v_{max}}\right)^{F/F_s}}{\frac{v_{min}-v}{v-v_{max}} + \left(\frac{v_{max}}{v_{min}}\frac{v_{min}-v}{v-v_{max}}\right)^{F/F_s}}. \tag{A.13}$$

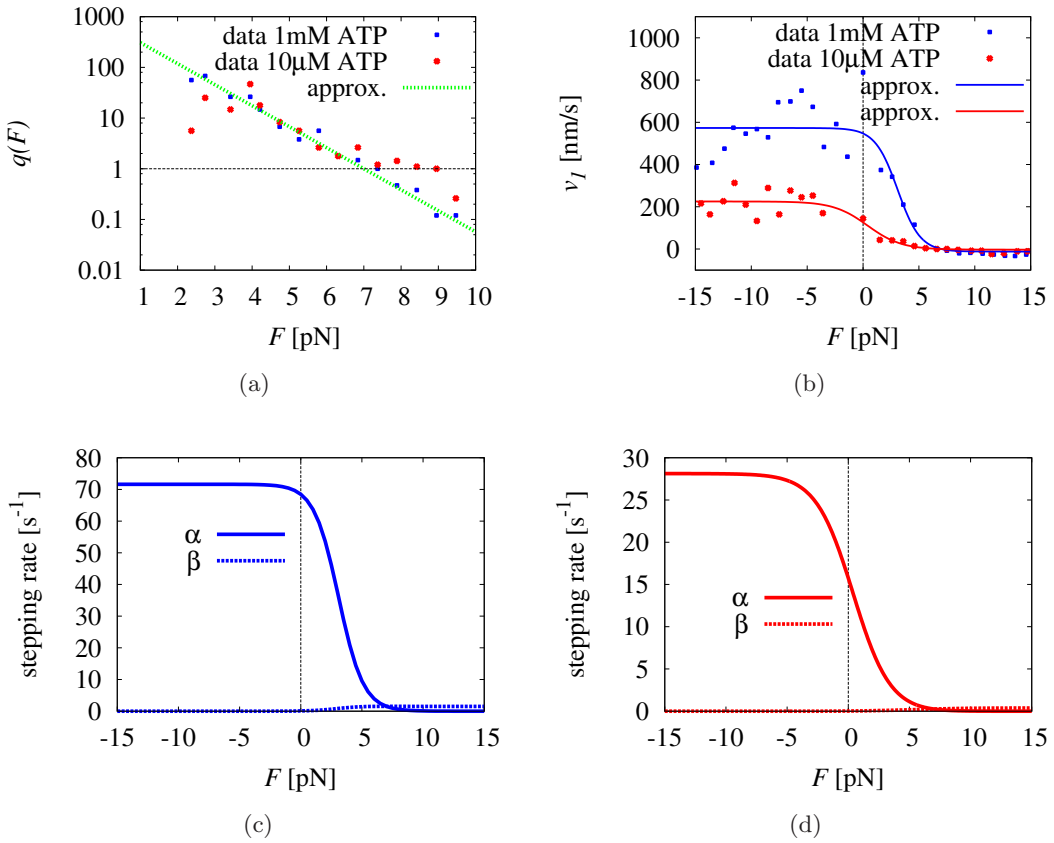

Figure A.3 Experimental data for kinesin-1 stepping taken from [69]. Figures (a) and (b) are the same as fig. 2.5(a) and fig. 2.5(b). (a) Ratio of forward to backward stepping rates $q(F)$ as a function of load force F for different ATP concentrations: 1mM ATP (blue) and 10μM (red). The line in the logarithmic plot is given by eq. (A.12) with $q_0 \simeq 800$ and $F_s \simeq 7\,\mathrm{pN}$ as suggested in [69]. (b) Force-velocity relation for kinesin-1 for different ATP concentrations taken from [69]. The two lines are the force-velocity relations from eq. (A.13) and $F_\mathrm{s} \simeq 7\,\mathrm{pN}$, where we use a least square fit to obtain the parameters $v \simeq 547\,\mathrm{nm/s}$, $v_\mathrm{max} \simeq 573\,\mathrm{nm/s}$ and $v_\mathrm{min} \simeq -12\,\mathrm{nm/s}$ for 1mM ATP (blue) and $v \simeq 126\,\mathrm{nm/s}$, $v_\mathrm{max} \simeq 225\,\mathrm{nm/s}$ and $v_\mathrm{min} \simeq -3\,\mathrm{nm/s}$ for 10μM ATP (red). (c) Forward $\alpha(F)$ and backward $\beta(F)$ stepping rates obtained from (a) and (b) for 1mM ATP concentration and (d) corresponding stepping rates for 10μM ATP concentration.

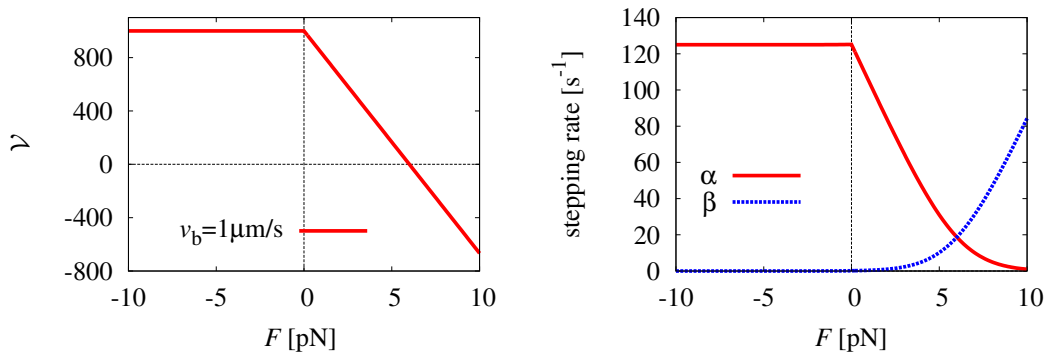

(a) (b)

Figure A.4 (a) Piecewise linear force-velocity relation with backward velocity $v_b \simeq 1\,\mu$m/s, given by eq. (A.14) and (b) the corresponding forward stepping rate α and backward stepping rate β.

Here, we determine the maximal velocity $v_{\max}$, the minimal velocity $v_{\min}$ and the force-free velocity v from a least square fit to the measured data, see blue and red line in fig. A.3(b) and values in the caption. Using the ratio of eq. (A.12) and the force velocity relation of eq. (A.13), we determine the forward and backward stepping rates eq. (2.5) and eq. (2.6) for our network description. The stepping rates are displayed in fig. A.3(c) and in fig. A.3(d).

A.5. Backward stepping

As discussed in section 2.2.2, backward stepping of molecular motors has been revealed in various single molecular experiments. Under stall force, the number of forward steps is equal to the number of backward steps. In this case, the distance between two elastically coupled motors fluctuates, although the cargo is not moving on average. In principle, these fluctuations could enhance unbinding. In the following, we quantify this effect and discuss whether it is significant for the parameters used in our study. To account for backward stepping in our description, we use the stepping rates α and β given by eq. (2.5) and eq. (2.6), the ratio of forward to backward steps, see eq. (A.12), and a force-velocity relation with a backward velocity $v_\mathrm{b} \neq 0$,

$$\mathcal{V}(F) \equiv \begin{cases} v & F < 0 \\ v(1 - F/F_\mathrm{s}) & 0 \leq F < F_\mathrm{s} \\ v_\mathrm{b}(1 - F/F_\mathrm{s}) & F \geq F_\mathrm{s}, \end{cases} \tag{A.14}$$

shown in fig. A.4(a). Inspection of the corresponding force dependent stepping rates $\alpha(F)$ and $\beta(F)$ reveals, that these rates are not defined for $F = F_\mathrm{s}$; they even are discontinuous for $v_1 \neq v_\mathrm{b}$ as shown in the following. From eq. (2.5), the forward stepping rate is defined

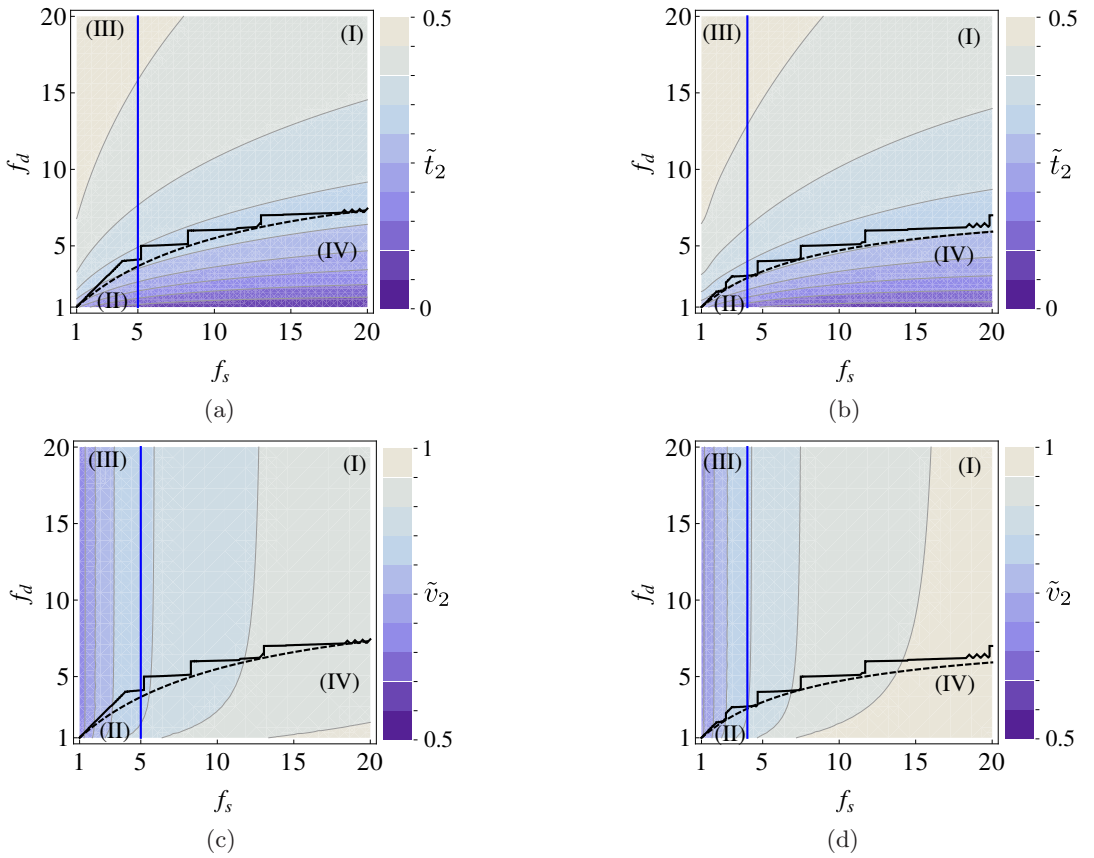

Figure A.5 (a)-(b) Scaled binding time $\tilde{t}_2$ and (c)-(d) scaled velocity $\tilde{v}_2$ as a function of the scaled forces f_s and f_d. The single motors are able to step backwards and their parameters are taken from table 3.2, except for the stepping rates. For (a) and (c), the stepping rates correspond to the piecewise linear force-velocity relation shown in fig. A.4(a). They are shown in fig. A.4(b). The stepping rates fitted to the data by Carter and Cross as shown in fig. A.3(c) are used for the plots (b) and (d). The crossover lines between the transport regimes are obtained as explained in section 3.3.1, but taking backward stepping into account. The solid blue line separates the region with and without a reduced velocity, whereas the solid black line separates the region of spontaneous and force-induced unbinding. The dashed lines correspond to the approximated crossover line as given by eq. (3.38).

as

$$\alpha(F) = \frac{q(F)}{q(F)-1}\frac{\mathcal{V}(F)}{l}, \tag{A.15}$$

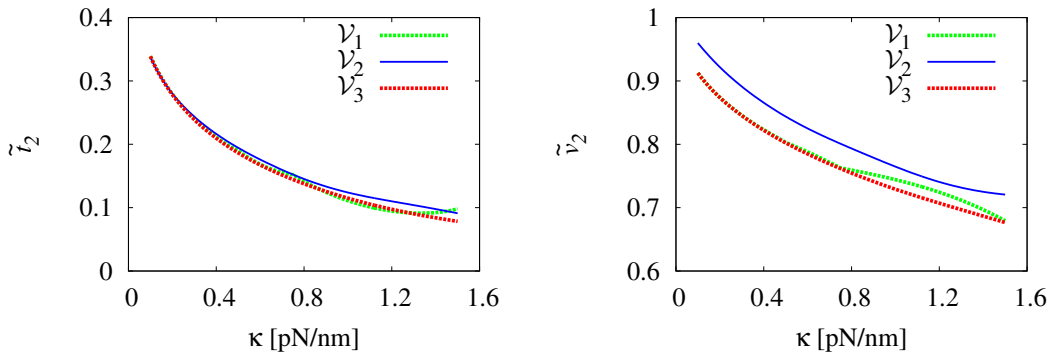

(a) (b)

Figure A.6 Detailed comparison of the effect of backward stepping for different force-velocity relations: $\mathcal{V}_1$ does not include backward stepping and is given by eq. (2.20), $\mathcal{V}_2$ as in eq. (A.13) and $\mathcal{V}_3$ as in eq. (A.14) with $v_\mathrm{b} \simeq 1\,\mu$m/s. $\mathcal{V}_2$ and $\mathcal{V}_3$ include backward stepping. (a) Scaled binding time $\tilde{t}_2$ and (b) velocity $\tilde{v}_2$ for two active kinesins with parameters from table 3.1 and corresponding force-velocity relations as a function of the stiffness κ. All other parameters are for kinesin-1 from table 3.2.

where $q(F) = q_0^{(1-F/F_\mathrm{s})}$ as in eq. (2.19). Using l'Hôpital's rule, we obtain the one-sided limit from below,

$$\lim_{F\to F_\mathrm{s}-} \alpha(F) = \frac{v}{l\ln(q_0)} \tag{A.16}$$

and from above

$$\lim_{F\to F_\mathrm{s}+} \alpha(F) = \frac{v_\mathrm{b}}{l\ln(q_0)}. \tag{A.17}$$

We complete the stepping rate with the average value of the limits, such that

$$\alpha(F_\mathrm{s}) \equiv \frac{1}{2}\left(\lim_{F\to F_\mathrm{s}-} \alpha(F) + \lim_{F\to F_\mathrm{s}+} \alpha(F)\right). \tag{A.18}$$

This results in the stepping rates shown in fig. A.4(b).

In addition to the rather simple linear force-velocity relation given by eq. (A.14), we consider the empirical force velocity relation including backward steps as introduced in section A.4

Let us compare the results from the two velocity relations with backward stepping to the ones from the reduced description without backward stepping, discussed in section 3.3. As a technical remark, we like to note that, in the case of backward stepping, the forces between the motors are not limited any more, since backward stepping could lead to higher forces than stall force. Thus, we have to choose the number of states N, see fig. 3.3, large enough, i.e., such that the results do not depend on N.

Using the scaled forces as variables, we determine the scaled binding time $\tilde{t}_2$ and the scaled velocity $\tilde{v}_2$ for the linear force velocity relation, eq. (A.14), with $v_b = 1\mu$m/s and for

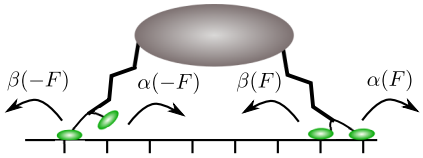

Figure A.7 Stepping rates of a motor pair under a strain force F. Considering the rates from fig. A.4(b), the most probable event for $F < F_s$ is a forward step of the trailing (left) motor. Thus, the strain is reduced between the motors.

the empirical force-velocity relation, eq. (A.13), and compare them to the results without backward stepping shown infig. 3.9. Note that in order to see an effect at all, we use a rather large backward velocity v_b. Typical values for v_b are in the range of nm/s, see also the experimentally determined force-velocity relation for $F > F_s$, where backward stepping dominates, shown in fig. A.3(b). Comparing the contour plots including backward stepping of fig. A.5 to the ones without backward stepping fig. 3.9, only a small difference in the system with the empirical force-velocity relation fig. A.5(b) and fig. A.5(d) can be found. However, this system exhibits a larger average velocity for high forces compared to the other cases. This difference arises from the fact that the empirical force-velocity relation has a different shape and, more significantly, a different force-free velocity v.

For a more quantitative comparison, we plot the scaled average velocity and the binding time as a function of the stiffness for kinesin-1 parameters of table 3.1. In case there is an effect from backward stepping, we expect it to occur for high coupling strength, where large forces are generated between the motors. However, the effect of backward stepping is small, see fig. A.6. A small difference occurs for coupling stiffnesses $\kappa > 0.8\,\mathrm{pN/nm}$.

To conclude, the effect of backward stepping is rather small. Even when high forces are generated between the motors, they tend to reduce the strain force by stepping towards each other. In order to understand this behavior, we consider the stepping rates for the motor pair shown in fig. A.7. The trailing motor is always under the force $-F$, and thus, its stepping rate is $\alpha(-F) = v/l$, assuming a constant force-velocity relation for assisting forces. Suppose that the strain force between the motors is on the order of the stall force. In this situation, the rate of forward stepping $\alpha(F) \simeq \beta(F)$ for the leading motor, but it is still small compared to $\alpha(-F)$ of the trailing motor, i.e. $\alpha(F) \ll \alpha(-F)$. As a consequence, it is most likely that the trailing motor steps forward, thereby reducing the strain force between the motors.

A.6. [ATP] dependence in the empirical force-velocity relation

The oversimplification of the [ATP] dependence of the force-velocity relation introduced in eq. (2.21) essentially scales the velocity without changing the shape of force-dependent part $\mathcal{V}(F)$. However, in experimental studies, it has been revealed that the shape of the force velocity relation also depends on the ATP concentration [69].

For a more detailed study, we consider the empirical force-velocity ration for low [ATP] by

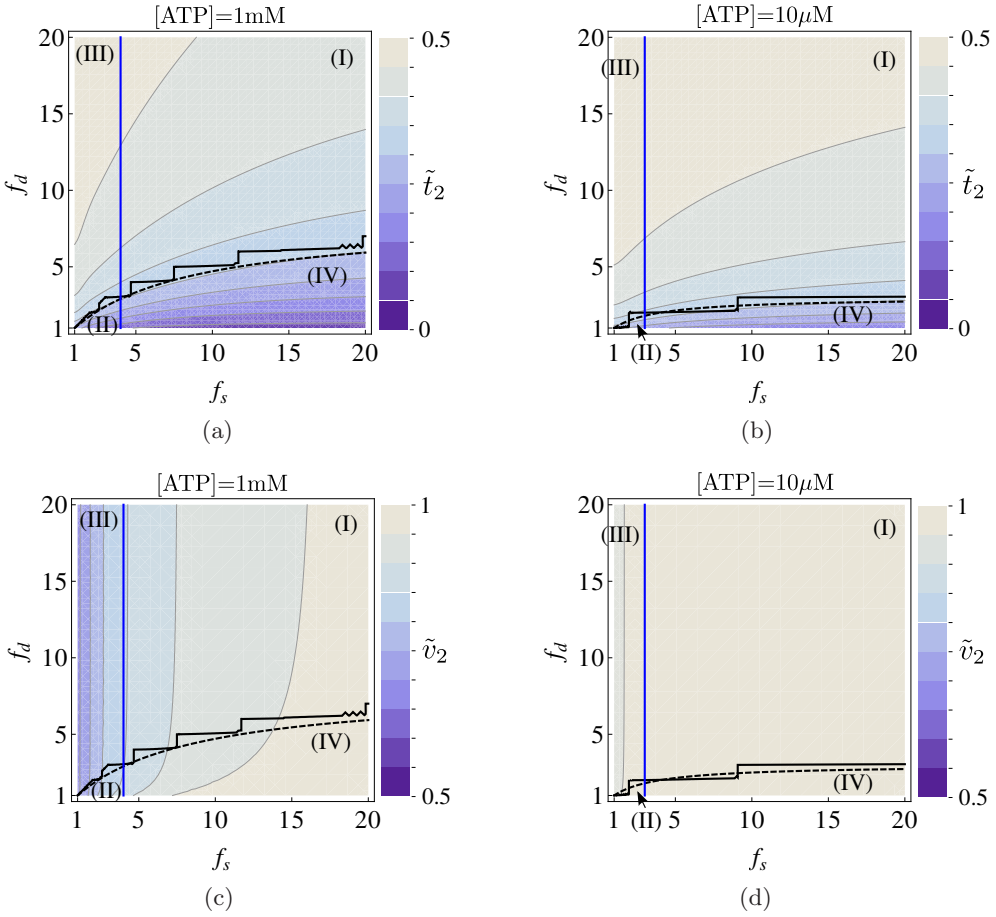

Figure A.8 (a) and (b) scaled binding time and (c) and (d) scaled velocity of two active kinesins with values from table 3.2, taking backward stepping into account. The stepping rates are determined from the fit to the data by Carter and Cross for [ATP]=1 mM (a) and (c) and for [ATP]=10 μM (b) and (d), see fig. A.3(c) and fig. A.3(d). The crossover lines between the transport regimes are obtained as explained in section 3.3.1, taking backward stepping into account. The solid blue line separates the region with and without a reduced velocity, whereas the solid black line separates the region of spontaneous and force-induced unbinding. The dashed lines correspond to the approximated crossover line as given by eq. (3.38). Slow motors typically unbind before generating substantial strain forces. Therefore, the interference regions (II), (III) and (IV) are small.

Carter and Cross, shown in fig. A.3(b). In combination with the step ratio $q(F)$, eq. (A.12), we determine the stepping rates for our single motor description and use, for the remaining parameters, the values from table 3.2. The scaled binding time $\tilde{t}_2$ and the scaled velocity $\tilde{v}_2$ are shown in fig. A.8. As expected for an ATP concentration this low, the regions with an effect on the unbinding and on the velocity are rather small compared to the results

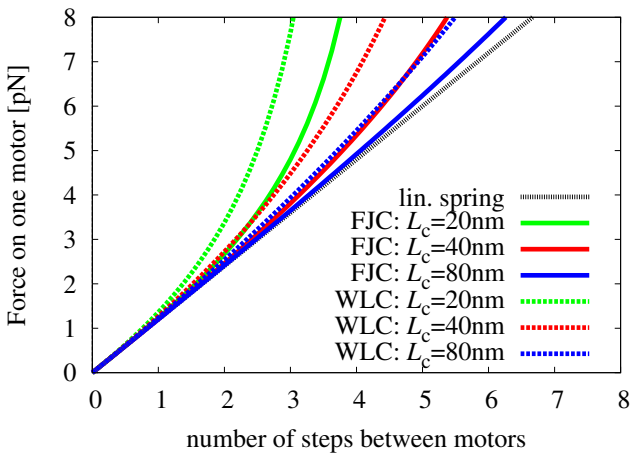

Figure A.9 Comparison of different force extension relations. The linear spring used throughout the work is compared to the freely jointed chain (FJC) and the worm like chain (WLC) model for different contour lengths L_c. In the case of a WLC with $L_c \simeq 20\,\mathrm{nm}$, a few steps between the motors are enough to generate forces on the order of the stall force.

for high [ATP]. Note, the shape of the force-velocity relation is now linear in the vicinity of $F = 0$, leading to a weak force-dependence of the average velocity, as explained by the symmetry argument in section 3.4.2. As also discussed in this section, the stall force might not be the appropriate force scale to characterize the reduced stepping for a symmetric force-velocity relation. However, the crossover line obtained from the time scale argument $t_{F_\mathrm{s}} = t_\mathrm{u}$ from section 3.3.1 separating the region with and without an effect on the velocity is shifted to the left compared to the case with a higher ATP concentration, compare blue lines in fig. A.8(c) and fig. A.8(d).

A.7. Non-linear springs as motor linkers

In this section, we discuss non-linear springs as motor linkers. A non-linear force extension relation can be incorporated in our model via eq. (3.4). In the case of the FJC, the extension is given as a function of the force eq. (2.17). In order to assign a force to a state of the network shown in fig. 3.4, we have to use a numerical algorithm for finding roots [137]. In this way, we obtain the force for a given extension. In fig. A.9, we plot the force extension relations for the FJC form eq. (2.17), for the WLC from eq. (2.18) and for the linear spring as a function of the distance between the two motors in units of the motor step size. The parameters are obtained from eq. (2.23) and eq. (2.24) with the kinesin value $\kappa \simeq 0.3\,\mathrm{pN/nm}$ from table 3.1.

Using the FJC and the WLC to mimic the elastic linkers, we consider the scaled binding time $\tilde{t}_2$ and the scaled velocity $\tilde{v}_2$ as a function of the contour length L_c. For the single

motor description, we use two sets of parameters: (i) the rates and parameters listed in table 3.1; (ii) the description based on the empirical force-velocity relation of appendix A.4 taking backward stepping into account. In general, for decreasing contour length L_c, both the binding time and the velocity decrease, see fig. A.10. This behavior arises from a larger strain force generation between the motors for small contour length, compare fig. A.9. In case of the linear force-velocity relation without backward stepping, case (i), the time $\tilde{t}_2$ and the velocity $\tilde{v}_2$ exhibit a kink. Further inspection reveals that this kink is an artifact that arises due to the combination of the simple force-velocity relation and the steep force extension relation for the WLC. Such a kink does not appear when describing the single motor with the empirical force-velocity relation including backward stepping, see fig. A.10(c) and fig. A.10(d).

However, the overall effect of the non-linear force extension relation is rather small and the linear spring as an approximation seems to be reasonable.

A.8. Initial conditions: binding under strain

In this section, we discuss the role of the initial condition. Until now, we assumed that when one motor is active the other motor binds into a state where the linkers are relaxed, the force-free state (0). In a real system, thermal fluctuations can lead to stretching of the linker of the inactive motor such that it reaches a different binding site. In this way, the motor binds under a strain force to the filament. Taking this into account, we assign a starting probability to every state, which is the Boltzmann distribution for the strain energy of two serial springs with the effective spring constant $\kappa/2$. This strain energy reads

$$E(i) = \frac{1}{4}\kappa(li)^2, \tag{A.19}$$

where l is the motor step size, here the distance to the next binding site. This energy leads to the starting weights

$$w(i) = \frac{1}{\sum_i e^{-E(i)/k_\mathrm{B}T}} e^{-E(i)/k_\mathrm{B}T} \tag{A.20}$$

for the initial states introduced in the network of fig. 3.3. The softer the springs are, the further they can, in principle, be pushed away by thermal fluctuations and therefore the starting probability distribution is broader, see fig. A.11(a). Nevertheless, the influence of 'binding under strain' is very small. For example, for the rates and parameter listed in table 3.1 with the initial probability distribution given by eq. (A.20), the scaled binding time and the average velocity are $\tilde{t}_2 \simeq 0.239$ and $\tilde{v}_2 \simeq 0.8450$, respectively. These values are only slightly different compared to the results, $\tilde{t}_2 \simeq 0.240$ and $\tilde{v}_2 \simeq 0.8456$, obtained for the same parameters but with binding exclusively into the state (0). Even when we compare the binding time and the average velocity over a range of stiffness κ for these two different initial conditions, we see no substantial difference fig. A.12. This rather weak dependence arises from the fact that although the second motor binds under strain force, the most probable pathway is to reduce the strain force by reducing the distance between the motors.

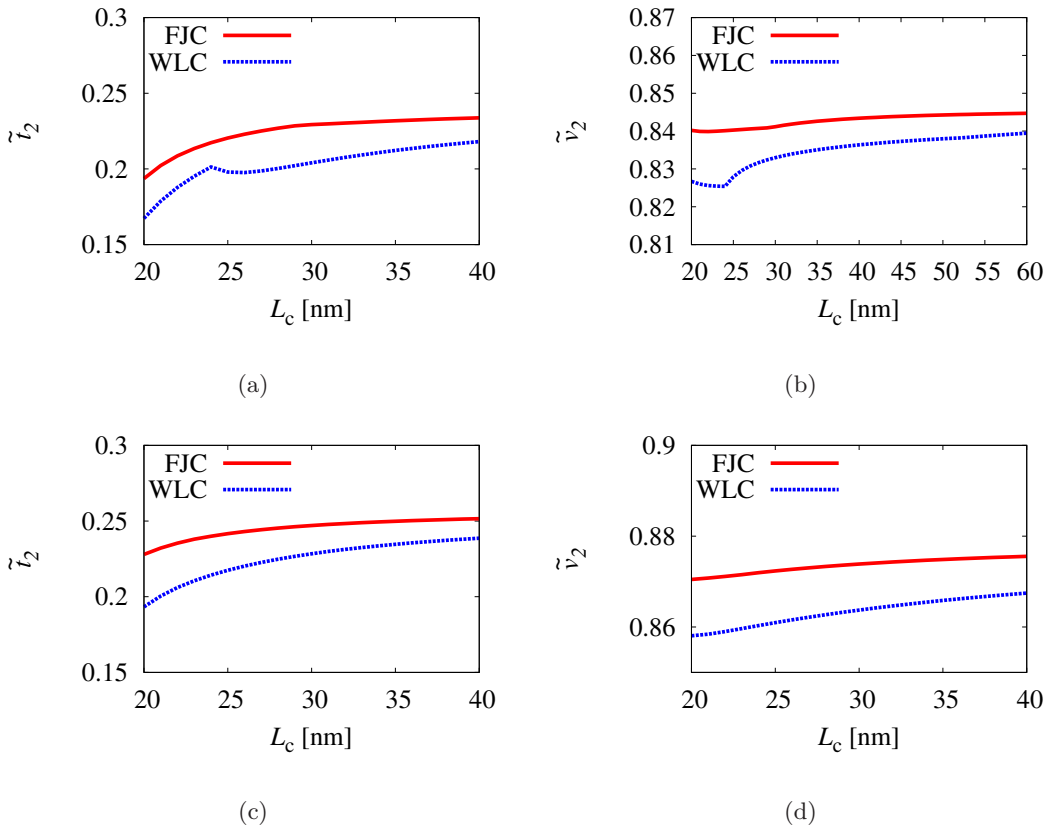

Figure A.10 Scaled binding time $\tilde{t}_2$ and velocity $\tilde{v}_2$ of two active kinesin with a FJC (straight red lines) or a WLC (dashed blue lines) as elastic linkers, as a function of a reasonable range of contour lengths L_c, see discussion in section 2.2.2. For (a) and (b), the single motor dynamics described by the rates and parameters from table 3.1 without backward stepping are used. With this reduced description, a kink appears for a WLC with small contour length in (a) and (b). This artifact disappears for the empirical force-velocity relation of fig. A.3(b) taking backward stepping into account, see (c) and (d).

We illustrate an extreme case in fig. A.11(b), where the inactive motor just has bound into a state, in which one motor is under stall force. Neglecting backward stepping, the forward stepping rate for the trailing motor is the largest rate, an order of magnitude larger than the unbinding rates. Therefore, it is most likely that the next transition reduces the strain force.

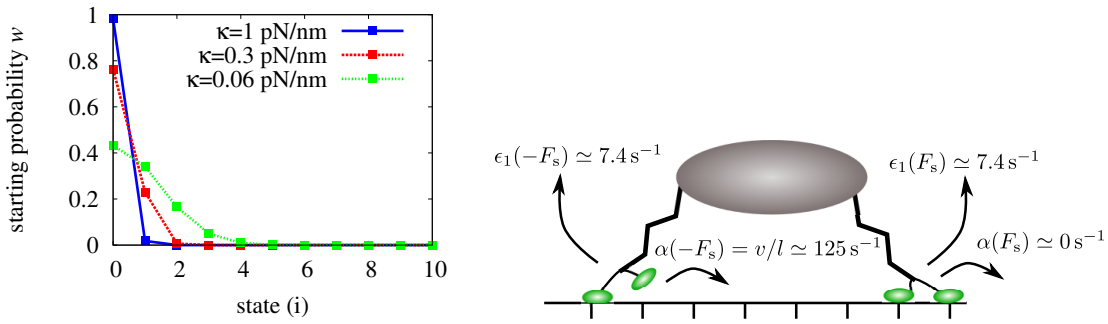

(a) (b)

Figure A.11 (a) Starting probability $w(i)$ for state (i) for different values of the coupling stiffness κ as in eq. (A.20). (b) Numerical values for the stepping rates and unbinding rates, when the strain force between the motors is of the order of the stall force F_s. The most probable transition is a step by the trailing motor and thus the elastic strain is reduced.

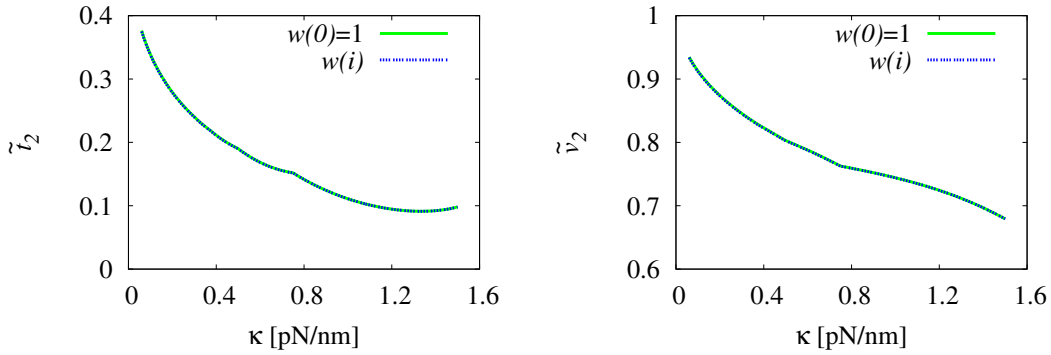

(a) (b)

Figure A.12 Comparison of the effect of different initial probability distributions. (a) Scaled binding time $\tilde{t}_2$ and (b) scaled velocity $\tilde{v}_2$ for two kinesins with rates and parameters from table 3.1, as a function of the stiffness κ. The motors start working exclusively in the relaxed state (0) with $w(0) = 0$ (green line). Starting in different states weighted with $w(i)$ from the Boltzmann distribution, eq. (A.20), does not change the results substantially (blue line).

A.9. Binding rate obtained from run length distribution

In this section, we explain how we obtain the binding rate π from a fit of the run length distribution. From the experimental data Rogers et al. determined a histogram of the overall cargo run length [25]. The bin-width of this histogram is $\Delta b = 1\mu$m. We numerate

the bins with the index i starting from $i = 1$ and denote the height of each bin h_i. To satisfy the normalization condition, we rescale all heights, such that $\sum_i h_i = 1$.

In case of fitting the binding rate π, all other parameters are known and we obtain the distribution of the cargo run length from eq. (A.2) as a function of $\langle \Delta x_{\mathrm{ca}} \rangle$ and π, $P(\langle \Delta x_{\mathrm{ca}} \rangle, \pi)$. In the scaled histogram, the height of the bin corresponds to the probability that the measurement of an event lies in the range of the bin. To compare the height of the bin with $P(\langle \Delta x_{\mathrm{ca}} \rangle, \pi)$, we have to integrate $P(\langle \Delta x_{\mathrm{ca}} \rangle, \pi)$ over the bin-width. Using a least square fit, we obtain the binding rate π from minimizing

$$\sum_i \left(\int_{(i-1)\Delta b}^{i\Delta b} P(\langle \Delta x_{\mathrm{ca}} \rangle, \pi)\, d\langle \Delta x_{\mathrm{ca}} \rangle - h_i \right)^2 . \tag{A.21}$$

This can be done numerically [137] and gives a numerical value for the binding rate π.

List of mathematical symbols

$A(f_\mathrm{s})$	numerical approximation used in eq. (3.43)
$\mathcal{A}'$	set of all states with at least one transition into an absorbing state
$\mathcal{A}$	set of all absorbing states
a	parameter for the slope of the force-velocity relation in eq. (3.50)
a_0	fit parameter in the numerical approximation $A(f_\mathrm{s})$
α	forward stepping rate
$\mathcal{B}$	set of all states
b	parameter for the plateau-width of the force-velocity relation in eq. (3.51)
Δb	bin-width of a histogram
β	backward stepping rate
$(\mathrm{C_i})$	activity state of a cargo, in which the cargo is bound to the filament by i active motors, see fig. 3.1
D	diffusion coefficient
δ	small increment
D_m	diffusion coefficient of myosin V on microtubule
$E(i)$	strain energy corresponding to the state (i), see eq. (A.19)
ϵ	force-free unbinding rate of a single motor
ϵ_1	force-dependent unbinding rate of single motor
ϵ_2	effective unbinding rate of a motor of a motor pair or the inverse of the time two motors are bound simultaneously to the filament
ϵ_k	kinesin unbinding rate

$\hat{\epsilon}_\mathrm{k}$	kinesin unbinding rate when myosin V is bound to the filament
ϵ_m	myosin V unbinding rate
$\hat{\epsilon}_\mathrm{m}$	myosin V unbinding rate when kinesin is bound to the filament
F	load force
F_d	detachment force
f_d	scaled detachment force as in eq. (3.27)
$\hat{F}_\mathrm{d,m}$	detachment force of myosin V diffusing on microtubule
F_d^-	detachment force for the assisting force direction
F_d^+	detachment force for the opposing force direction
F_i	discrete elastic force induced by a discrete extension, see eq. (3.4)
F_κ	strain force between two elastically coupled motors per motor step, see eq. (3.26)
F_m	myosin V's friction force, when it is pulled along a microtubule by kinesin.
F_s	stall force of a single motor
f_s	scaled stall force as in eq. (3.28)
ΔG	average free binding energy of myosin V to microtubule
γ	friction coefficient
h_i	height of bin i of a histogram
$I_{(i)}$	modified Bessel function
i_t	index of the target state of the network shown in fig. 3.8
J	probability current
κ	spring constant
κ_k	spring constant of kinesin
κ_m	spring constant of myosin V

κ_{tot}	total effective spring constant
$\mathcal{L}$	Fokker-Planck operator
Δl	spatial distance
l	step size of a molecular motor
l_0	rest length of a cable of the motor-cargo linker
L_{c}	contour length of a polymer (the motor-cargo linker)
L_{p}	persistence length for the WLC
L_{s}	segment length of the FJC
N	total number of states
$\mathcal{N}$	normalization constant
n	number of analyzed trajectories
N_{k}	number of kinesins attached to the cargo
n_{k}	number of kinesins bound to the filament
N_{m}	number of myosins attached to the cargo
n_{m}	number of myosins bound to the filament
N^-	number of states corresponding to the compression mode of cable like motor-cargo linkers
ω_{ij}	rate for a transition from state (i) to state (j)
$\langle\omega_{\mathrm{b}}\rangle$	average rate of a backward step of two elastically coupled motors before one of the motors unbinds
$\langle\omega_{\mathrm{f}}\rangle$	average rate of a forward step of two elastically coupled motors before one of the motors unbinds
$\omega_{\mathrm{b}}(i)$	effective rate of backward steps out of state (i)
$\omega_{\mathrm{f}}(i)$	effective rate of forward steps out of state (i)
ω_{off}	unbinding rate of a motor in a motor pair for the network shown in fig. 3.2(b) taking the strain in each state into account
ω_{r}	rate for relaxing the elastic element between two elastically coupled motors by one motor step

ω_s	rate for stretching the elastic element between two elastically coupled motors by one motor step
$P_\mathrm{sk}(i,t)$	modified Skellam distribution for the absolute distance i at time t, see eq. (3.64)
P_i	steady state probability of being in state (i)
$p_i(t)$	probability of being in state (i) at time t
p	probability
ϕ_nde	fraction of runs without diffusive events
π	circle number
π	binding rate of a single motor
π_k	kinesin binding rate
$\hat{\pi}_\mathrm{k}$	kinesin binding rate when myosin V is bound to the filament
π_m	myosin V binding rate to microtubule
$\hat{\pi}_\mathrm{m}$	myosin V binding rate to microtubule when kinesin is bound to the filament
ψ_i	probability density function of the waiting time in state (i)
Q	steady state probability of network in fig. 4.4(b)
$q(F)$	force-dependent ratio of forward to backward steps
q_0	force-free ratio of forward to backward steps
$r_{n_\mathrm{m},n_\mathrm{k}}(x,t)$ . . .	probability of being in state $(n_\mathrm{m}, n_\mathrm{k})$ at position x at time t
$\mathcal{S}$	set of all starting states
$\sigma()$	standard deviation of the quantity in the brackets
$\sigma^2()$	variance of the quantity in the brackets
Θ	ratio of the detachment forces associated with different direction, see eq. (3.54)
t	time
δt	small time increment

$\langle \Delta t_{\mathrm{ca}} \rangle$	average binding time of a cargo
Δt_{ca}	binding time of a cargo
τ_{D}	estimated time for motors with cable-like linkers to step out of the compression mode
$\langle \Delta t \rangle$	average time to absorption
$\langle \Delta t_{\mathrm{de}} \rangle$	average time of a diffusive event
$t_{F_{\mathrm{d}}}$	time it takes to generate strain forces between two elastically coupled motors comparable to the detachment force F_{d}
$t_{F_{\mathrm{s}}}$	time it takes to generate strain forces between two elastically coupled motors comparable to the stall force F_{s}
$\langle \Delta t_i \rangle$	average waiting time in state (i)
τ_i	time spent in state (i) before absorption
t_1	average binding time of one motor to the filament
t_2	average binding time of two elastically coupled motors simultaneously to the filament
$\tilde{t}_2$	average scaled binding time of two elastically coupled motors simultaneously to the filament in units of the single motor binding time t_1
$\langle \Delta t_{\mathrm{k}} \rangle$	average binding time of kinesin on microtubule
$\langle \Delta t_{\mathrm{m}} \rangle$	average binding time of myosin V on microtubule
$\langle \Delta t_{\mathrm{se}} \rangle$	average time of a stepping event
t_{u}	time scale for spontaneous unbinding of a motor in a motor pair
$U(x)$	tilted potential
$\mathcal{V}(F)$	velocity as a function of the force F used as the force-velocity relation for a single motor
$V(x)$	potential
v	force-free single motor velocity
v_1	average velocity of one molecular motor or of a cargo transported by one motor

v_2	average velocity of two elastically coupled molecular motors or of a cargo transported by two motors simultaneously
$\tilde{v}_2$	average scaled velocity of two elastically coupled motors in units of the single motor velocity v
v_b	backward velocity of a motor
$\langle v \rangle_\mathrm{ca}$	average over the single trajectory velocity of a cargo
v_ca	average velocity of a cargo bound to the filament
v_i	velocity of the cargo particle in state (i)
v_k	velocity of kinesin on microtubule
$\langle v^2 \rangle_\mathrm{ca}$	mean square velocity of a cargo
v_max	maximal velocity of the empirical force velocity relation in eq. (A.13)
v_min	minimal velocity of the empirical force velocity relation in eq. (A.13)
w	constant starting probability
$w_{0,0}$	splitting probability of starting in state $(0,1)$ and being absorbed in state $(0,0)$ in the network shown in fig. 4.4(a)
$w_{1,1}$	probability for a stepping event to start in state $(1,1)$ of the network shown in fig. 4.2
$w(i)$	initial probability to start in state (i)
$W(i,j)$	transition probability from state (i) to state (j)
w_k	probability for a 'kinesin start' in state $(0,1)$ in fig. 4.2
$X(t)$	stochastic process in time
x	spatial coordinate
x_0	position of the minimum of the potential, see fig. 2.3(a)
x_b	position of the barrier of the potential, see fig. 2.3(a)
$\langle \Delta x_\mathrm{ca} \rangle$	average run length of a cargo
Δx_ca	run length of a cargo

Δx	extension of an elastic element
Δx_i	discrete extension of an elastic element
$\left\langle \Delta x_{\mathrm{ca}}^2 \right\rangle$	mean square run length of a cargo
$\lceil\ \rceil$	the ceiling function gives the smallest integer not less than the value in the brackets

Acronyms

[ATP]	adenosine triphosphate concentration
ADP	adenosine diphosphate
AFM	atomic force microscopy
ATP	adenosine triphosphate
DNA	deoxyribonucleic acid
EM	electron microscope
FJC	freely jointed chain
KIF	kinesin superfamily
Pi	inorganic phosphate
Qdot	quantum dot
RNA	ribonucleic acid
TIRF	total internal reflection fluorescence as in total internal reflection fluorescence microscope (TIRFM)
WLC	worm like chain

Bibliography

[1] Alberts, B., Johnson, A., Walter, P., Lewis, J., Raff, M. & Roberts, K. *Molecular Biology of the Cell* (Taylor & Francis, 2007).

[2] Nelson, D. L. & Cox, M. M. *Lehninger Principles of Biochemistry* (Palgrave Macmillan, 2008).

[3] Howard, J. *Mechanics of Motor Proteins and the Cytoskeleton* (Sinauer Associates, Sunderland (Mass.), 2001).

[4] Schliwa, M. & Woehlke, G. Molecular motors. *Nature* **422**, 759 (2003).

[5] Vale, R. D. & Milligan, R. A. The way things move: Looking under the hood of molecular motor proteins. *Science* **288**, 88 (2000).

[6] Vale, R. D. The molecular motor toolbox for intracellular transport. *Cell* **112**, 467 (2003).

[7] Hirokawa, N., Noda, Y., Tanaka, Y. & Niwa, S. Kinesin superfamily motor proteins and intracellular transport. *Nature Rev. Mol. Cell Biol.* **10**, 682 (2009).

[8] Mallik, R. & Gross, S. Molecular motors: Strategies to get along. *Curr. Biol.* **14**, R971 (2004).

[9] Welch, M. D., Mallavarapu, A., Rosenblatt, J. & Mitchison, T. J. Actin dynamics in vivo. *Curr. Opin. Cell Biol.* **9**, 54 (1997).

[10] Hirokawa, N. From electron microscopy to molecular cell biology, molecular genetics and structural biology: intracellular transport and kinesin superfamily proteins, KIFs: genes, structure, dynamics and functions. *J. Electron Microsc. (Tokyo)* **60 (suppl 1)**, S63 (2011).

[11] Lawrence, C. J. *et al.* A standardized kinesin nomenclature. *J. Cell. Biol.* **167**, 19 (2004).

[12] Hirokawa, N. Kinesin and dynein superfamily proteins and the mechanism of organelle transport. *Science* **279**, 519 (1998).

[13] Sellers, J. R. Myosins: a diverse superfamily. *Biochim. Biophys. Acta* **1496**, 3 (2000).

[14] Mallik, R. & Gross, S. P. Molecular motors as cargo transporters in the cell - the good, the bad and the ugly. *Physica A* **372**, 65 (2006).

[15] Ashkin, A., Schütze, K., Dziedzic, J. M., Euteneuer, U. & Schliwa, M. Force generation of organelle transport measured in vivo by an infrared laser trap. *Nature* **348**, 346 (1990).

[16] Holzbaur, E. L. & Goldman, Y. E. Coordination of molecular motors: from in vitro assays to intracellular dynamics. *Curr. Opin. Cell Biol.* **22**, 4 (2010).

[17] Miller, R. H. & Lasek, R. I. Cross-bridges mediate anterograde and retrograde vesicle transport along microtubules in squid axoplasm. *J. Cell. Biol.* **101**, 2181 (1985).

[18] Hirokawa, N. Cross-linker system between neurofilaments, microtubules, and membranous organelles in frog axons revealed by the quick-freeze, deep-etching method. *J. Cell. Biol.* **94**, 129 (1982).

[19] Hill, D. B., Plaza, M. J., Bonin, K. & Holzwarth, G. Fast vesicle transport in PC12 neurites: velocities and forces. *Eur. Biophys. J.* **33**, 623 (2004).

[20] Welte, M. A. Bidirectional transport along microtubules. *Curr. Biol.* **14**, R525 (2004).

[21] Goode, B. L., Drubin, D. G. & Barnes, G. Functional cooperation between the microtubule and actin cytoskeletons. *Curr. Opin. Cell Biol.* **12**, 63 (2000).

[22] Levi, V., Serpinskaya, A. S., Gratton, E. & Gelfand, V. Organelle transport along microtubules in Xenopus melanophores: Evidence for cooperation between multiple motors. *Biophys. J.* **90**, 318 (2006).

[23] Berger, F., Keller, C., Müller, M. J. I., Klumpp, S. & Lipowsky, R. Co-operative transport by molecular motors. *Biochem. Soc. Trans.* **39**, 1211 (2011).

[24] Beeg, J., Klumpp, S., Dimova, R., Gracià, R. S., Unger, E. & Lipowsky, R. Transport of beads by several kinesin motors. *Biophys. J.* **94**, 532 (2008).

[25] Rogers, A. R., Driver, J. W., Constantinou, P. E., Jamison, D. K. & Diehl, M. R. Negative interference dominates collective transport of kinesin motors in the absence of load. *Phys. Chem. Chem. Phys.* **11**, 4882 (2009).

[26] Jamison, D. K., Driver, J. W., Rogers, A. R., Constantinou, P. E. & Diehl, M. R. Two kinesins transport cargo primarily via the action of one motor: Implications for intracellular transport. *Biophys. J.* **99**, 2967 (2010).

[27] Soppina, V., Rai, A. K., Ramaiya, A. J., Barak, P. & Mallik, R. Tug-of-war between dissimilar teams of microtubule motors regulates transport and fission of endosomes. *Proc. Natl. Acad. Sci. U.S.A.* **106**, 19351 (2009).

[28] Hendricks, A. G., Perlson, E., Ross, J. L., Schroeder III, H. W., Tokito, M. & Holzbaur, E. L. F. Motor coordination via a tug-of-war mechanism drives bidirectional vesicle transport. *Curr. Biol.* **20**, 697 (2010).

[29] Ali, M. Y., Lu, H., Bookwalter, C. S., Warshaw, D. M. & Trybus, K. M. Myosin V and kinesin act as tethers to enhance each others' processivity. *Proc. Natl. Acad. Sci. U.S.A.* **105**, 4691 (2008).

[30] Klumpp, S. & Lipowsky, R. Cooperative cargo transport by several molecular motors. *Proc. Natl. Acad. Sci. U.S.A.* **102**, 17284 (2005).

[31] Müller, M. J. I., Klumpp, S. & Lipowsky, R. Tug-of-war as a cooperative mechanism for bidirectional cargo transport by molecular motors. *Proc. Natl. Acad. Sci. U.S.A.* **105**, 4609 (2008).

[32] Berger, F., Müller, M. J. I. & Lipowsky, R. Enhancement of the processivity of kinesin-transported cargo by myosin V. *EPL* **87**, 28002 (2009).

[33] Gross, S. P., Vershinin, M. & Shubeita, G. T. Cargo transport: Two motors are sometimes better than one. *Curr. Biol.* **17**, R478 (2007).

[34] Hunt, A., Gittes, F. & Howard, J. The force exerted by a single kinesin molecule against a viscous load. *Biophys. J.* **67**, 766 (1994).

[35] Gagliano, J., Walb, M., Blaker, B., Macosko, J. C. & Holzwarth, G. Kinesin velocity increases with the number of motors pulling against viscoelastic drag. *Eur. Biophys. J.* **39**, 801 (2010).

[36] Coy, D. L., Wagenbach, M. & Howard, J. Kinesin takes one 8-nm step for each ATP that it hydrolyzes. *J. Biol. Chem.* **274**, 3667 (1999).

[37] Mallik, R., Petrov, D., Lex, S. A., King, S. & Gross, S. Building complexity: An in vitro study of cytoplasmic dynein with in vivo implications. *Curr. Biol.* **15**, 2075 (2005).

[38] Hodges, A. R., Krementsova, E. B. & Trybus, K. M. Engineering the processive run length of myosin V. *J. Biol. Chem.* **282**, 27192 (2007).

[39] Constantinou, P. E. & Diehl, M. R. The mechanochemistry of integrated motor protein complexes. *J. Biomech.* **43**, 31 (2010).

[40] Vershinin, M., Carter, B. C., Razafsky, D. S., King, S. J. & Gross, S. P. Multiple-motor based transport and its regulation by tau. *Proc. Natl. Acad. Sci. U.S.A.* **104**, 87 (2007).

[41] Bieling, P., Telley, I. A., Piehler, J. & Surrey, T. Processive kinesins require loose mechanical coupling for efficient collective motility. *EMBO Rep.* **9**, 1121 (2008).

[42] Keller, C. *Diploma Thesis: Coupled molecular motors* (Humboldt University of Berlin, 2009).

[43] Korn, C. B., Klumpp, S., Lipowsky, R. & Schwarz, U. S. Stochastic simulations of cargo transport by processive molecular motors. *J. Chem. Phys.* **131**, 245107 (2009).

[44] Wang, Z. & Li, M. Force-velocity relations for multiple-molecular-motor transport. *Phys. Rev. E* **80**, 041923 (2009).

[45] Kunwar, A. & Mogilner, A. Robust transport by multiple motors with nonlinear force-velocity relations and stochastic load sharing. *Phys. Biol.* **7**, 016012 (2010).

[46] Driver, J. W., Rogers, A. R., Jamison, D. K., Das, R. K., Kolomeisky, A. B. & Diehl, M. R. Coupling between motor proteins determines dynamic behaviors of motor protein assemblies. *Phys. Chem. Chem. Phys.* **12**, 10398 (2010).

[47] Zhang, Y. Cargo transport by several motors. *Phys. Rev. E* **83**, 011909 (2011).

[48] Gross, S. P. Hither and yon: a review of bi-directional microtubule-based transport. *Phys. Biol.* **1**, R1 (2004).

[49] Gennerich, A. & Schild, D. Finite-particle tracking reveals submicroscopic-size changes of mitochondria during transport in mitral cell dendrites. *Phys. Biol.* **3**, 45 (2006).

[50] Schuster, M., Lipowsky, R., Assmann, M., Lenz, P. & Steinberg, G. Transient binding of dynein controls bidirectional long-range motility of early endosomes. *Proc. Natl. Acad. Sci. U.S.A.* **108**, 3618 (2011).

[51] Müller, M. J. I., Klumpp, S. & Lipowsky, R. Motility states of molecular motors engaged in a stochastic tug-of-war. *J. Stat. Phys.* **133**, 1059 (2008).

[52] Müller, M. J. I., Berger, F., Klumpp, S. & Lipowsky, R. Cargo transport by two teams of molecular motors. *Biophys. J.* **98**, 432a (2010).

[53] Langford, G. M. Actin- and microtubule-dependent organelle motors: interrelationships between the two motility systems. *Curr. Opin. Cell Biol.* **7**, 82 (1995).

[54] Brown, S. S. Cooperation between microtubule- and actin-based motor proteins. *Annu. Rev. Cell Dev. Biol.* **15**, 63 (1999).

[55] Snider, J., Lin, F., Zahedi, N., Rodionov, V., Yu, C. C. & Gross, S. P. Intracellular actin-based transport: How far you go depends on how often you switch. *Proc. Natl. Acad. Sci. U.S.A.* **101**, 13204 (2004).

[56] Ross, J. L., Ali, M. Y. & Warshaw, D. M. Cargo transport: molecular motors navigate a complex cytoskeleton. *Curr. Opin. Cell Biol.* **20**, 41 (2008).

[57] Rodionov, V., Yi, J., Kashina, A., Oladipo, A. & Gross, S. P. Switching between microtubule- and actin-based transport systems in melanophores is controlled by camp levels. *Curr. Biol.* **13**, 1837 (2003).

[58] Ali, M. Y., Krementsova, E. B., Kennedy, G. G., Mahaffy, R., Pollard, T. D., Trybus, K. M. & Warshaw, D. M. Myosin Va maneuvers through actin intersections and diffuses along microtubules. *Proc. Natl. Acad. Sci. U.S.A.* **104**, 4332–4336 (2007).

[59] Hodges, A. R., Bookwalter, C. S., Krementsova, E. B. & Trybus, K. M. A nonprocessive class V myosin drives cargo processively when a kinesin- related protein is a passenger. *Curr. Biol.* **19**, 2121 (2009).

[60] Kincaid, M. M. & King, S. J. Motors and their tethers: The role of secondary binding sites in processive motility. *Cell Cycle* **5**, 2733 (2006).

[61] Culver-Hanlon, T. L., Lex, S. A., Stephens, A. D., Quintyne, N. J. & King, S. J. A microtubule-binding domain in dynactin increases dynein processivity by skating along microtubules. *Nat. Cell. Biol.* **8**, 264 (2006).

[62] King, S. J. & Schroer, T. A. Dynactin increases the processivity of the cytoplasmic dynein motor. *Nat. Cell. Biol.* **2**, 20 (2000).

[63] Berezuk, M. A. & Schroer, T. A. Dynactin enhances the processivity of kinesin-2. *Traffic* **8**, 124 (2007).

[64] Geething, N. C. & Spudich, J. A. Identification of a minimal myosin Va binding site within an intrinsically unstructured domain of melanophilin. *J. Biol. Chem.* **282**, 21518 (2007).

[65] Lipowsky, R. & Klumpp, S. 'life is motion': multiscale motility of molecular motors. *Physica A* **352**, 53 (2005).

[66] Kodera, N., Yamamoto, D., Ishikawa, R. & Ando, T. Video imaging of walking myosin V by high-speed atomic force microscop. *Nature* **468**, 72 (2010).

[67] Seitz, A. & Surrey, T. Processive movement of single kinesins on crowded microtubules visualized using quantum dots. *EMBO J.* **25**, 267 (2006).

[68] Trejo, H. E., Lecuona, E., Grillo, D., Szleifer, I., Nekrasova, O. E., Gelfand, V. I. & Sznajder, J. I. Role of kinesin light chain-2 of kinesin-1 in the traffic of Na,K-ATPase-containing vesicles in alveolar epithelial cells. *FASEB J.* **24**, 374 (2010).

[69] Carter, N. J. & Cross, R. A. Mechanics of the kinesin step. *Nature* **435**, 308 (2005).

[70] Visscher, K., Schnitzer, M. J. & Block, S. M. Single kinesin molecules studied with a molecular force clamp. *Nature* **400**, 184 (1999).

[71] Clancy, B. E., Behnke-Parks, W. M., Andreasson, J. O. L., Rosenfeld, S. S. & Block, S. M. A universal pathway for kinesin stepping. *Nat. Struct. Mol. Biol.* **18**, 1020 (2011).

[72] Liepelt, S. & Lipowsky, R. Kinesin's network of chemomechanical motor cycles. *Phys. Rev. Lett.* **98**, 258102 (2007).

[73] Bierbaum, V. & Lipowsky, R. Chemomechanical coupling and motor cycles of myosin V. *Biophys. J.* **100**, 1747 (2011).

[74] Block, S. M., Goldstein, L. S. B. & Schnapp, B. J. Bead movement by single kinesin molecules studied with optical tweezers. *Nature* **348**, 348 (1990).

[75] Ally, S., Larson, A. G., Barlan, K., Rice, S. E. & Gelfand, V. I. Opposite-polarity motors activate one another to trigger cargo transport in live cell. *J. Cell. Biol.* **187**, 1071 (2010).

[76] Veigel, C. & Schmidt, C. F. Moving into the cell: single-molecule studies of molecular motors in complex environments. *Nat. Rev. Mol. Cell Biol.* **12**, 163 (2011).

[77] Lipowsky, R., Beeg, J., Dimova, R., Klumpp, S., Liepelt, S., Müller, M. J. I. & Valleriani, A. Active bio-systems: from single motor molecules to cooperative cargo transport. *Biophys. Rev. Lett.* **4**, 77 (2009).

[78] Lipowsky, R., Klumpp, S. & Nieuwenhuizen, T. M. Random walks of cytoskeletal motors in open and closed compartments. *Phys. Rev. Lett.* **87**, 108101 (2001).

[79] Klumpp, S. & Lipowsky, R. Active diffusion of motor particles. *Phys. Rev. Lett.* **95**, 268102 (2005).

[80] Verhey, K. J., Kaul, N. & Soppina, V. Kinesin assembly and movement in cells. *Annu. Rev. Biophys.* **40**, 267 (2011).

[81] Kramers, H. Brownian motion in a field of force and the diffusion model of chemical reactions. *Physica* **7**, 284 (1940).

[82] Bell, G. I. Models for the specific adhesion of cells to cells. *Science* **200**, 618 (1978).

[83] Evans, E. & Ritchie, K. Dynamic strength of molecular adhesion bonds. *Bio. Phys. J.* **72**, 1541 (1997).

[84] Dudko, O. K., Hummer, G. & Szabo, A. Theory, analysis, and interpretation of single-molecule force spectroscopy experiment. *Proc. Natl. Acad. Sci. U.S.A.* **105**, 15755 (2008).

[85] Gardiner, C. W. *Handbook of Stochastic Methods* (Springer-Verlag, Berlin, 2004).

[86] van Kampen, N. G. *Stochastic processes in physics and chemistry* (North-Holland, Amsterdam, 1981).

[87] Gittes, F., Meyhöfer, E., Baek, S. & Howard, J. Directional loading of the kinesin motor molecule as it buckles a microtubule. *Biophys. J.* **70**, 418 (1996).

[88] Bustamante, C., Marko, J. F., Siggia, E. D. & Smith, S. Entropic elasticity of lambda-phage DNA. *Science* **265**, 1599 (1994).

[89] Phillips, R., Kondev, J. & Theriot, J. *Physical Biology of the Cell* (Garland Science, 2009).

[90] Leduc, C., Campàs, O., Zeldovich, K. B., Roux, A., Jolimaitre, P., Bourel-Bonnet, L., Goud, B., Joanny, J. F., Bassereau, P. & Prost, J. Cooperative extraction of membrane nanotubes by molecular motors. *Proc. Natl. Acad. Sci. U.S.A.* **101**, 17096 (2004).

[91] Gennerich, A., Carter, A. P., Reck-Peterson, S. L. & Vale, R. D. Force-induced bidirectional stepping of cytoplasmic dynein. *Cell* **131**, 952 (2007).

[92] Clemen, A. E. M., Vilfan, M., Jaud, J., Zhang, J., Bärmann, M. & Rief, M. Force-dependent stepping kinetics of myosin-V. *Biophys. J.* **88**, 4402 (2005).

[93] Ökten, Z., Churchman, L. S., Rock, R. S. & Spudich, J. A. Myosin VI walks hand-over-hand along actin. *Nat. Struct. Mol. Biol.* **11**, 884 (2004).

[94] Schnitzer, M., Visscher, K. & Block, S. Force production by single kinesin motors. *Nat. Cell. Biol.* **2**, 718 (2000).

[95] Svoboda, K. & Block, S. M. Force and velocity measured for single kinesin molecules. *Cell* **77**, 773 (1994).

[96] Coppin, C., Pierce, D., Hsu, L. & Vale, R. The load dependence of kinesin's mechanical cycle. *Proc. Natl. Acad. Sci. U.S.A.* **94**, 8539 (1997).

[97] Toba, S., Watanabe, T. M., Yamaguchi-Okimoto, L., Toyoshima, Y. Y. & Higuchi, H. Overlapping hand-over-hand mechanism of single molecular motility of cytoplasmic dynein. *Proc. Natl. Acad. Sci. U.S.A.* **103**, 5741 (2006).

[98] Mallik, R., Carter, B. C., Lex, S. A., King, S. J. & Gross, S. Cytoplasmic dynein functions as a gear in response to load. *Nature* **427**, 649 (2004).

[99] Mehta, A. D., Rock, R. S., Rief, M., Spudich, J. A., Mooseker, M. S. & Cheney, R. E. Myosin-V is a processive actin-based motor. *Nature* **400**, 590 (1999).

[100] Rock, R. S., Rice, S. E., Wells, A. L., Purcell, T. J., Spudich, J. A. & Sweeney, H. L. Myosin VI is a processive motor with a large step size. *Proc. Natl. Acad. Sci. U.S.A.* **98**, 13655 (2001).

[101] Ali, M. Y., Kennedy, G. G., Safer, D., Trybus, K. M., Lee Sweeney, H. & Warshaw, D. M. Myosin Va and myosin VI coordinate their steps while engaged in an in vitro tug of war during cargo transport. *Proc. Natl. Acad. Sci. U.S.A.* **108**, E535 (2011).

[102] Kawaguchi, K., Uemura, S. & Ishiwata, S. Equilibrium and transition between single- and double-headed binding of kinesin as revealed by single-molecule mechanics. *Biophys. J.* **84**, 1103 (2003).

[103] Sakakibara, H., Kojima, H., Sakai, Y., Katayama, E. & Oiwa, K. Inner-arm dynein c of chlamydomonas flagella is a single-headed processive motor. *Nature* **400**, 586 (1999).

[104] Oiwa, K. & Sakakibara, H. Recent progress in dynein structure and mechanism. *Curr. Opin. Cell Biol.* **17**, 98 (2005).

[105] Veigel, C., Schmitz, S., Wang, F. & Sellers, J. R. Load-dependent kinetics of myosin-V can explain its high processivity. *Nat. Cell. Biol.* **9**, 861 (2005).

[106] Burgess, S. A., Walker, M. L., Sakakibara, H., Knight, P. J. & Oiwa, K. Dynein structure and power stroke. *Nature* **421**, 715 (2003).

[107] Krementsov, D. N., Krementsova, E. B. & Trybus, K. M. Myosin V: regulation by calcium, calmodulin, and the tail domain. *J. Cell. Biol.* **164**, 877 (2004).

[108] Erickson, R. P., Jia, Z., Gross, S. P. & Yu, C. C. How molecular motors are arranged on a cargo is important for vesicular transport. *PLoS Comput. Biol.* **7**, e1002032 (2011).

[109] Müller, M. J. I. *Ph.D. Thesis: Bidirectional transport by molecular motors* (University of Potsdam, 2008).

[110] Moffitt, J. R., Chemla, Y. R., Smith, S. B. & Bustamante, C. Recent advances in optical tweezers. *Annu. Rev. Biochem.* **77**, 205 (2008).

[111] Ashkin, A. Acceleration and trapping of particles by radiation pressure. *Phys. Rev. Lett.* **24**, 156 (1970).

[112] Perkins, T. T. Optical traps for single molecule biophysics: a primer. *Laser & Photon. Rev.* **3**, 203 (2009).

[113] Visscher, K. & Block, S. Versatile optical traps with feedback control. *Meths. Enzymol.* **298**, 460 (1998).

[114] Uemura, S., Higuchi, H., Olivares, A. O., De La Cruz, E. M. & Ishiwata, S. Mechanochemical coupling of two substeps in a single myosin V motor. *Nat. Struct. Mol. Biol.* **11**, 877 (2004).

[115] Lipowsky, R. Universal aspects of the chemomechanical coupling for molecular motors. *Phys. Rev. Lett.* **85**, 4401 (2000).

[116] Forkey, J. N., Quinlan, M. E., Shaw, M. A., Corrie, J. E. T. & Goldman, Y. E. Three-dimensional structural dynamics of myosin V by single-molecule fluorescence polarization. *Nature* **422**, 399 (2003).

[117] Schief, W. R., Clark, R. H., Crevenna, A. H. & Howard, J. Inhibition of kinesin motility by ADP and phosphate supports a hand-over-hand mechanism. *Proc. Natl. Acad. Sci. U.S.A.* **101**, 1183 (2004).

[118] Dudko, O. K., Hummer, G. & Szabo, A. Intrinsic rates and activation free energies from single-molecule pulling experiments. *Phys. Rev. Lett.* **96**, 108101 (2006).

[119] Uemura, S., Kawaguchi, K., Yajima, J., Edamatsu, M., Toyoshima, Y. Y. & Ishiwata, S. Kinesin-microtubule binding depends on both nucleotide state and loading direction. *Proc. Natl. Acad. Sci. U.S.A.* **99**, 5977 (2002).

[120] Mikhailenko, S. V., Oguchi, Y. & Ishiwata, S. Insights into the mechanisms of myosin and kinesin molecular motors from the single-molecule unbinding force measurements. *J. R. Soc. Interface* **7**, S295 (2010).

[121] Cross, R. A. The kinetic mechanism of kinesin. *Trends Biochem. Sci.* **29**, 301 (2004).

[122] Woehlke, G. & Schliwa, M. Walking on two heads: The many talents of kinesin. *Nat. Cell. Biol.* **1**, 50 (2000).

[123] Schwaiger, I., Sattler, C., Hostetter, D. R. & Rief, M. The myosin coiled-coil is a truly elastic protein structure. *Nature Materials* **1**, 232 (2002).

[124] Jeney, S., Stelzer, E. H. K., Grubmüller, H. & Florin, E. L. Mechanical properties of single motor molecules studied by three-dimensional thermal force probing in optical tweezers. *Chem. Phys. Chem.* **5**, 1150 (2004).

[125] Risken, H. *The Fokker-Planck Equation* (Springer Berlin Heidelberg, 1996).

[126] Hill, T. L. Interrelations between random walks on diagrams (graphs) with and without cycles. *Proc. Natl. Acad. Sci. U.S.A.* **85**, 2879 (1988).

[127] Hill, T. L. Further properties of random walks on diagrams (graphs) with and without cycles. *Proc. Natl. Acad. Sci. U.S.A.* **85**, 3271 (1988).

[128] Hill, T. L. Number of visits to a state in a random walk, before absorption, and related topics. *Proc. Natl. Acad. Sci. U.S.A.* **85**, 4577 (1988).

[129] Rozanov, Y. *Probability Theory: A Concise Course* (Dover Publications, 1977).

[130] Schnakenberg, J. Network theory of microscopic and macroscopic behavior of master equation systems. *Rev. Mod. Phys.* **48**, 571 (1976).

[131] Hill, T. L. *Free Energy Transduction and Biochemical Cycle Kinetics* (Springer, New York, 1989).

[132] Bouzat, S. & Falo, F. The influence of direct motor-motor interaction in models for cargo transport by a single team of motors. *Phys. Biol.* **7**, 046009 (2010).

[133] Kunwar, A., Vershinin, M., Xu, J. & Gross, S. P. Stepping, strain gating, and an unexpected force-velocity curve for multiple-motor-based transport. *Curr. Biol.* **18**, 1173 (2008).

[134] Campàs, O., Kafri, Y., Zeldovich, K. B., Casademunt, J. & Joanny, J.-F. Collective dynamics of interacting molecular motors. *Phys. Rev. Lett.* **97**, 038101 (2006).

[135] Press, W. H., Teukolsky, S. A., Vetterling, W. T. & Flannery, B. P. *Numerical Recipes* (Cambridge University Press, 2007).

[136] *GSL - GNU Scientific Library* (www.gnu.org/s/gsl/).

[137] *Mathematica 8.0.1.0* (Wolfram Research, 2011).

[138] Seifert, U. Rupture of multiple parallel molecular bonds under dynamic loading. *Phys. Rev. Lett.* **84**, 2750 (2000).

[139] Schwarz, U. S., Erdmann, T. & Bischofs, I. B. Focal adhesions as mechanosensors: The two-spring model. *BioSystems* **83**, 225 (2006).

[140] Varga, V., Leduc, C., Bormuth, V., Diez, S. & Howard, J. Kinesin-8 motors act cooperatively to mediate length-dependent microtubule depolymerization. *Cell* **138**, 1174 (2009).

[141] Skellam, J. G. The frequency distribution of the difference between two poisson variates belonging to different populations. *J. Roy. Stat. Soc.* **109**, 296 (1946).

[142] Irwin, J. O. The frequency distribution of the difference between two independent variates following the same poisson distribution. *J. of the Roy. Stat. Soc.* **100**, 415 (1937).

[143] Einstein, A. Über die von der molekularkinetischen Theorie der Wärme geforderte Bewegung von in ruhenden Flüssigkeiten suspendierten Teilchen. *Ann. der Physik* **322**, 549 (1905).

[144] Gillespie, D. T. Exact stochastic simulation of coupled chemical reactions. *J. Phys. Chem.* **81**, 2340 (1977).

[145] Astumian, D. Equilibrium theory for a particle pulled by a moving optical trap. *J. Chem. Phys.* **126**, 111102 (2007).

[146] Posta, F., D'Orsogna, M. R. & Chou, T. Enhancement of cargo processivity by cooperating molecular motors. *Phys. Chem. Chem. Phys.* **11**, 4851 (2009).

[147] Hammer III, J. A. & Wu, X. Slip sliding away with myosin V. *Proc. Natl. Acad. Sci. U.S.A.* **104**, 5255 (2007).

[148] Pan, X., Ou, G., Civelekoglu-Scholey, G., Blacque, O. E., Endres, N. F., L.Tao, Mogilner, A., abd R. D. Vale, M. R. L. & Scholey, J. M. Mechanism of transport of IFT particles in C. elegans cilia by the concerted action of kinesin-II and OSM-3 motors. *J. Cell. Biol.* **174**, 1035 (2006).

[149] Larson, A. G., Landahl, E. C. & Rice, S. E. Mechanism of cooperative behaviour in systems of slow and fast molecular motors. *Phys. Chem. Chem. Phys.* **11**, 4890 (2009).

[150] Driver, J. W., Jamison, D. K., Uppulury, K., Rogers, A. R., Kolomeisky, A. B. & Diehl, M. R. Productive cooperation among processive motors depends inversely on their mechanochemical efficiency. *Biophys. J.* **101**, 386 (2011).

[151] Hirokawa, N. & Takemura, R. Biochemical and molecular characterization of diseases linked to motor proteins. *Trends Biochem. Sci.* **28**, 558 (2003).

[152] Korten, T., Månsson, A. & Diez, S. Towards the application of cytoskeletal motor proteins in molecular detection and diagnostic devices. *Curr. Opin. Biotech.* **21**, 477 (2010).

[153] van den Heuvel, M. G. L. & Dekker, C. Motor proteins at work for nanotechnology. *Science* **317**, 333 (2007).

[154] Müller, M. J. I., Berger, F., Klumpp, S. & Lipowsky, R. *Organelle-Specific Pharmaceutical Nanotechnology*, chap. 16, 289 (John Wiley & Sons, Inc., Hoboken, NJ, USA, 2010).

Danksagung

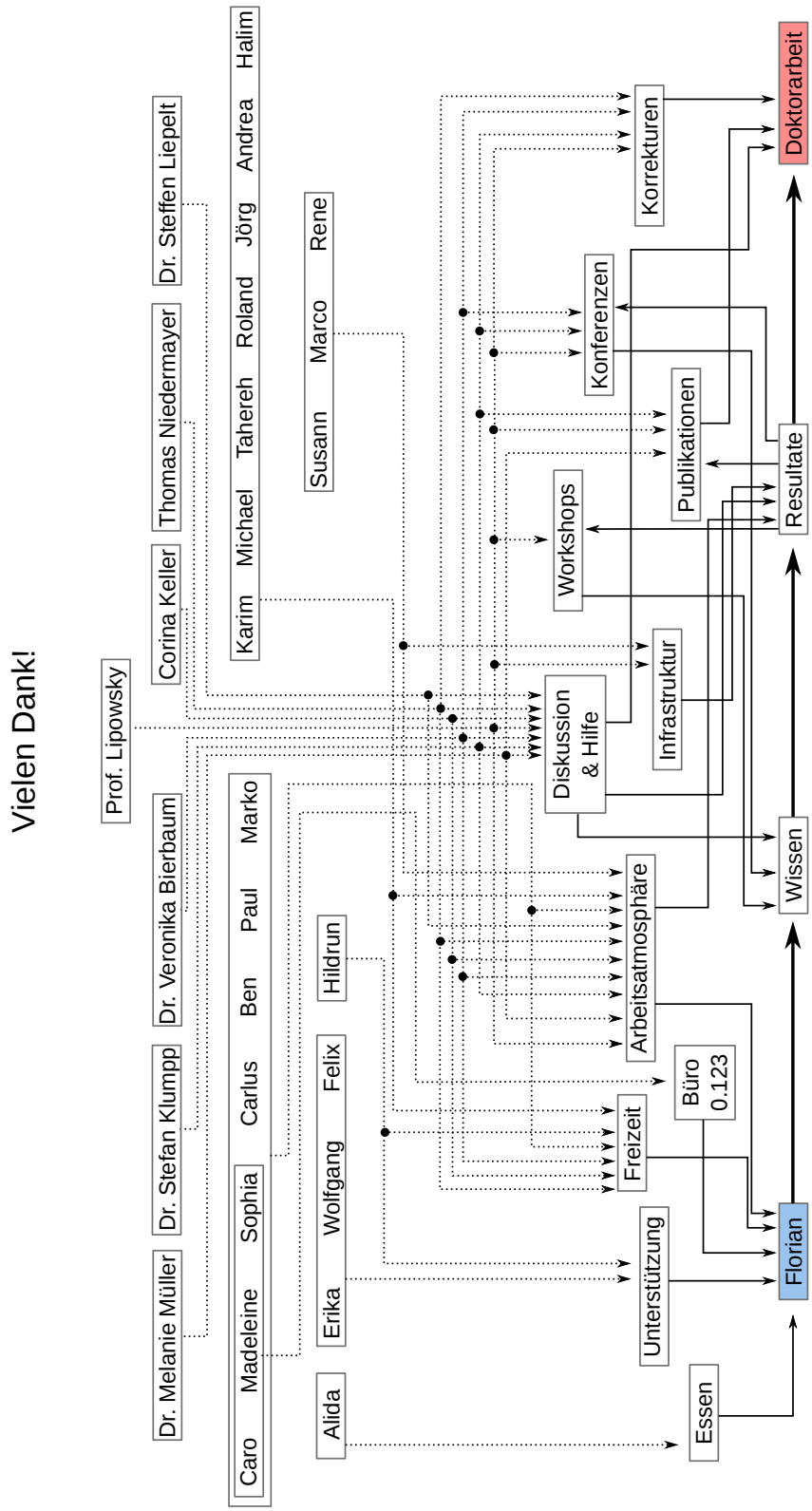
Vielen Dank!
Prof. Lipowsky
Dr. Melanie Müller
Dr. Stefan Klumpp
Dr. Veronika Bierbaum
Corina Keller
Thomas Niedermayer
Dr. Steffen Liepelt
Caro
Madeleine
Sophia
Carlus
Ben
Paul
Marko
Alida
Erika
Wolfgang
Felix
Hildrun
Karim
Michael
Tahereh
Roland
Jörg
Andrea
Halim
Susann
Marco
Rene
Essen
Florian
Unterstützung
Freizeit
Büro 0.123
Arbeitsatmosphäre
Diskussion & Hilfe
Infrastruktur
Workshops
Konferenzen
Publikationen
Korrekturen
Wissen
Resultate
Doktorarbeit

Ehrenwörtliche Erklärung

Hiermit erkläre ich, dass diese Arbeit an keiner anderen Hochschule eingereicht, sowie selbstständig verfasst und keine anderen als die angegebenen Quellen und Hilfsmittel verwendet wurden.

Florian Berger,
Potsdam, January 16, 2012